Phonons, Non-linear Elasticity and First-principles Theory of Martensitic Structural Transformations in Metals

A Thesis

Submitted For the Degree of

DOCTOR OF PHILOSOPHY

in the Faculty of Science

by

Pawan Kumar

THEORETICAL SCIENCES UNIT
JAWAHARLAL NEHRU CENTRE FOR ADVANCED SCIENTIFIC RESEARCH
Bangalore – 560 064

MARCH 2020

To tax payers

विद्या वितर्को विज्ञानं स्मृतिः तत्परता क्रिया ।
यस्यैते षड्गुणास्तस्य नासाध्यमतिवर्तते ॥

Translation

Nothing remains 'unachievable' for those who have
these six virtues Knowledge, Logic, Science,
Memory, Readiness and functionality.

DECLARATION

I hereby declare that the matter embodied in the thesis entitled "**Phonons, Non-linear Elasticity and First-principles Theory of Martensitic Structural Transformations in Metals**" is the result of investigations carried out by me at the Theoretical Sciences Unit, Jawaharlal Nehru Centre for Advanced Scientific Research, Bangalore, India under the supervision of Prof. Umesh V. Waghmare and that it has not been submitted elsewhere for the award of any degree or diploma.

In keeping with the general practice in reporting scientific observations, due acknowledgement has been made whenever the work described is based on the findings of other investigators.

Pawan Kumar

CERTIFICATE

I hereby certify that the matter embodied in this thesis entitled "**Phonons, Non-linear Elasticity and First-principles Theory of Martensitic Structural Transformations in Metals**" has been carried out by Mr. Pawan Kumar at the Theoretical Sciences Unit, Jawaharlal Nehru Centre for Advanced Scientific Research, Bangalore, India under my supervision and that it has not been submitted elsewhere for the award of any degree or diploma.

Prof. Umesh V. Waghmare
(Research Supervisor)

Acknowledgements

I would like to express my sincere gratitude to my thesis advisor Professor Umesh V. Waghmare. His excellent guidance and endless support have always helped me to overcome all kinds of obstacles throughout my Ph.D. Working with him was an amazing experience, and his passion and enthusiasm for science always kept me motivated. I am also very thankful for his valuable comments and instructions in preparing for seminars and writing papers.

I am thankful to my research collaborators: Prof. Sahab Dass, Dr. Anupam Srivastav, Harish K. Singh, Prof. Dipankar Banerjee and Dr. Manu S. Mohan.

I thank all the TSU faculties and course instructors: Prof. Shobhana Narasimhan, Prof. Kavita Jain, Prof. Subir K Das, Prof. Swapan K. Pati, Prof. Srikant Sastri, Prof. Vidyadhiraja, Prof. Meher K. Prakash, Prof. C. Narayana (CPMU) and Prof. Balasubramanian (CPMU) for providing excellent knowledge of their subjects and stimulating scientific interactions.

I am very thankful to my past and present lab members Sharmila, Summayya, Anjali, Kaushik, Arpita, Krishnmonan, Shashwat, Harish, Henu, Sweta, Himanshu, Sandhya, Shivani, Sampath, Suchitra, Meha, Anuja, Lakshay, Narendra, Raagya, Shashank, Koyendrila, Arijit, Prasad, Shazia, Meghana and Prashant for many academic, non-academic and fun interactions and lessons.

I am very thankful to Aruna madam and Kruti for their wonderful hospitality, and for making me feel like a family.

I am grateful to my friends in JNCASR, Anand, Aditya, Rajaji, Manjeet, Nikita, Krishnendu, Rafi, Praveen, Anshul, Pradeep, Samarth, Badri, Akash, Navneet, Shubhajit, Debdipto and Rajdeep for their help and wonderful company in all these years.

I sincerely thank my intermediate (11^{th} and 12^{th} class) teacher Mr. Mahesh

Chandra Kushwaha. He has not only taught free tuition of physics in my economically tough days but also motivated me to follow my dream in research. My special thanks to Mr. Vijendra Singh Nayak for his financial support during my college days. He was kind enough to me and always said that your education should not stop because of financial issues.

I am very fortunate to have friends like Harendra Pratap, Kuldeep Pandey, Chetan Chauhan, Ram Singh, Yogesh Sharma, Deepshika Malkar and Manoj Kumar. I met with these guys at various stages of my career and now they become an important part of my life. Life becomes very easy and enjoyable when one has friends like them.

I would like to acknowledge the Centre for Computational Material Science (CCMS) for providing computational facilities, using which some of the calculations in the work presented here were performed. I would also like to thank the Complab staff for tending to our problems at any time of the day. I also extend my gratitude to Librarian, Academic and Administrative staff for their efficiency and helpfulness. I thank Dhanvantari staffs, Hostel mess, Chandraya canteen and utility for food facilities.

Last but not least, I thank my parents for always believing in me, providing endless freedom and unconditional support at all stages of my life.

Synopsis

Martensitic transformations (MTs) form an important class of first-order structural phase transformations exhibited by crystalline solids that involve breaking of symmetry upon cooling (quenching) or applying external stresses on the high-temperature phases. The structures stable above and below the transformation temperature are called austenite and martensite respectively. Symmetry breaking of the austenite phase is a result of diffusionless (cooperative) atomic displacements within the periodic unit cell and its deformation typically without breaking any bonds. These features define an MT as distinct from other transformations. Examples of MTs are seen in steel, shape memory alloys, many elemental metals and their alloys, and ferroelectric materials. These materials are of great importance to advanced technologies ranging from medical applications, robotic structures to automotive and aerospace industries. Immense technological relevance of materials undergoing MT and its singular impact on their behavior make MT one of the most widely studied phenomena in metallurgy and materials science. Our focus in this thesis is on the MTs exhibited by shape memory alloys and group IV B transition metals (Ti, Zr and Hf).

It is now quite well-established that first-principles density functional theory (DFT) and simulations are capable of accurate prediction of ground state properties of materials arising from mechanisms operating at various scales. Though computing resources have advanced greatly, the cost of these simulations limit their efficacy in determination of properties of materials primarily at low temperatures. It is generally impractical to do first-principles Monte Carlo simulations and Molecular Dynamics requiring large system sizes to study of finite temperature properties like structural phase transformations. Indeed, DFT does provide important information that can be used in estimation of finite temperature properties. The main theme

of this thesis is devoted to determination of the finite-temperature phase transformations in metallic materials within the framework of statistical mechanics using models derived from the results of first-principles DFT calculations.

In this thesis, we make extensive use of first-principles DFT calculations, and have developed three significantly important techniques to study martensitic structural transformations governed by the physics of coupled unstable phonons and strain exhibiting nonlinear elasticity in the materials: (i) Quantum mechanical analysis of unstable phonons ($\omega^2 < 0$) to determine their free energy, where the harmonic approximation is not valid, (ii) Construction a materials-specific effective Hamiltonian as a function of coupled phonons and strain modes using the method of lattice Wannier functions (LWFs) to capture the low energy physics of martensitic transformations in metallic materials, and (iii) A periodic generalization of Landau theory that can describe energetics of microstructure and martensitic transformations in materials. These methods provide a significant advance in studies of thermodynamic properties, microstructures relevant to shape memory effect and physics of martensitic transformations in metallic materials. We note that methods (i) and (iii) are new and based on innovative ideas and have general applicability. Method (i) and (ii) were used in resolving the relative stability issues of various martensite phases and investigation of MTs in NiTi (chapter 3) and PtTi (chapter 4) shape memory alloys respectively. Method (ii) was also employed in our analysis of an MT in Ti elemental metal (chapter 5). Method (iii) was used to model the energy along path of martensitic transformations in group IV B transition metals (chapter 6).

List of Publications

(1) **Pawan Kumar** and Umesh V. Waghmare, "First-principles Phonon-based Model and Theory of Martensitic Phase Transformation in NiTi Shape Memory Alloy", Materialia **9**, 100602 (2020).

(2) **Pawan Kumar** and Umesh V. Waghmare, "*Ab Initio* Statistical Mechanics of Martensitic Phase Transformation in PtTi High Temperature Shape Memory Alloy", (preprint available).

(3) **Pawan Kumar** and Umesh V. Waghmare, "First-principles Theory of Martensitic Structural Transformation from β to α Structure in Titanium", (preprint available).

(4) **Pawan Kumar** and Umesh V. Waghmare, "Fourier-Landau Theoretical Analysis of Phase Transformations in IV B Group Elemental metals", (manusript under preparation).

Not included in thesis

(5) Harish K. Kumar, **Pawan Kumar** and Umesh V. Waghmare, "Theoretical Prediction of a Stable 2D Crystal of Vanadium Porphyrin: A Half-Metallic Ferromagnet", The Journal of Physical Chemistry C **119**, 25657 (2015).

(6) Anupam Srivastav, **Pawan Kumar**, Anuradha Verma, York R. Smith, Vibha R. Satsangi, Rohit Srivastav, Umesh V. Waghmare and Sahab Dass, "Experimental and First-principles Studies of $BiVO_4/BiV_{1-x}Mn_xO_{4-y}$ $n-n^+$ Homojunction for Efficient Charge Carrier Separation in Sunlight Induced Water Splitting", International Journal of Hydrogen Energy, **43**, 15815 (2018).

List of Figures

List of Tables

Contents

Chapter 1

Introduction

Martensitic transformation (MT) is a first-order displacive structural transformation in crystalline solids which involves breaking of symmetry, induced by cooling (quenching) or applying external stresses on the high-temperature phases [1–3]. The structures stable above and below the transformation temperature are called austenite (named after W. C. Roberts-Austen) and martensite (named after Adolf Martens), respectively. Symmetry breaking of the austenite phase is a result of diffusionless (cooperative) atomic movement and deformation in which atoms displace relative to each other without breaking the bonds and not exceeding the interatomic distance. These features distinguish an MT from other transformations. It commonly occurs in steel, shape memory alloys, many elemental metals and their alloys, and ferroelectric [4] materials. The set of materials known to undergo MT is continuously increasing. These materials are of great importance to advanced technologies ranging from medical applications to robotic structures, automotive and aerospace industries. The immense technological relevance of materials undergoing MT and interesting features associated with it make MT one of the most widely studied phenomena by metallurgists and materials scientists.

1.1 Crystallography of martensitic transformation

Crystal structures of austenite and martensite phases depend strongly on the type of materials and of martensitic transformation. Generally in metals and their alloys, austenite phases have the cubic crystal lattices (B2, BCC or FCC), the martensite phase is characterized by reduced symmetry of distorted cubic lattice. Consequently, martensite phases may have tetragonal, orthorhombic, rhombohedral, monoclinic, hexagonal or BCC crystal lattices, which depend on the chemistry of material and structure of the austenite phase. For example, (i) ferrous alloys (iron-carbon alloys, commonly known as steel) transform from face-centered cubic (FCC) structure to body-centered cubic (BCC) or base-centered tetragonal (BCT) structure through an MT, (ii) most of the shape memory alloys have B2 (CsCl lattice type) structure in the austenite phase and B19 (orthorhombic) or/and B19$'$ (monoclinic) structures in the martensite phases, (iii) Group IV B transition metals (Ti, Zr and Hf) undergo a martensitic transformation from BCC (or β) structure to hexagonal close-packed (HCP or α) and hexagonal open-packed (HOP or ω) structures. Our focus in this thesis is on categories (ii) and (iii).

1.2 Experimental observations

The phenomenon of martensitic transformations in metallic alloys has a long history, and was a mystery for metallurgists until middle of 19^{th} century due to the lack of experimental techniques. The first notable experimental observation was made on steel (iron-carbon alloys) by Henry Clifton Sorby in 1863 [5] using the reflected light microscopy, revealing a bulk metallic microstructure. After that, a series of experimental observations using optical microscopy and a high degree of hardness of the martensite steel was interpreted in terms of its microstructure. The major breakthrough in this field came after the discovery of X-ray diffraction (XRD) in

1912. XRD, used to determining crystal structures, was very soon adopted by scientists to study martensitic transformations. Westgren (1921) [6] and Westgren and Phragmen (1922, 1924) [7,8] successfully explained the crystallography of allotropes of iron. In 1950's transmission electron microscopy (TEM) augmented XRD and inspired new theories and approaches in this field. Apart from steel, MTs then were demonstrated in other alloys such as InTl, CuAl, CuZn and many elemental metals and their alloys. Another breakthrough impacting engineering applications occurred with the discovery of NiTi by Buehler in 1963 [9], which was shown to be a remarkable shape memory alloy exhibiting a reversible martensitic transformation. The commercial success and vast applications of NiTi in technologies spearheaded intense research activity in shape memory alloys, making them widely investigated alloys.

1.3 Theoretical developments

Experimental evidence in the crystallography of austenite and martensite structures motivated scientists to find the theoretical explanation of MTs. The very first theory was proposed by Bain in 1924 [10] using the concept of lattice correspondence (LC) that builds a relationship between austenite and martensite lattices and provides an important link between them through a lattice distortion. He successfully explained the diffusionless character of MT in steel and illustrated the homogeneous deformation of the FCC austenite phase to the BCC martensite phase, now called the Bain strain. A simple deformation mechanism proposed by Bain failed to explain shear deformation, invariant planes between austenite and martensite phases and twinning, and it was considered as an oversimplified theory but yet important work to understand MTs. Kurdjumov and Sachs in 1930 [11] and Nishiyama in 1934 [12]

proposed mechanisms based on orientation relationship (OR) between the martensite and austenite phases that include rotation of the transforming portion of the material leading to shear deformation. Though the OR theories of Kurdjumov and Sachs, and Nishiyama explained shear deformation in MTs it failed to explain the invariant planes and twinning.

Thereafter in the 1950's when mathematical concepts were adapted by metallurgists and material scientists, two famous works proposed phenomenological theories of martensite crystallography (PTMC) of MTs: (i) by Wechsler, Lieberman and Read (WLR) [13,14] and (ii) by Bowles and Mackenzie (BM) [15–17], independently. The WLR theory of crystallography of MTs was formulated in real space while the BM theory was formulated in the reciprocal space. Though the two formulations are different they are proven to be equivalent [18]. In these theories, deformation and rotation of austenite lattice are represented by matrices as operators acting on an arbitrary vector, and the invariant plane is the interface between austenite and martensite phases which is undistorted and unrotated. PTMC is one of the most successful theories based on geometrical crystallography with well established mathematical framework. Though PTMC theory is very sucssefull in explaining the MTs where only lattice distortion take place, in shape memory and many other alloys atomic displacements also take place along with lattice distortions, and the PTMC theory does not quite explain their MTs. With advances in first-principles simulations methods to study properties of materials, atomic displacements described in terms of phonons became readily accessible. First-principles calculations have become a very useful tool to study MTs in materials.

It is now quite well-established that first-principles based density functional theory (DFT) is capable of predicting ground state properties of materials at various scales with remarkable accuracy. It is (a) predictive, (b) complementary to experiments, and (c) helpful in understanding mechanisms. Some properties are the direct

outcome of DFT simulations including total energy, electronic structure, phonon frequencies, stress and forces etc. Though computing resources have advanced greatly, DFT is still tool to determine properties of materials primarily at T=0 K and it is impractical to do first-principles Monte Carlo (MC) simulations and Molecular Dynamics (MD) that require large system sizes to study of finite temperature properties, e.g. structural phase transformations. Of course, DFT provides important information that can be used in estimation of finite temperature properties. The main work of this thesis is devoted to determining the finite temperature behavior of materials within the framework of statistical mechanics using models derived from the results of DFT calculations.

Rabe and Joahnopouos [19, 20] developed an *ab initio* effective Hamiltonian approach which takes a subset of the degrees of freedom which are relevant to the phase transformation. They constructed an effective Hamiltonian as a function of these degrees of freedom, determined its parameters from first-principles and successfully explained the ferroelectric structural transformation in GeTe. Following this approach Zhong, Vanderbilt and Rabe [21] constructed an effective Hamiltonian to explain the ferroelectric phase transition in $BaTiO_3$. Rabe and Waghmare [22] took forward this idea and developed an effective Hamiltonian scheme based on lattice Wannier functions (LWFs), and used it to study phase transformations in ferroelectric $PbTiO_3$ [23] and antiferroelectric $PbZrO_3$ [24]. Though this approach became quite popular in the field of ferroelectric phase transformations, it has been challenging to generalize this to other structural phase transformation. We have taken it further here and constructed an effective Hamiltonian using LWFs to study martensitic transformation in shape memory alloys (NiTi and PiTi) and titanium an elemental metal.

1.4 Overview of the thesis

In this thesis, we make extensive use of first-principles DFT calculations, and have developed three significantly important techniques to study martensitic structural transformations governed by the physics of coupled unstable phonons and strain exhibiting nonlinear elasticity in the materials: (i) Quantum mechanical analysis of unstable phonons ($\omega^2 < 0$) to determine their free energy, where the harmonic approximation is not valid, (ii) Construction a materials-specific effective Hamiltonian as a function of coupled phonons and strain modes using the method of lattice Wannier functions (LWFs) to capture the low energy physics of martensitic transformations in metallic materials, and (iii) A periodic generalization of Landau theory (Fourier-Landau theory) that can describe energetics of microstructure and martensitic transformations in materials. These methods provide a significant advance in studies of thermodynamic properties, microstructures relevant to shape memory effect and physics of martensitic transformations in metallic materials. We note that methods (i) and (iii) are new and based on innovative ideas and have general applicability. Method (i) and (ii) were used in resolving the relative stability issues of various martensite phases and investigation of MTs in NiTi and PtTi shape memory alloys respectively. Method (ii) was also employed in our analysis of an MT in Ti elemental metal. Method (iii) was used to model the energy along path of martensitic transformations in group IV B transition metals.

In Chapter 2, we present a brief description of first-principles methods used in this work, starting with Hohenberg-Kohn theorems and foundations of Kohn-Sham density functional theory (DFT) that replace the interacting many-body problem with an effective non-interacting electron problem. In the second part, the formalism used in the estimation of free-energies of unstable phonons. In the third part, we will review the method of construction of an effective Hamiltonian that is used in

investigation of martensitic transformations in shape memory alloys and in pure titanium. Finally, we will present the basis of periodic generalization of Landau theory that is used to study MTs in IV B group transition metals.

In Chapter 3, we present a phonon-based model and its statistical mechanical analysis to obtain atomistic insights into martensite phases and transformation in NiTi, uncovering seven order parameters that are relevant to its MT. With Monte Carlo simulations of an effective Hamiltonian derived to capture its low energy landscape, we determine its soft phonons and establish the cell-doubling $M_{5'}$ mode as the primary order parameter. Using Landau theoretical analysis, we show that relative strengths of its third-order coupling with secondary order parameters (e.g., strain) determine the specific symmetry of low-T martensite structures emerging at the MT. Our pressure-dependent Monte Carlo simulations show that negative pressure enhances the martensitic transformation temperature, while positive pressure can stabilize B19 as an intermediate phase during the MT. We present analysis of microstructures of NiTi using the effective Hamiltonian approach and show that the domain walls separating domains with distinct orientations of order parameters identified here are essentially the twinning or stacking faults relevant to the microstructures governing martensitic transformation.

In Chapter 4, we present a theoretical analysis of martensitic transformation in PtTi, a high-temperature shape memory alloy. Similar to NiTi, PtTi also occurs in the B2 structure at high temperature. However, its ground state is the monoclinic (B19′) structure. We show that vibrational entropy of soft modes stabilizes the orthorhombic (B19) structure at $T > 112$ K, the experimentally known ground state. We use the same form of effective Hamiltonian as one used for NiTi, with parameters specific to PtTi determined from first-principles, and present its analysis with Monte Carlo simulations to determine the T-dependent MT. Landau theoretical analysis of effective Hamiltonian reveals important phonon instabilities and their couplings

with strain, and confirm that the relative strengths of primary order parameter's ($M_{5'}$) third-order coupling with secondary order parameters indeed determine the stability of B19 structure. We have identified four order parameters relevant to the MT exhibited by PtTi.

In Chapter 5, we present a detailed statistical mechanical analysis of an effective Hamiltonian derived to capture the low energy physics of Ti and investigate its martensitic transformation from the body-centered cubic (BCC or β) to hexagonal close-packed (HCP or α) structure. Analysis of phonon modes and strains of the β structure reveals that α-phase corresponds to a specific amplitude of unstable $M_{5'}$ phonon mode and values of strains. We present Monte Carlo simulations of the effective Hamiltonian of Ti demonstrating β to α martensitic transformation identifying the relevant soft modes and their behavior near martensitic transformation temperature.

In Chapter 6, we present a Fourier generalization of Landau theoretical energy function that is essential for a single description that captures the translational symmetry and physics of microstructure and of the martensitic transformations in materials. We apply this theory to two martensitic transformations in Group IV B transition metals: (i) $\beta \rightarrow \alpha$, and (ii) $\beta \rightarrow \omega$. Finally, we summarize highlighting the achievements in this thesis and limitations of the methods used, and present our perspective on the opportunities of further work in chapter 7.

Chapter 2

Methods and Formalism

In this chapter, we describe theoretical and computational methods that we used in our calculations or developed to determine the various properties of materials: (i) at T = 0 K within the framework of first-principles density functional theory, and (ii) T-dependent phenomena (e.g. martensitic transformations).

2.1 First-principles methods

Materials are described as a collection of nuclei and electrons that interact via the electromagnetic fields, and the various properties of it can be determined by their motions and interactions among them. The collection of electrons and nuclei makes it a many-body problem, and the fundamental Hamiltonian of this problem that describes their motion and interactions is given by [25],

$$\begin{aligned} \hat{H} &= -\frac{\hbar^2}{2m_e}\sum_i \nabla_i^2 + \frac{1}{2}\sum_{i\neq j}\frac{e^2}{|\mathbf{r}_i-\mathbf{r}_j|} - \sum_{i,I}\frac{Z_I e^2}{|\mathbf{r}_i-\mathbf{R}_I|} \\ &- \sum_I \frac{\hbar^2}{2M_I}\nabla_I^2 + \frac{1}{2}\sum_{I\neq J}\frac{Z_I Z_J e^2}{|\mathbf{R}_I-\mathbf{R}_J|}, \end{aligned} \tag{2.1}$$

where m_e and e are the mass and charge of an electron respectively, and $\hbar$ is the reduced Planck constant. $\mathbf{r}_i$ is the position vector of i^{th} electron. $\mathbf{R}_I$, M_I and Z_I are the position vector, mass and atomic number of the I^{th} nucleus, respectively. The first and fourth terms in Eq. (2.1) are the kinetic energy of electrons and nuclei respectively. Second, third and fifth terms represent electron-electron, electron-nuclei and nuclei-nuclei Coulomb interactions, respectively.

Though the many-body Hamiltonian (Eq. 2.1) looks simple, its solution is almost impossible for a material that consists of the large number of electrons and nuclei. Therefore, we sovle Eq. (2.1) within the Born-Oppenheimer approximation (adiabatic approximation) [26]. This approximation has been made considering the fact that $M_I >> m_e$, the kinetic energy of nuclei is much lower than that of electrons, and can be ignored. Thus, electrons and nuclei can be treated as quantum and classical particles, respectively. Consequently, the total energy of a given set of atoms in a material is the sum of the nuclei-nuclei Coulomb interaction and electronic ground state energy. To estimate the electronic ground state energy, the form of many-body electronic Hamiltonian can be written as:

$$\hat{H}_e = \hat{T}_e + \hat{V}_{int} + \hat{V}_{ext}, \tag{2.2}$$

where $\hat{T}_e$, $\hat{V}_{int}$ and $\hat{V}_{ext}$ denote kinetic energy, electron-electron interations and potential acting on the electrons due to nuclei, respectively. The many-body wavefunctions of electrons are obtained by time-independent Schrödinger equation:

$$\hat{H}\Psi(\mathbf{R},\mathbf{r}) = \epsilon\Psi(\mathbf{R},\mathbf{r}), \tag{2.3}$$

where ϵ and $\psi(\mathbf{R},\mathbf{r})$ are the ground state energy eigenvalue and wavefunction

of the electrons, respectively. **R** and **r** are the position vectors of nuclei and electrons in the materials respectively. Since, the electrons are fermions, $\psi(\mathbf{R}, \mathbf{r})$ must be antisymmetric under exchange of two electronic coordinates $\mathbf{r}_i$. Though Born-Oppenheimer approximation reduces the difficulty to determine the ground state for a given set of atoms and their positions, quantum mechanical solution of Eq. (2.3) for the large number of atoms is still a challenge. Therefore, determination of the ground state is quite hard and requires additional approximations.

2.2 Density functional theory

Density functional theory (DFT) is one of the most popular and versatile quantum mechanical modeling methods to investigate the electronic structure and properties of materials. DFT was developed by Hohenberg and Kohn in 1964 [27], Kohn and Sham in 1965 [28] replacing an interacting many-body problem into a set of single-particle problems treating charge density of electron gas as fundamental, including many-body effects in the exchange-correlation energy functional of density.

2.2.1 Hohenberg-Kohn theorems

The framework of DFT is based on two powerful theorems:

Theorem I: The external potential $V_{ext}(\mathbf{r})$ of any system of interacting particles can be determined uniquely by the ground state particle density $n_0(\mathbf{r})$ within an additive constant.

Theorem II: For any given external potential $V_{ext}(\mathbf{r})$, the universal functional for energy $E[n]$ of the system can be defined in terms of particle density $n(\mathbf{r})$. The exact ground state energy of the system is the global minimum value of this functional, and the density n($\mathbf{r}$) that minimizes this functional is the exact ground state particle density $n_0(\mathbf{r})$.

Based on these two theorems, the $3N_e$ (N_e is number of electrons) variables in the problem are reduced to a problem involving function of only three variables of $n(\mathbf{r})$, and the total energy functional can be written:

$$E_{HK}[n] = F_{HK}[n] + \int d^3 r V_{ext}(\mathbf{r}) n(\mathbf{r}) + E_{II}, \tag{2.4}$$

$$F_{HK}[n] = T[n] + E_{int}[n], \tag{2.5}$$

where E_{II} is the nuclei-nuclei Coulomb interactions. Functional $F_{HK}[n]$ includes kinetic $T[n]$ and potential $E_{int}[n]$ energies of interacting particles system. Though these two theorems prove existence of an universal functional $F_{HK}[n]$ (only a functional of density $n(\mathbf{r})$), they do not provide a practical scheme for determining the ground state density $n_0(\mathbf{r})$, In 1965, Kohn and Sham proposed an anstaz for the ground state density $n_0(\mathbf{r})$ to simplify this.

2.2.2 Kohn-Sham ansatz

Kohn-Sham ansatz [28] is a mathematical assumption that replaces the ground state density of an original interacting many-body system by a system of auxiliary non-interacting particles. Thus, calculations of an original system can be performed on an auxiliary non-interacting particles system with the total energy functional given by,

$$E_{KS} = T_s[n] + \int d\mathbf{r} V_{ext}(\mathbf{r}) n(\mathbf{r}) + E_{XC}[n] + E_H[n] + E_{II}. \tag{2.6}$$

Terms in Eq. (2.6) are described below:

$n(\mathbf{r})$ is charge density of auxiliary system determined by the sum of square of N_e non-interacting electrons′ wavefuctions ($\psi_i(\mathbf{r})$):

$$n(\mathbf{r}) = \sum_{i=1}^{N_e} |\psi_i(\mathbf{r})|^2, \; and \; N_e = \int d\mathbf{r} \; n(\mathbf{r}). \tag{2.7}$$

$T_s[n]$ is the kinetic energy of N_e non-interacting electrons, and given by,

$$T_s[n] = -\frac{\hbar^2}{2m_e} \sum_{i=1}^{N_e} \langle \psi_i(\mathbf{r}) | \nabla^2 | \psi_i(\mathbf{r}) \rangle. \tag{2.8}$$

$E_H[n]$ is the Hartree energy, classical interaction energy of the electron density interacting with itself, and define as,

$$E_H[n] = \frac{e^2}{2} \int \frac{n(\mathbf{r}) n(\mathbf{r}')}{|\mathbf{r} - \mathbf{r}'|} d\mathbf{r} d\mathbf{r}'. \tag{2.9}$$

$E_{XC}[n]$ is the exchange-correlation energy of electrons that takes into account of (i) difference in kinetic energy of the many-body interacting system and set of non-interacting system, and (ii) residual energy contributions due to the exchange asymmetry and correlations. E_{XC} is given by,

$$E_{XC}[n] = (T[n] - T_s[n]) + (E_{int}[n] - E_H[n]), \tag{2.10}$$

where $[n]$ denotes a functional of the electron density $n(\mathbf{r})$. The exact form of $E_{XC}[n]$ is unknown, and will be discussed shortly. In this approch, the Hamiltonian of an auxiliary non-interacting particles is called Kohn-Sham Hamiltonian (H_{KS}), and written as,

$$H_{KS} = -\frac{\hbar^2}{2m_e} \nabla^2 + V_{KS}(\mathbf{r}), \tag{2.11}$$

where $V_{KS}(\mathbf{r})$ is Kohn-Sham potential expressed as,

$$V_{KS}(\mathbf{r}) = V_{ext}(\mathbf{r}) + V_H(\mathbf{r}) + V_{XC}(\mathbf{r}), \tag{2.12}$$

where $V_{ext}(\mathbf{r})$, $V_H(\mathbf{r})$ and $V_{XC}(\mathbf{r}) = \frac{\partial E_{XC}[n]}{\partial n(\mathbf{r})}$ are external, Hartree and exchange-correlation potentials, respectively. Now, one can write single-particle Kohn-Sham equations as,

$$H_{KS}\psi_i(\mathbf{r}) = \epsilon_i\psi_i(\mathbf{r}), \tag{2.13}$$

the solution of Eq. (2.13) is a self-consistent iterative method, and illustrated in Figure 2.1.

2.2.3 Exchange-correlation energy functionals

As mentioned earlier, the exact form of $E_{XC}[n]$ is unknown, and it requires further approximations. Towards this, many approximations have been proposed, and among all available approximations, local density approximation (LDA) [29–31] and generalized gradient approximation (GGA) [32] are the most commonly and widely used schemes to estimate the exchange-correlation energy. In LDA, the exchange-correlation energy density is approximated as that of the uniform electron gas given by its density, while in GGA, it considered as a function of both density and its gradient at each point in the space. GGA leads to a notable improvement over LDA in estimation of energies, and improve the accuracy of many of the ground state properties of materials.

2.2.4 Pseudopotential approximation

Based on the nature of chemical activity of electrons in a material, they can be divided into two types, (i) core electrons, and (ii) valence electrons. It is an established fact that most of the properties of a material can be determined by the

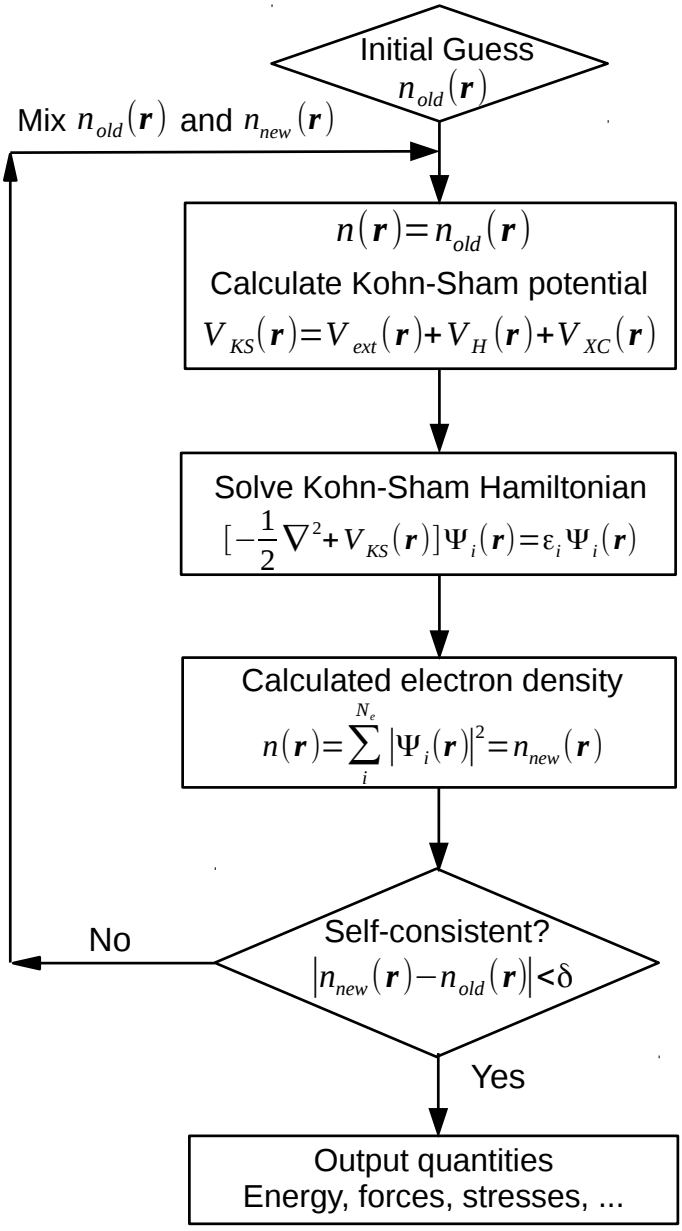

Figure 2.1: Flow chart of the iterative solution of Kohn-Sham equations to achieve self-consistency.

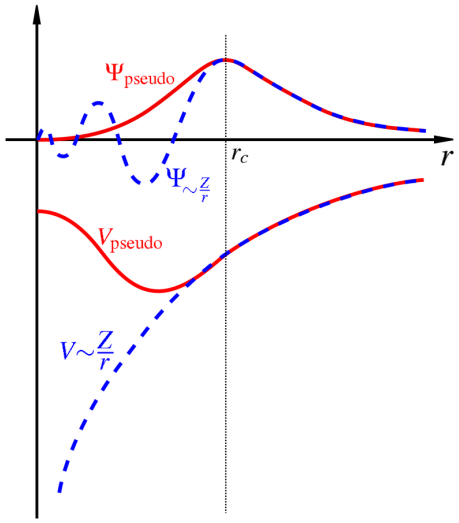

Figure 2.2: Schematic representation of an all electron potential (dotted line) and pseudopotential (solid line) along with corresponding wavefunction. Source of figure: https://en.wikipedia.org/wiki/Pseudopotential.

valence electrons of its atoms, while core electrons are sort of inert. Pseudopotential approximation [33] takes this into account, and removes core electrons by replacing their effects and strong ionic potential by a weak and smooth pseudopotential that act on a group of pseudo wavefunctions of valence electrons (See Fig. 2.2).

The behavior of pseudopotential in different regions of radius r (see Fig. 2.2) is defined by a cut-off radius (r_c). For $r \geq r_c$, all-electron and pseudo wavefunctions of valence electrons are identical. For $r < r_c$, energy eigenvalues and scattering properties are conserved by the pseudo-wavefunctions. If the charge density of each pseudo wavefunction is equal to the charge density of the actual wavefunction inside the region r $< r_c$, the pseudopotential is known as a norm-conserving pseudopotential [34]. This is generalized in ultrasoft pseudopotentials [35], where the total charge in $r < r_c$ region is conserved along with augmented charge density. Ultrasoft pseudopotentials reduce the computational cost significantly while maintaining the accuracy.

2.2.5 Basis set

The basis set is a set of functions that can be used to represent the Kohn-Sham wavefunctions, and transforms the Kohn-Sham equation into the algebraic equation appropriate for computational simulations. Among many possible basis sets, plane-waves [36], atomic orbitals [37, 38] and their combination (mixed basis) [39] are commonly used in first-principles based computational simulations within DFT.

Plane-wave basis set is widely used in the simulations of materials that have periodicity at least in one dimension. In this basis set, Kohn-sham wavefunction of a particle can be represent as,

$$\psi_{i,\mathbf{k}}(\mathbf{r}) = \sum_{|\mathbf{G}|} C_{i,(\mathbf{k}+\mathbf{G})} e^{i(\mathbf{k}+\mathbf{G}).\mathbf{r}}, \tag{2.14}$$

where $\mathbf{G}$ and $\mathbf{k}$ are reciprocal lattice vector and Bloch wave-vector in the Brillouin zone, respectively, and $C_{i,(\mathbf{k}+\mathbf{G})}$ is an expansion coefficient. In practice the sum is truncated by introducing a kinetic energy cutoff (E_{cut}) which determines the number of plane-waves satisfying the following condition:

$$\frac{\hbar^2}{2m_e}|\mathbf{k}+\mathbf{G}|^2 \leq E_{cut}. \tag{2.15}$$

The cutoff energy (E_{cut}) is increased until the calculated energy differences converge to a desired accuracy. Atomic orbitals are used to expand Kohn-Sham wavefunctions of molecules and atomic clusters to calculate their electronic properties. In mixed basis sets, atomic orbitals are incorporated near the nucleus while plane-waves are away from the nucleus as implemented in Linearized Augmented Plane-wave (LAPW) method [40, 41].

2.3 Phonons

Phonon is a quasiparticle and quantum of vibrational energy associated with collective motion of atoms in materials. The concept of phonons provides a powerful tool to study the properties of materials which are governed by atomic displacements. Phonon-dispersion, behavior of vibrational frequency (ω) versus wave-vector ($\mathbf{q}$), reveals interesting physics of materials that governs stability of structures, thermodynamic properties and structural phase transformation of crystalline materials. There are two types of phonons: (i) stable phonons ($\omega^2 > 0$) and (ii) unstable phonons ($\omega^2 < 0$). Frozen-phonon and linear-response methods are the two methods which are commonly used to calculate phonons from first-principles.

2.3.1 Frozen-phonon method

This method involves explicit displacements of each of the atoms in a given crystal structure to calculate induced forces on every atom using Hellmann-Feynman theorem [42]. The force constant matrix ($K_{i\alpha,j\beta}(\mathbf{R})$), $\mathbf{R}$ denotes real space, is the second derivative of total energy E with respect to atomic displacements,

$$K_{i\alpha,j\beta}(\mathbf{R}) = -\frac{\partial F_{i\alpha}}{\partial u_{j\beta}} = -\frac{\partial^2 E}{\partial u_{i\alpha} \partial u_{j\beta}}, \tag{2.16}$$

where i and j are the atomic indexes, and α and β are their cartesian coordinates. $K_{i\alpha,j\beta}(\mathbf{R})$ is the force acting on the α coordinate of i^{th} atom due to the displacement $u_{j\beta}$ in the β direction of j^{th} atom. Phonon frequencies (ω) at any wave-vector ($\mathbf{q}$) can be determined by taking square root of eigenvalues of the dynamical matrix ($D_{i\alpha,j\beta}(\mathbf{q})$) that is the Forurier transformation of $\frac{K_{i\alpha,j\beta}(\mathbf{R})}{\sqrt{M_i M_j}}$.

This method requires a set of total energy calculations using DFT that depends on the number of atoms in the system, and is suitable for the phonon calculations at $\mathbf{q} = 0$, called Γ-point in the Brillouin zone. To calculate phonons where $\mathbf{q} \neq 0$,

we need to use a supercell and its size will be defined by the wave-vector **q**. In this case, the number of atoms increases rapidly and require a large number of total energy calculations which are computationally expensive and time-consuming. The linear-response method overcomes this drawback and provides a computationally feasible tool to calculate full phonon-dispersion.

2.3.2 Linear-response

DFT linear-response (DFT-LR) [43] is an approach to computing the second derivative of the total energy with respect to a given perturbation. Since the force constant matrix is a second derivative of ground state energy with respect to atomic displacements (**u**), the linear-response provides a powerful mechanism to calculate phonons at an arbitrary wave-vector (**q**). This method is efficient and hence widely used in first-principles calculations, and also known as density functional perturbation theory (DFPT). In this approach, the force constant matrix ($K_{i\alpha,j\beta}$) is:

$$K_{i\alpha,j\beta} = \frac{\partial^2 E}{\partial u_{i\alpha} u_{j\beta}} = \frac{\partial^2 E_{ion-ion}}{\partial u_{i\alpha} u_{j\beta}} + \int \frac{\partial^2 V_{ext}(\mathbf{r})}{\partial u_{i\alpha} u_{j\beta}} d\mathbf{r} n(\mathbf{r}) + \int \frac{\partial n(\mathbf{r})}{\partial u_{i\alpha}} \frac{\partial V_{ext}(\mathbf{r})}{\partial u_{j\beta}} d\mathbf{r}. \quad (2.17)$$

It is clear from Eq. (2.17) that $K_{i\alpha,j\beta}$ dependes on the ground state charge density ($n(\mathbf{r})$) and its first-derivative (linear-response) with respect to atomic displacement $\frac{\partial n(\mathbf{r})}{\partial u_{i\alpha}}$. To calculate $K_{i\alpha,j\beta}$, Eq. (2.17) is evaluated within the frame work of first-principles calculations by solving first-order Kohn-Sham equations [28].

2.4 Free-energy

The direct outputs from DFT and DFPT calculations determine the properties of materials at T=0 K. To calculate properties at $T > 0$ K, free-energy becomes an

important quantity. Using phonons, one can estimate free-energy of stable phonons readily using the harmonic approximation. On the other hand, free-energy of unstable phonons is not quite possible because harmonic approximation is not valid for these phonons.

To estimate contributions of *stable phonons* to vibrational free energy, we use harmonic approximation treating them as quantum oscillators [44]:

$$F^{ph}_{stable} = \frac{k_B T}{N_q} \sum_{q,\nu} ln[2sinh(\frac{\hbar\omega_{q\nu}}{2k_B T})], \tag{2.18}$$

where F^{ph}_{stable} vibrational free energy of stable phonons of the optimized structure. $\omega_{q,\nu}$ is the frequency of ν phonon mode at q wave-vector, and N_q is the number of q wave-vectors. Since Eq. (2.18) does not hold for *unstable phonons* ($\omega^2 < 0$), we determine* [45] their contributions to vibrational free energies by treating them as quantum *anharmonic* oscillators (QAOs). We include fourth-order anharmonic term in Hamiltonian of unstable modes:

$$H = -\frac{1}{2}\frac{\hbar^2}{M_{q\nu}}\frac{\partial^2}{\partial u^2_{q\nu}} + V(u_{q\nu}), \tag{2.19}$$

$$V(u_{q\nu}) = -\frac{1}{2}M_{q\nu}\omega^2_{q\nu}u^2_{q\nu} + \frac{1}{4}k_4 u^4_{q\nu}, \tag{2.20}$$

where $V(u_{q\nu})$, $M_{q\nu}$, $\omega_{q\nu}$ and $u_{q\nu}$ are anharmonic potential, effective mass, imaginary part of frequency and amplitude of the normalized eigenvector ($|\hat{u}_{q\nu}>$) of unstable phonon mode ν at q wave-vector in BZ, respectively. k_4 is the coefficient of fourth-order anharmonic force constant of ν, and it must be positive. The effective mass ($M_{q\nu}$) of a phonon mode is $M_{q\nu} =< \hat{u}_{q\nu}|M|\hat{u}_{q\nu} >$, where M is the diagonal

*Published in Materialia **9**,100602 (2020)

mass matrix. We used values of $\omega_{q\nu}$, M and $|\hat{u}_{q\nu}>$ from the DFT-LR calculations, and the value of k_4 was estimated by fitting to the double-well potential calculated by freezing unstable phonon modes.

To solve Schrödinger equation of Hamiltonian of unstable modes, we used higher-order finite difference formula of the kinetic energy operator on a uniform grid in real-space [46] of $u_{q\nu}$:

$$\frac{\partial^2}{\partial u_{q\nu}^2}\psi_{q\nu l}(u_{q\nu i}) = \frac{1}{h^2}\sum_{n=-N}^{N} C_n \psi_{q\nu l}(u_{q\nu(i+nh)}) + O(h^{2N+2}) \tag{2.21}$$

where h is the grid spacing, $\psi_{q\nu l}(u_{q\nu i})$ is quantum mechanical wavefunction of the l^{th} excited state of phonon ν at q-point in BZ. C_n being the coefficients of finite difference formula [46], N is the order of finite difference approximation, which is accurate to $O(h^{2N+2})$. We use N=6 and employ Eq. (2.19) and (2.21) in setting up the Schrödinger equation as follows.

$$-\frac{1}{2h^2}\frac{\hbar^2}{M_{q\nu}}\sum_{n=-N}^{N} C_n \psi_{q\nu l}(u_{q\nu(i+nh)}) + V(u_{q\nu})\psi_{q\nu l}(u_{q\nu i}) = E_{q\nu l}\psi_{q\nu l}(u_{q\nu i}), \tag{2.22}$$

where $E_{q\nu l}$ is the l^{th} energy eigenvalue of ν phonon mode at q-point. We diagonalized H matrix and find its energy spectrum. Using this spectrum, we calculate the partition function $Z_{q\nu}$ as,

$$Z_{q\nu} = \sum_{l=0}^{H} e^{-E_{q\nu l}/k_B T}, \tag{2.23}$$

$$Z_{q\nu} = e^{-E_{q\nu 0}/k_B T}\{1 + \sum_{l=1}^{H} e^{-(E_{q\nu l}-E_{q\nu 0})/k_B T}\}, \tag{2.24}$$

$$lnZ_{q\nu} = -E_{q\nu 0}/k_bT + ln\{1 + \sum_{l=1}^{H} e^{-(E_{q\nu l} - E_{q\nu 0})/k_BT}\}, \quad (2.25)$$

where H labels the highest energy excited state in our analysis of phonon ν. $E_{q\nu 0}$ is ground state energy of ν phonon at q wave vector in BZ. Factoring it out of the logarithmic function in Eq. (2.25), we ensure that $(1 + \sum_{l=1}^{H} e^{-(E_{q\nu l} - E_{q\nu 0})/k_BT}) > 0$ for all excited states, enabling estimations of logarthimic function. We choose the cut-off exciting state (H) such that $exp(-E_{q\nu l}/k_BT)$ is negligible at room temperature, and calculate contribution to free energy of each unstable phonon mode ν as,

$$F^{ph}_{unstable} = -\frac{k_BT}{N_q} \sum_{q,\nu} lnZ_{q\nu}, \quad (2.26)$$

$$F^{ph}_{unstable} = \frac{1}{N_q}[\sum_{q,\nu} E_{q\nu 0} - k_BT \sum_{q\nu} ln[1 + \sum_{l=1}^{H} e^{-(E_{q\nu l} - E_{q\nu 0})/k_BT}], \quad (2.27)$$

where N_q is the number of q wave vectors in the BZ, using Eq. (2.27), we calculate the free energy of unstable phonons. Using Eq. (2.18) and (2.27), we estimate the total free energy as follows:

$$F_H = E + F^{ph}_{stable} + F^{ph}_{unstable}, \quad (2.28)$$

where E and F_H are the total and Helmholtz-free energies of the optimized structure, respectively.

2.5 Method of lattice Wannier functions

Lattice Wannier functions (LWFs) are the localized modes in the real space, obtained through Fourier transformation of phonon normal modes [47–49], and a phonon

analogue of electronic Wannier functions [50, 51]. The lattice Wannier basis vectors span in an invarient subspace of atomic displacements, and is determined by phonon normal modes. For a phonon mode the Wannier basis vector can be written as,

$$w_{i,\nu} = \frac{1}{N}\sum_{\vec{q}} exp(i\phi_{\nu}(\vec{q}))exp(-i\vec{q}\cdot\vec{R}_i)e_{\vec{q},\nu}, \tag{2.29}$$

where $w_{i,\nu}$ is the Wannier basis vector in the i^{th} unit cell of crystal structure in real space corresponding to frequency band of phonon modes ν. $\phi_{\nu}(\vec{q})$ is a phase factor in reciprocal space, and its value always chosen typically to maximize the localization of $w_{i,\nu}$. This localized basis in real space facilitates construction of an effective Hamiltonian to study the structural transformations in which the product phase is linked by lattice distortion and atomic displacements in the parent phase.

2.5.1 Effective Hamiltonian approach

The form and invariant subspace of effective Hamiltonian (H_{eff}) constructed using LWFs to study the structural transformations are material-specific. These depend strongly on the crystal symmetry of the parent structure of materials and its unstable phonon modes involved in this transformation. In this approach, the Wannier basis coordinates span an invariant subspace containing the unstable phonon modes that link parent and product structures through lattice distortions that occur during the transformation. Localized Wannier basis coordinates that define the invariant subspace can be determined using Eq. 2.29 for a set of phonon modes (ν) at high-symmetry $\vec{q}$ wave-vectors.

We implemented this effective Hamiltonian approach to investigate the important physics of martensitic transformation in MTi (M = Ni and Pt) shape memory alloys and pure titanium. We follow the scheme of lattice Wannier functions (LWFs) in

Ref. [22], and identify the symmetry invariant subspaces of the relevant degrees of freedom using full phonon dispersion of the cubic lattice (B2 for shape memory alloys and two atoms basis β for titanium) obtained along the high-symmetry directions in the BZ. The symmetry analysis of the invariant subspaces of the B2 structure of MTi that have two non-identical atoms in the unit cell allows us to divide LWFs into two subspaces labelled by atomic positions (M and Ti) with irreducible representations of a vector. Using symmetries and eigenvectors of the zone boundary phonons, we determine M-centric $\{\vec{\eta}\}$ and Ti-centric $\{\vec{\tau}\}$ localized LWFs to span these subspaces of B2 structure's phonons. Using the cubic symmetry, we express H_{eff} as an explicit symmetry invariant Taylor expansion in $\vec{\eta}_i$, $\vec{\tau}_i$ and homogeneous strains ($\varepsilon_{\alpha\beta}$), i indicates the lattice unit cell $\vec{\eta}_i$ and $\vec{\tau}_i$ belong to. H_{eff} consists of four parts:

$$H_{eff} = H^{M}_{eff}(\vec{\eta}_i) + H^{Ti}_{eff}(\vec{\tau}_i) + H_{spc}(\vec{\eta}_i, \vec{\tau}_i, \varepsilon_{\alpha\beta}) + H_{elastic}(\varepsilon_{\alpha\beta}), \tag{2.30}$$

where $H^{M}_{eff}(\vec{\eta}_i)$ and $H^{Ti}_{eff}(\vec{\tau}_i)$ operate in subspaces of phonons dominated by M (Ni and Pt) and Ti atomic displacements, respectively. $H_{elastic}(\varepsilon_{\alpha\beta})$ contains linear and nonlinear elastic energy of homogeneous strain $\varepsilon_{\alpha\beta}$, and the coupling of $\varepsilon_{\alpha\beta}$ with both sets of LWFs is included in $H_{spc}(\vec{\eta}_i, \vec{\tau}_i, \varepsilon_{\alpha\beta})$. The detailed derivation of H_{eff} and a procedure for determining its material specific parameters are presented in Section 3.5 of chapter 3, and the same form of this Hamiltonian is also used in analysis of MT in PtTi (chapter 4). In contrast to NiTi and PtTi, BCC structure of Ti has identical atoms at M and Ti sites of conventional unit cell of its parent phase. In the effective Hamiltonian of Ti, we thus do not distinguish the two LWFs subspace, and use the modified form of Eq. 2.30 to investigate martensitic transformation in titanium and its full details are presented in chapter 5.

2.6 Monte-Carlo simulations

Temperature-dependent properties of a material can be calculated using its partition function, once the material-specific Hamiltonian in terms of relevant degrees of freedom is available. This Hamiltonian can be readily simulated using Monte Carlo simulations to study temperature-dependent phenomena. Monte Carlo simulations are based on stochastic integration sampling with random numbers and provide estimates of the statistical averages of physical quantities of a model material. In our work, we studied martensitic transformations exhibited by the effective Hamiltonian with Monte Carlo simulations on the $L \times L \times L$ periodic system of the parent phase using the Metropolis algorithm for updating the configurational variables in the model system.

2.7 Periodic generalization of Landau theory: Fourier-Landau theory

Landau theory models free energy function of the order parameters of phase transformations typically expressed as symmetry allowed polynomial using the parent phase as the reference. It captures the physics of all symmetry equivalent ordered states. In some phase transformations (chapter 6), it has been found that free energy is a periodic function of order-parameter. In this case, conventional Landau theory needs to be generalized to a Fourier series to capture the translational symmetry of the crystalline lattice, we called it Fourier-Landau theory, and the free energy per unit volume becomes,

$$\frac{F(u)}{V} = \frac{F_0}{V} + \sum_{n=1}\{a_n cos(\frac{2n\pi}{u_0}u) + b_n sin(\frac{2n\pi}{u_0}u)\} + g\int dx|\frac{du}{dx}|^2, \quad (2.31)$$

where F_0, a_n's and b_n are the Fourier coefficients. V is volume of unit cell, u_0 denotes the translational symmetry of the crystal lattice. Last term denotes the kinetic energy, for $g > 0$, its clear that energy will be minimized if $|u|$ does not vary along x. Coefficients in Eq. 2.31 can be determined easily by first-principles calculations. The Fourier-Landau theory provides a unified description of microstructure and structural transformations.

Chapter 3

Martensitic Structural Transformation in NiTi: A Shape Memory Alloy

3.1 Introduction

Shape Memory Alloys (SMAs) are of great importance to technologies ranging from medical stents to smart structures in the aerospace industry. They exhibit a shape memory effect (SME), in which a highly deformed material recovers its predetermined shape upon heating [52]. Fundamental to the SME is the martensitic transformation (MT), in which the high-temperature cubic austenite structure changes to a low-temperature martensite structure [53] through a non-diffusive first-order phase transition involving atomic displacements (phonons) and large deformations in the crystal shape (strain) [54]. MT in SMAs has been investigated through experimental [55–59] and theoretical studies over the past few decades [60–64]. While Nitinol (NiTi) is the prototypical member of an important class of SMAs, a clear

*This work has been published in *Materialia*, **9**, 100602 (2020). Reproduced by permission of Elsevier, URL: https://doi.org/10.1016/j.mtla.2020.100602

understanding of the precise mechanisms of MT and relative stability of its various low-symmetry structures relevant to its SME are still lacking.

Depending on the composition of NiTi-based alloys, their MT involves five crystal structures: B2 (cubic, space group (SG) $Pm\bar{3}m$), R (trigonal, SG $P3$) [65], B19 (orthorhombic, SG $Pmma$), B19′ (monoclinic, SG $P2_1/m$) and BCO (base-centered orthorhombic, SG $Cmcm$) [66], a special case of B19′ structure with lattice parameters satisfying certain geometric conditions. At high-temperatures, these alloys have the cubic B2 structure, which deforms spontaneously through one of the three transition pathways (Fig. 36 of Ref. [67]) to low-symmetry structures upon cooling. The transformation from B2 → B19′ occurs in quenched NiTi, B2 → R → B19′ occurs in Ni_4Ti_3 and B2 → B19 → B19′ occurs in ternary $Ti_{49.5}Ni_{45.5}Cu_{5.0}$ and quaternary $Ti_{50}Ni_{44}Cu_5Al$ alloys [68]. Fundamental understanding of the microscopic coupling governing these transition pathways is essential to design of improved NiTi-based shape memory alloys.

Several first-principles studies of NiTi [65, 66, 69–71] focused on accurate prediction of structural parameters of its low-temperature phases and their electronic and vibrational properties, complementing the experimental results. In earlier theoretical works on NiTi [72, 73], B19 phase was found to be a relevant metastable phase, and it was suggested that the MT occurs in two steps B2 → B19 → B19′. However, this was suggested to be unlikely in a recent work of Strachan et al. [69], who showed that B19 phase is unstable. Seminal first-principles theoretical analysis of Huang et al. [66] showed that the BCO structure is the ground state of NiTi, while it is yet to be observed experimentally. More importantly, single crystal BCO structure can not store shape memory at atomic-scale because it is connected to B2 structure along non-unique atomistic paths of transformation.

Thus, theoretical prediction of BCO as the ground state structure of NiTi had been a puzzling result. Haskins et al. [63] resolved this puzzle by determining the

free energies of B19′ and BCO structure using thermodynamic integration within *ab initio* molecular dynamics (AIMD). They confirmed that BCO is the ground state structure of NiTi, while B19′ structure gains stability at $T > 75$ K. Some of the recent theoretical works used molecular dynamics (MD) [74–76] to simulate temperature-dependent structural phase transformation in NiTi, with a semiempirical model derived from the second-moment approximation of tight-binding method. With focus primarily on the transition temperature (T_M), their estimates of T_M are in good agreement with experiment of NiTi. Haskins et al. [63] performed AIMD simulations to estimate free energies along the path of transformation between B2 and B19′ structures. Their estimate of the transformation temperature is approximately 500 K, which is about 180 K above experimental results [77]. However, the microscopic picture and interactions governing the MT are not quite clear.

The monoclinic B19′ structure of NiTi stores its shape memory, as it undergoes a reversible transformation upon heating to the B2 phase involving $\{0\bar{1}1\}\langle 011\rangle$ shuffle and $\{100\}\langle 011\rangle$ non-basal shear. In the absence of non-basal shear, B2 transforms into the B19 structure [78, 79]. Elastic moduli of the cubic structure corresponding to $\{0\bar{1}1\}\langle 011\rangle$ basal shear and $\{100\}\langle 011\rangle$ non-basal shear are $C'=(C_{11}-C_{12})/2$ and C_{44} respectively, and their ratio is called the anisotropy factor A$= C_{44}/C'$. Ren and Otsuka [80] presented a Landau-like model to study MT in NiTi taking into account $\{0\bar{1}1\}\langle 011\rangle$ shuffle, $\{100\}\langle 011\rangle$ non-basal shear and $\{0\bar{1}1\}\langle 011\rangle$ basal shear as three order parameters, and determined their contributions in different phases of NiTi. Otsuka et al. [67] proposed that a material with $10 < A < 20$ exhibits a B2 to B19 transformation, while a material with the smaller value of A (~ 2) exhibits B2 to B19′ transformation. Anisotropy factor (A) is a physically sensible *macroscopic* descriptor, as its large value essentially means stabilizing B19 structure as the non-basal shear is suppressed in the low-temperature phase due to high energy ($\propto C_{44}$) cost. They also highlighted that $\{0\bar{1}1\}\langle 011\rangle$

shuffle is related to softening of M-point phonons [67]. Though strain and phonon softening provide important information relevant to the MT, it is not clear (i) what the primary and secondary order parameters are, and (ii) which strain-phonon coupling drives the MT to B19 versus B19′ structures. Indeed, the pathway of MT depends on a delicate competition between different microscoping couplings between phonons and strain, and a quantitatively accurate microscopic model and its theoretical analysis are needed to understand the material-specific physics of MT.

In this chapter, we present detailed *ab initio* and Landau theoretical analysis of the MT in NiTi with focus to uncover microscopic mechanisms and couplings. While the martensitic transformation involves twin and planar fault structures deviating from the single crystalline phases, our goal here is to analyze the single crystal structural transformation the B19′ phase to B2 phase with temperature. In Sec. 3.2, we present details of the methodology used in our first-principles calculations, structural parameters and energies of NiTi phases. In Sec. 3.3, we present T-dependent vibrational free energies of B19, B19′ and BCO structures, adding to the resolution of puzzling issue of their relative stability of B19′ and BCO structures of NiTi. In Sec. 3.4, we uncover the relevant order parameters of MT and their relationship with phonons and strain. In Sec. 3.5, we present an effective Hamiltonian (H_{eff}) with parameters determined to capture the low energy landscape of various NiTi structures. In Sec. 3.6, we present results of Monte Carlo simulations of H_{eff} to determine temperature and pressure dependent MT, uncovering the soft mode behavior. We present Landau theoretical analysis in Sec. 3.7 to identify specific couplings in H_{eff} that stabilize B19 and B19′ phases. In Sec. 3.8, we present results of structural disorder and microstructures relevant to MT in NiTi using H_{eff} analysis, and finally conclude our work in Sec. 3.9.

3.2 First-principles computational details and structural parameters

Our first-principles calculations within the density functional theory (DFT) were performed with a plane-wave pseudopotential scheme implemented in the Quantum Espresso (QE) package [81], with a generalized gradient approximation (GGA) and Perdew-Burke-Ernzerhof (PBE) [32] form of exchange-correlation energy functional. In self-consistent Kohn-Sham (KS) calculations with primitive unit cells, the Brillouin Zone (BZ) integrations were sampled on uniform meshes of $18 \times 18 \times 18$ k-meshes for B2 structure, and $18 \times 12 \times 12$ k-meshes for B19, B19$'$ and BCO structures, and note that these uniform k-meshes include Γ-point.

To check the accuracy of our quantum-mechanical calculations, specially the energy of B19$''$ (at $\gamma =\sim 101^o$, a monoclinic structure intermediate to B19$'$ and BCO [69]) relative to B19$'$ (at $\gamma =\sim 97.8^o$) and BCO structures (which is within $\sim$1 meV), we tested the convergence of total energies with respect to energy cutoffs used to truncate the plane-wave basis representing the Kohn-Sham wave functions (Fig. 3.1). While total energies of these structures shifted with increasing the energy cutoff and converged at 100 Ry (Fig. 3.1), their relative energies do not change above the cutoff energy of 40 Ry. We thus performed the structural optimization calculations at energy cutoffs of 40 Ry.

We relaxed B19$'$ structure to minimize energy with respect to atomic positions keeping lattice parameters fixed at these in Ref. [66] until the force on each atom is less than 2 meV/$\mathring{A}$. At these lattice parameters of B19$'$, shear stresses ($\sigma_{xy} = -10.5$ kbar) are a bit high, and the structure is thus not completely optimized. When B19$'$ structure is relaxed with respect to both lattice parameters and atomic positions until the magnitude of stresses are less than 0.1 kbar (and force on each atom is less than 2 meV/$\mathring{A}$), it transforms into B19$''$ structure. Thus, it is clear that B19$'$

at experimental lattice parameters is unstable with respect to B19″ (Table 3.1). Optimization of the BCO structure with respect to its atomic positions and lattice parameters relaxed until the magnitude of stresses are less than 0.1 kbar (and force on each atom is less than 1 meV/$\mathring{A}$), and it is lower in energy with respect to B19″ structure (Table 3.1).

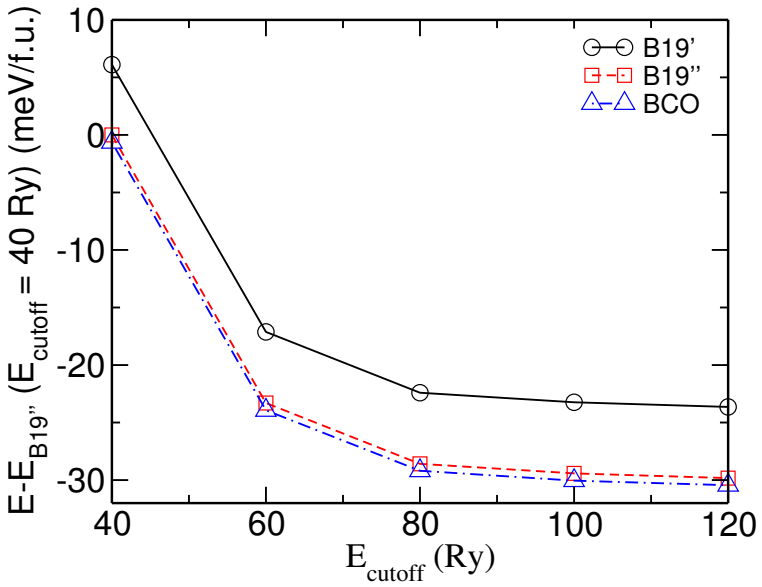

Figure 3.1: Total energies of B19′ (black), B19″ (red) and BCO (blue) structures of NiTi with respect to B19″ at 40 Ry energy cutoff.

We reconfirm structural parameters and relative energies of the structures of NiTi using (i) local density approximation (LDA) as parametrized by Perdew-Zunger [82] pseudopotential implemented in QE at energy cutoffs of 50 Ry and 400 Ry to truncate the plane-wave basis set for representing Kohn-Sham wavefunctions and charge density respectively at the uniform mesh of 20 × 16 × 16 k-points, and (ii) SCAN meta-GGA exchange-correlation functional [83, 84] as implemented in the VASP code [85, 86] along with projector augmented wave (PAW) potentials [87]. Our estimates of structural parameters and energies of B2, B19, B19′, B19″ and BCO phases of NiTi agree well with earlier theoretical works [69, 88–90], structural parameters of B2 and B19′ structures agree well with experiments [55, 57] as well,

and reconfirm that BCO is the most stable of the structures of NiTi (Table 3.1), though their relative energies depend on the flavor choice of (exchange-correlation energy functional) of DFT. We refer to B19″ as B19′ in our rest of analysis, as both the structures are monoclinic and exhibit SME [69].

Table 3.1: Structural parameters (4 atoms per unit cell) and energies of B2, B19, B19′, B19″ and BCO phases of NiTi relative to B19″ structure as a reference, obtained with different computational schemes.

Phase	Space group	Method	a($\mathring{A}$)	b($\mathring{A}$)	c($\mathring{A}$)	γ^o	$E - E_{B19''}$ (meV/f.u)
B2	$Pm\bar{3}m$	PBE-GGA	3.004	4.248	4.248	90	75.3
		PZ-LDA	2.937	4.153	4.153	90	112.1
		SCAN metaGGA	2.966	4.195	4.195	90	156.7
		USPP-GGA [66]	3.009	4.255	4.255	90	84.0
		Exp [55]	3.015	4.264	4.264	90	
B19	Pmma	PBE-GGA	2.832	4.589	4.168	90	28.3
		PZ-LDA	2.644	4.553	4.165	90	19.8
		SCAN metaGGA	2.805	4.565	4.097	90	45.9
		USPP-GGA [66]	2.776	4.631	4.221	90	24.0
B19′	$P2_1/m$	PBE-GGA	2.929	4.686	4.048	97.8	4.9
		USPP-GGA [66]	2.929	4.686	4.048	97.8	0.0
		PAW-GGA [69]	2.929	4.686	4.048	97.8	1.6
		PBE-GGA [88]	2.933	4.678	4.067	98.3	6.0
		PBE-GGA [89]	2.732	4.672	4.234	95.3	16.0
		Exp [57]	2.898	4.646	4.108	97.8	
B19″	$P2_1/m$	PBE-GGA	2.935	4.733	4.027	100.9	0.0
		PZ-LDA	2.846	4.722	3.932	103.8	0.0
		SCAN metaGGA	2.907	4.726	3.953	101.9	0.0
		PAW-GGA [69]	2.945	4.769	4.034	101.8	0.0
		PBE-GGA [88]	2.923	4.801	4.042	102.4	0.0
		PBE-GGA [89]	2.917	4.780	4.047	100.0	0.0
		PAW-GGA [90]	2.916	4.767	4.032	102.2	0.0
BCO	Cmcm	PBE-GGA	2.928	4.910	4.006	107.1	-1.6
		PZ-LDA	2.851	4.813	3.923	107.1	-2.2
		SCAN metaGGA	2.891	4.888	3.937	107.3	-0.4
		USPP-GGA [66]	2.940	4.936	3.997	107.0	-16.0
		PAW-GGA [69]	2.932	4.926	4.012	107.3	-2.2
		PBE-GGA [88]	2.928	4.923	4.017	106.6	-5.0
		PBE-GGA [89]	2.914	4.927	4.021	107.3	-1.0
		PAW-GGA [90]	2.916	4.901	4.015	107.3	-1.0

We determined dynamical matrices and phonon spectra within the framework of DFT linear response (DFT-LR) at q-points on a $6 \times 6 \times 6$ mesh for B2, and

$2 \times 2 \times 2$ mesh in the BZ for B19, B19′ and BCO structures implemented in QE. We estimated the free-energies of B19, B19′ and BCO structures of NiTi using,

$$G(S) = E(S) + F^{ph}_{stable}(S) + F^{ph}_{unstable}(S), \tag{3.1}$$

where $E(S)$ and $G(S)$ are the total and free energies of the optimized structures S, respectively. $F^{ph}_{stable}(S)$ and $F^{ph}_{unstable}(S)$ are the vibrational free energies of stable and unstable phonons, respectively (details of methods to compute these terms are presented in Chapter 2, Sec 2.4).

3.3 Resolution of the puzzle of relative stability of B19′ and BCO structures

Each Ti atom in B19′ phase has seven first nearest neighbor (NN) Ni atoms (three in $(001)_{B19'}$ plane and four in $(010)_{B19'}$ plane) at a distance 2.55 $\mathring{A}$ and one second NN Ni atom in $(001)_{B19'}$ plane at a distance 4.27 $\mathring{A}$ (Fig. 3.2a), which are related to eight of its first NN Ni atoms at a distance 2.60 $\mathring{A}$ ($\sqrt{3}a/2$) in the B2 structure (a is the lattice parameter of B2 structure). In B2 to B19′ transformation, one of the eight NN Ni atoms in B2 structure becomes the second NN in B19′ structure and vice versa. Since only one Ni atom (per Ti atom) is involved in the change in the NN environment of the B19′ structure, it allows to remember the structural path of transformation and the shape of the B2 structure. In contrast, each Ti atom in the BCO structure has seven first NN Ni atoms (three in $(001)_{BCO}$ plane and four in $(010)_{BCO}$ plane) at a distance 2.56 $\mathring{A}$, and *two* identical second NN Ni atoms in $(001)_{BCO}$ plane at a distance 3.89 $\mathring{A}$ (Fig. 3.2b). During the transformation of BCO to B2 structure, either of the second NN Ni atoms can become the first NN Ni atom of Ti in B2 structure. Thus, the BCO to B2 transformation can occur along

more than one symmetry equivalent atomistic pathways, involving evolution of any one of the two Ni atoms in the second shell of Ti in BCO to the first neighbour Ni of B2 structure, and hence the BCO structure does not memorize at the atomic scale the shape of B2 phase uniquely, as shown in Ref. [66]. However, the shape memory could be stored at micro-structural level and through its transformation to B19′ phase stabilized under residual internal stresses.

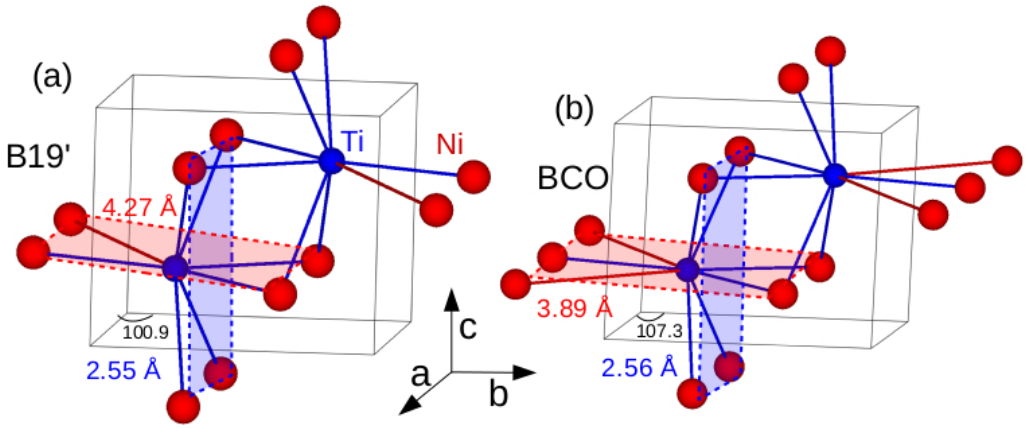

Figure 3.2: Subtle difference between B19′ (at $\gamma = 100.9^0$) (a) and BCO (at $\gamma = 107.3^0$) (b) structures of NiTi. Blue and red bonds connect a Ti (blue) atom with its first and second nearest neighbors Ni (red) atoms respectively. The second nearest neighbor sites of Ti are occupied by two and one Ni atoms in BCO and B19′ structure respectively.

We note that the puzzling issue of BCO as the ground state structure of NiTi has been resolved by Haskins et al. [63], who obtained free energies of these structures from AIMD and showing that the B19′ structure stabilizes above $T > 75$ K. We note that their analysis is based on *classical* statistical mechanics, and we complement it here with quantum statistical mechanics, in which Bose-Einstein statistics of phonons is used. We determined their phonon spectra using DFT linear response (DFT-LR), and confirm the results of Ref. [61, 63–65] that $M_{5'}$ phonon mode is the strongest lattice instability of B2 structure ($\omega \sim 57i\ cm^{-1}$, Fig. 3.3a). In B19 structure, one of the transverse acoustic (TA) phonon branches is weakly unstable ($\omega \sim 33i\ cm^{-1}$) along $\Gamma \rightarrow Y$ direction (Fig. 3.3b), little different from the results

of Ref. [65] which do not show any imaginary frequency along $\Gamma \rightarrow Y$ direction. A TA phonon branch in $\Gamma \rightarrow E$ direction of B19′ structure exhibits a weak instability ($\omega \sim 8i\ cm^{-1}$, Fig. 3.3c) in our analysis, slight different from the results of Ref. [63–65] (where no imaginary frequency phonons found along $\Gamma \rightarrow E$ direction). We note that unstable modes are expected in the phonon spectra of B19 and B19′ as they are consistent with this instability (against shear strain) of these structures with respect to BCO structure [66]. Our calculated phonon dispersion of the BCO structure, the ground state, exhibits no instability anywhere in the BZ (Fig. 3.3c), and is in good agreement with Ref. [63, 64].

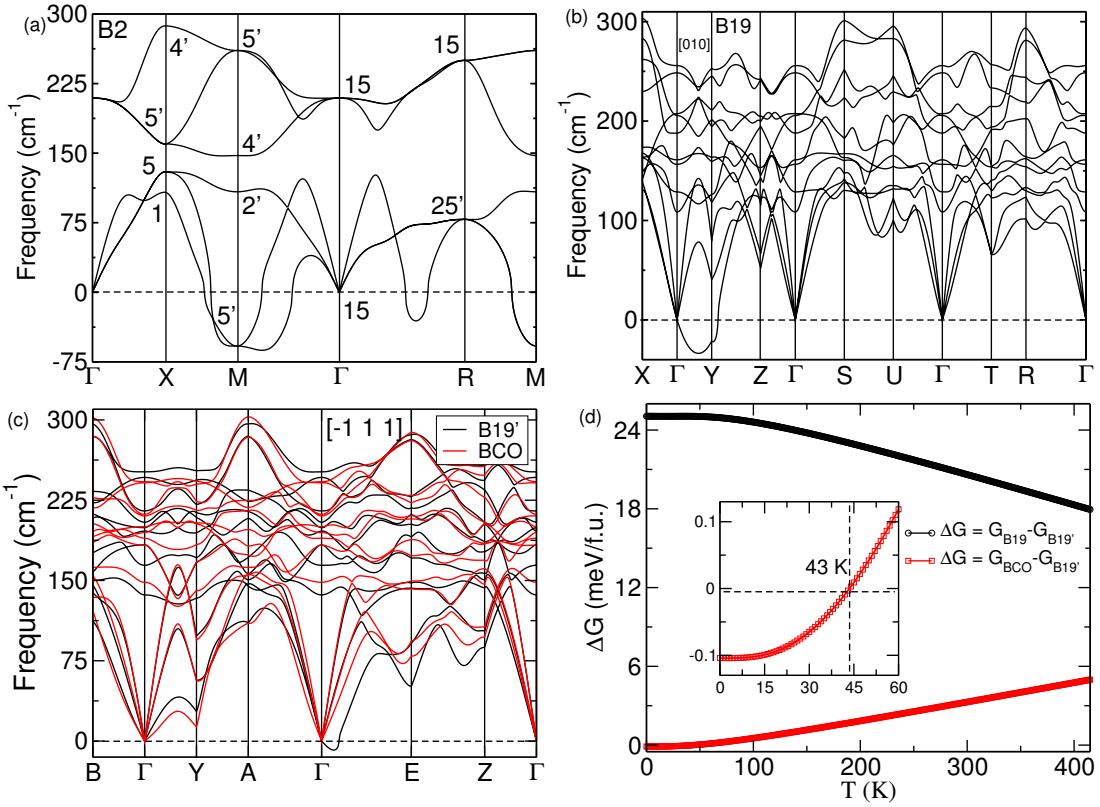

Figure 3.3: Phonon spectra along high-symmetry lines of B2 (a), B19 (b), B19′ (black) and BCO (red) (c) structures of NiTi obtained using DFT-LR calculations. Unstable modes with imaginary frequencies ($\omega^2 < 0$) are shown with negative values. Difference between free-energies of B19 and B19′ structures (black line) and BCO and B19′ structures (red line) (d).

We now estimate the free energies of B19, B19′ and BCO structures using

Eq. (3.1), and we find $\Delta G = G_{B19} - G_{B19'} >$ 18 meV/f.u. at T up to temperatures 400 K, and thus conclude that B19 structure is unlikely to occur at low-T. At T = 0 K, $\Delta G = G_{BCO} - G_{B19'}$ = -0.10 meV/f.u. (while this is within the error of our computations, we have tested its convergence with respect to q-mesh), revealing nearly equal stability of BCO and B19′ structures within our error bars. However, at T > 43 K B19′ structure gain the stability over BCO structure (Fig. 3.3d). We confirm the transformation from BCO to B19′ structure as it was studied earlier using AIMD [63], and quasi-harmonic approximation (QHA) [64]. Our estimate of transformation temperature from BCO to B19′ is lower than that in Ref. [63] because of the quantum statistical approach used here versus classical approach used in their work (zero-point motion typically suppress the ordering at low-T), and Ref. [64] (at T = 100 K). However, the BCO phase deforms readily and transforms to $B19'$ phase in the response to stresses, and shape memory effect is thus strongly influenced by stresses and planar twining faults.

3.4 Identification of order parameters

We now identify the order parameters of the MT in NiTi by deriving atomic positions and lattice vectors of its low-symmetry B19 and B19′ structures as changes or distortions of the reference B2 structure expressed in terms of its phonon modes and strains respectively. While $M_{5'}$, $M_{2'}$ and $M_{4'}$ phonons are involved in the transformation of B2 to B19′ (Fig. 3.4a-3.4c, 3.4e), $M_{5'}$ phonon alone drives the B2 to B19 structural transformation (Fig. 3.4a, 3.4d). Dominant structural instability of $M_{5'}$ mode makes it the order parameter common to both B2 → B19 and B2 → B19′ phase transformations. The quantitative estimation of phonons and strains involved in transformations to B19 and B19′ structures of NiTi are listed in Table 3.2. While we find that $\{0\bar{1}1\}<011>$ basal shear does not constitute an order parameter of any

of these structures, it can arise when the transformation occurs under applied stress as seen in earlier reports [78, 79]. It is evident from our analysis that Bain strain, pure shear and hydrostatic strains are involved in B2 to B19 (and B19′) transformations. In B2 to B19 transformation, we find only four order parameters ($M_{5'}$, s_2, s_3 and s_4), while in B2 to B19′ seven order parameters ($M_{5'}$, $M_{2'}$, $M_{4'}$, s_2, s_3, s_4 and s_5) are involved. Thus the couplings of {100}<011> non-basal shear deformation with $M_{2'}$ and $M_{4'}$ phonons are expected to be relevant to the transformation to B19′ structure. The dependence of secondary order parameters on the primary order parameter is nonlinear (See Fig. 3.5); hence we can not combine them into a single one as a linear combination.

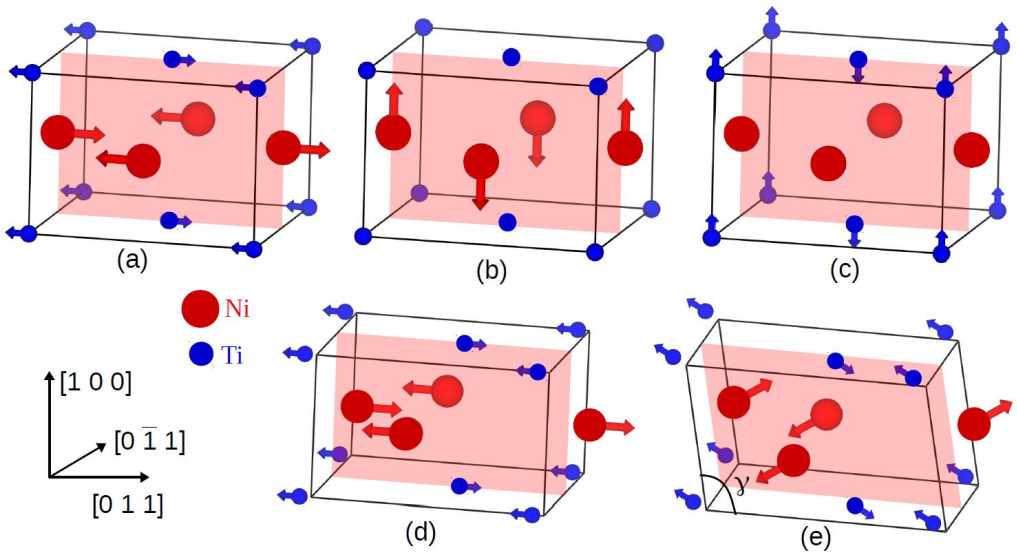

Figure 3.4: Order parameters of B2 → B19 and B2 → B19′ structural transformations. Atomic displacements of $M_{5'}$ (a), $M_{2'}$ (b) and $M_{4'}$ (c) modes at $\vec{q} = \frac{\pi}{a}(011)$, shown in $1\times\sqrt{2}\times\sqrt{2}$ supercell of B2 structure. While $M_{5'}$ phonon and orthorhombic strain of supercell of B2 give B19 structure (d), $M_{5'}$, $M_{2'}$, $M_{4'}$ modes and monoclinic strain together give B19′ structure (e). The planar unit shaded with light red colour at $c/2$ distance along [0 $\bar{1}$ 1] direction contains one Ti (blue) and one Ni (red) atom on its edges-centers.

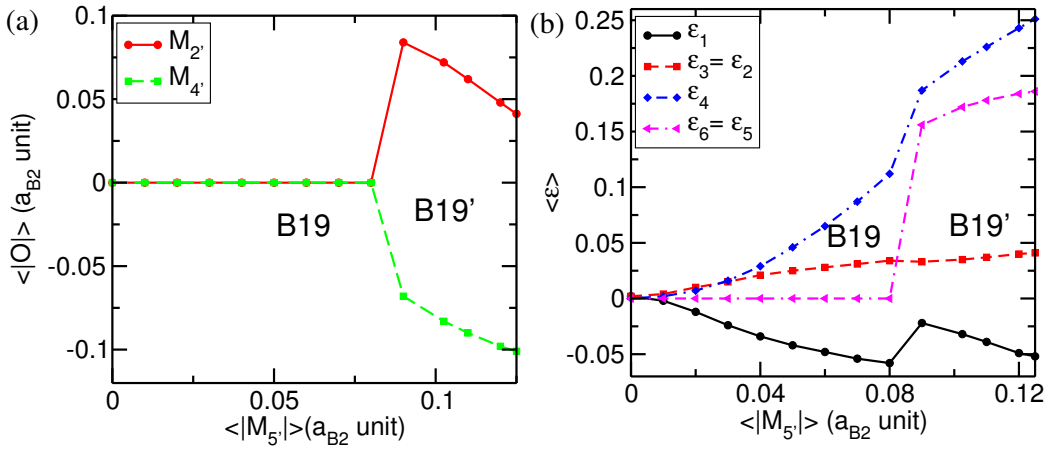

Figure 3.5: Dependence of secondary order parameters, $M_{2'}$ and $M_{4'}$ (a) strain order parameter (b) on the primary order parameter $M_{5'}$. In B2 structure all order parameters are zero.

3.5 Construction of effective Hamiltonian

Having identified the relevant phonons and strains, we now construct an effective Hamiltonian (H_{eff}) that models the low-energy landscape of NiTi with special attention to these phonons, strains and their interactions. Since the BCO structure occurs in a vanishingly small subspace of configurations given by certain geometric conditions on B19′ structural parameters, and their relative stability depends on quantum vibrational energy not captured by Monte Carlo or Molecular dynamics, we will focus our attention on the energy landscape and paths relevant to B2, B19′ and B19 phases in our statistical mechanical analysis of the MT.

We follow here the scheme of the lattice Wannier functions (LWFs) in Ref. [22], and identify the symmetry invariant subspaces of the relevant degrees of freedom starting with full phonon dispersion of B2 structure obtained along the high-symmetry lines ($\Gamma \to X \to M \to \Gamma \to R \to M$, see Fig. 3.3a) in the BZ. Subspaces of acoustic and optical phonons are separated by a gap in frequencies and involve modes dominated by Ni and Ti displacements respectively. Using symmetries and

Table 3.2: Order parameters (M-point phonon modes at $\vec{q} = \frac{\pi}{a}(011)$ of the cubic B2 structure and strain tensor components) associated with various low-symmetry structures of NiTi, obtained from first-principles calculations. The amplitudes of phonon eigenmodes are in unit of lattice constant of B2 structure, and phonon eigenmodes are expressed in terms of atomic displacements $\hat{e}_{ph} = |Ti_x, Ti_y, Ti_z, Ni_x, Ni_y, Ni_z >$. The strain eigenmodes $s = |\varepsilon_1, \varepsilon_2, \varepsilon_3, \varepsilon_4, \varepsilon_5, \varepsilon_6 >$, are in the Voigt notation. ($\varepsilon_1 = \varepsilon_{xx}$, $\varepsilon_2 = \varepsilon_{yy}$, $\varepsilon_3 = \varepsilon_{zz}$, $\varepsilon_4 = 2\varepsilon_{yz}$, $\varepsilon_5 = 2\varepsilon_{zx}$ and $\varepsilon_6 = 2\varepsilon_{xy}$).

Modes	Eigenmode	Character	B2	B19	B19′
$M_{5'}$	$\|0, 0.33, 0.33, 0, 0.94, 0.94 >$	$\{0\bar{1}1\}$<011> Basal shuffle	0	0.075	-0.095
$M_{2'}$	$\|0, 0, 0, 1, 0, 0 >$	$\{0\bar{1}1\}$<100>, Ni displacements	0	0	0.066
$M_{4'}$	$\|1, 0, 0, 0, 0, 0 >$	$\{0\bar{1}1\}$<100>, Ti displacements	0	0	-0.096
s_1	$\frac{1}{\sqrt{2}}\|0, 1, -1, 0, 0, 0 >$	$\{0\bar{1}1\}$<011> Basal shear	0	0	0
s_2	$\frac{1}{\sqrt{6}}\|-2, 1, 1, 0, 0, 0 >$	Bain strain	0	0.072	0.047
s_3	$\frac{1}{\sqrt{3}}\|1, 1, 1, 0, 0, 0 >$	Hydrostatic strain	0	0.003	0.017
s_4	$\|0, 0, 0, 1, 0, 0 >$	{010}<001> Pure shear	0	0.099	0.162
s_5	$\frac{1}{\sqrt{2}}\|0, 0, 0, 0, 1, 1 >$	{100}<011> Non-basal shear	0	0	-0.199

eigenvectors of the zone boundary phonons, we determine Ni-centric $\{\vec{\eta}\}$ and Ti-centric $\{\vec{\tau}\}$ localized LWFs to span these subspaces of phonons.

Using the cubic symmetry (of B2 phase), we express H_{eff} as an explicit symmetry invariant Taylor expansion in $\vec{\eta}_i$, $\vec{\tau}_i$ and homogeneous strains ($\varepsilon_{\alpha\beta}$), i indicating the lattice unit cell to which $\vec{\eta}_i$ and $\vec{\tau}_i$ belong. H_{eff} consists of four parts:

$$H_{eff} = H_{eff}^{Ni}(\vec{\eta}_i) + H_{eff}^{Ti}(\vec{\tau}_i) + H_{spc}(\vec{\eta}_i, \vec{\tau}_i, \varepsilon_{\alpha\beta}) + H_{elastic}(\varepsilon_{\alpha\beta}), \tag{3.2}$$

where $H_{eff}^{Ni}(\vec{\eta}_i)$ and $H_{eff}^{Ti}(\vec{\tau}_i)$ operate in the subspaces of acoustic and optic phonons respectively. $H_{elastic}(\varepsilon_{\alpha\beta})$ is the linear and nonlinear elastic energy of homogeneous strain $\varepsilon_{\alpha\beta}$, and the coupling of $\varepsilon_{\alpha\beta}$ with both sets of LWFs is included in $H_{spc}(\vec{\eta}_i, \vec{\tau}_i, \varepsilon_{\alpha\beta})$. We note that inhomogeneous (spatially varying) strain field is captured here by the acoustic phonons: $\varepsilon_{\alpha\beta}(\underline{r}) = \frac{1}{2}(\frac{\partial \eta_\alpha}{\partial r_\beta} + \frac{\partial \eta_\beta}{\partial r_\alpha})$. Energetics of $\varepsilon_{\alpha\beta}(\underline{r})$ captured in H_{eff}^{Ni} has to be consistent with the energies of homogeneous strain $\varepsilon_{\alpha\beta}$

captured in $H_{elastic}$. This is achieved by ensuring the equivalence between $H_{elastic}$ and H_{eff}^{Ni}, H_{spc} in the long-wavelength limit.

3.5.1 Effective Hamiltonian of acoustic modes: H_{eff}^{Ni}

$H_{eff}^{Ni}(\vec{\eta}_i)$ represents energetics of acoustic phonons (and inhomogeneous strain), which include all the lattice instabilities in NiTi, i.e. unstable modes (Fig. 3.3a), This part of effective Hamiltonian is invariant under translational and rotational symmetries. It includes harmonic and anharmonic terms, which relate to linear and nonlinear elastic energy terms in $H_{elastic}$ in the long-wavelength (continuum) limit. To impose the translational symmetry, we express its terms using differences in $\vec{\eta}_i$'s at neighboring sites and their dot products. In the harmonic part, we consider differences between $\vec{\eta}_i$'s up to third NN sites, with a general form permitted by the symmetry of space group $Pm\bar{3}m$ as follows:

$$\begin{aligned} H_{har}(\vec{\eta}) &= \frac{1}{2}\sum_{i=1}^{N}[\sum_{j=1}^{6}\{A_{11}|\vec{\eta}_{1ij}|^2 + A_{12}(\vec{\eta}_{1ij}\cdot\hat{d}_{1j})^2\} \\ &+ \sum_{j=1}^{12}\{A_{21}(\vec{\eta}_{2ij}\cdot\hat{d}_{2j})^2 + A_{22}(\vec{\eta}_{2ij}\cdot\hat{d}_{21j})^2 + A_{23}(\vec{\eta}_{2ij}\cdot\hat{d}_{22j})^2\} \\ &+ \sum_{j=1}^{8}\{A_{31}|\vec{\eta}_{3ij}|^2 + A_{32}(\vec{\eta}_{3ij}\cdot\hat{d}_{3j})^2\}], \end{aligned} \tag{3.3}$$

where $\vec{\eta}_{1ij}$, $\vec{\eta}_{2ij}$, $\vec{\eta}_{3ij}$ denote the LWFs differences between $\vec{\eta}_i$ at site i and its $\vec{\eta}_j$ first, second and third NNs at site j respectively. $\hat{d}_{1j}$, $\hat{d}_{2j}$,$\hat{d}_{3j}$ denote unit vectors along the directions of first, second and third NN sites j respectively. $\hat{d}_{21j}$ and $\hat{d}_{22j}$ are unit vectors perpendicular to $\hat{d}_{2j}$. A_{ij}'s are the harmonic coefficients in H_{eff}^{Ni}, and determined from force constants of acoustic phonons at high symmetry q-points (M and R) and $\vec{q}_\Sigma = \frac{\pi}{3a}(0,1,1)$. Linear combinations of these coefficients give the corresponding eigenvalues of acoustic phonons. Since we have six equations

Table 3.3: Linear combinations of coefficients in the harmonic terms in H_{eff}^{Ni} at a q-point give the eigenvalue of corresponding phonon. $M_{2'}$ and $M_{5'}$ represent TA_2 and doubly degenerate unstable (LA and TA_1) modes at M-point, respectively. Σ_1, Σ_3 and Σ_4 represent LA , TA_1 and TA_2 modes at Σ-point respectively, and $R_{25'}$ represents triply degenerate acoustic mode at R-point.

Acoustic phonon	Linear combination of the coefficients	Eigenvalue of acoustic phonon (eV/f.u)
$M_{2'}$	$4A_{11} + 4A_{21} + 4A_{22}$	9.22
$M_{5'}$	$4A_{11} + 2A_{12} + 2A_{21} + 2A_{22} + 4A_{23}$	-4.19
Σ_1	$\frac{1}{2}A_{11} + \frac{1}{4}A_{12} + A_{21} + \frac{1}{4}A_{22} + \frac{1}{2}A_{23} + \frac{3}{2}A_{31} + A_{32}$	7.24
Σ_3	$\frac{1}{2}A_{11} + \frac{1}{4}A_{12} + \frac{1}{4}A_{21} + A_{22} + \frac{1}{2}A_{23} + \frac{3}{2}A_{31}$	0.80
Σ_4	$\frac{1}{2}A_{11} + \frac{1}{2}A_{21} + \frac{1}{2}A_{22} + \frac{3}{4}A_{23} + \frac{3}{2}A_{31} + \frac{1}{2}A_{32}$	1.95
$R_{25'}$	$6A_{11} + 2A_{12} + 8A_{31} + \frac{8}{3}A_{32}$	5.65

(Table 3.3) and seven coefficients, we use singular value decomposition (SVD) to determine these coefficients, and have listed them in Table 3.7.

In the anharmonic part of H_{eff}^{Ni}, we considered differences in $\vec{\eta}_i$'s up to third NN sites in the third-, and fourth-order terms, which are needed to include inhomogeneous strain correctly in the long-wavelength limit (interaction of the first and second NN sites is zero for shear strain in third-order terms (See Table 3.4), and hence we need the third NN sites interaction). Due to cubic symmetry, odd-order terms do not contribute to the energy of phonons at high-symmetry q-point, but do contribute in the long-wavelength limit. We approximated interaction in the third-order terms by considering the dominant term in interaction with NN sites allowed by the cubic symmetry. Fourth-order interaction terms include the full cubic anisotropy for the first NNs and isotropic terms for the second and third NNs. We simplified sixth- and eighth-order terms restricting to the isotropic ones in differences between $\vec{\eta}_i$'s up to first NNs. Since our nonlinear elastic energy includes terms up to fourth-order, we did not include fifth- and seventh-order terms in the anharmonic part of H_{eff}^{Ni}. Moreover, the MT in NiTi is primarily governed by unstable M-point phonons, which are not affected by the fifth- and seventh-order terms. We have tested that the errors associated with such truncation are less than 1% of the

energy differences.

$$
\begin{aligned}
H_{anh}(\vec{\eta}) &= \sum_{i=1}^{N}[B_{31}\sum_{j=1}^{6}(\vec{\eta}_{1ij}\cdot\hat{d}_{1j})^3 + B_{32}\sum_{j=1}^{12}(\vec{\eta}_{2ij}\cdot\hat{d}_{2j})^3 + B_{33}\sum_{j=1}^{8}(\vec{\eta}_{3ij}\cdot\hat{d}_{3j})^3 \\
&+ \sum_{j=1}^{6}\{B_{41}(\eta_{1ijx}^4+\eta_{1ijy}^4+\eta_{1ijz}^4) + B_{42}(\eta_{1ijx}^2\eta_{1ijy}^2+\eta_{1ijy}^2\eta_{1ijz}^2+\eta_{1ijz}^2\eta_{1ijx}^2) \\
&+ B_{43}(\vec{\eta}_{1ij}\cdot\hat{d}_{1j})^4 + B_{44}|\vec{\eta}_{1ij}|^2(\vec{\eta}_{1ij}\cdot\hat{d}_{1j})^2\} + B_{45}\sum_{j=1}^{12}|\vec{\eta}_{2ij}|^4 + B_{46}\sum_{j=1}^{8}|\vec{\eta}_{3ij}|^4 \\
&+ \sum_{j=1}^{6}\{B_{61}|\vec{\eta}_{1ij}|^6 + B_{81}|\vec{\eta}_{1ij}|^8\}], \qquad (3.4)
\end{aligned}
$$

where B_{ij}'s are coefficients of anharmonic terms. Third-order terms of H_{eff}^{Ni} coefficients are related to the nonlinear elastic moduli. Thus, these third-order coefficients (B_{31}, B_{32} and B_{33}) are obtained from the corresponding third-order elastic moduli. Since there are only three coefficients, we use three inequivalent strain modes (hydrostatic strain, Bain strain and shear strain) to calculate these coefficients (See Table 3.4). Fourth-order terms in H_{eff}^{Ni} contribute to energy of phonons at both high-symmetry q-points and long-wavelength limit. We have six fourth-order coefficients in the H_{eff}^{Ni}, which are calculated by freezing doubly degenerate unstable $M_{5'}$ (η_y and η_z), stable $M_{2'}$ (η_x) acoustic phonons and their linear combinations (Fig. 3.6). We fitted the total energy of configurations obtained as structural distortions with these phonon modes to a polynomial of 8^{th} order. We used two strain modes (hydrostatic and shear strain modes) to connect with behavior in the long wavelength limit (Table 3.5). To determine the coefficients of sixth- and eight-order terms in H_{eff}^{Ni}, ($128B_{61} = -3.7\times10^4$ eV/f.u) and ($512B_{81} = 8.3\times10^5$ eV/f.u), we fit the polynomial to double-well energy of $M_{5'}$ mode. We used gnuplot software for fitting these data to polynomials (values of all these coefficients are listed in Table 3.7), and find that the maximum fitting errors in second-, fourth-, sixth- and eight-order coefficients are $\pm0.13\%$, $\pm0.31\%$, $\pm1.58\%$ and $\pm3.85\%$ respectively.

These are negligible and do not affect the energy landscape and its impact on the MT.

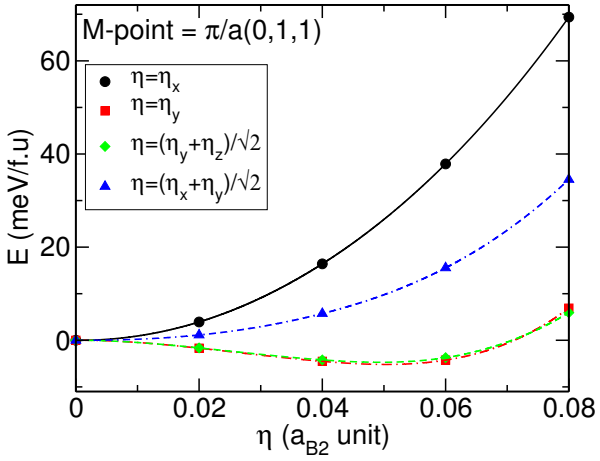

Figure 3.6: Total energies of cell-doubling structural distortions ($\vec{\eta}$ at $\vec{q} = \frac{\pi}{a}(0,1,1)$). Lines represent the fits obtained with the 4^{th}, 6^{th} and 8^{th} anharmonic parameters in H_{eff}.

,

Table 3.4: Strain mode is represented with $s = |\varepsilon_1, \varepsilon_2, \varepsilon_3, \varepsilon_4, \varepsilon_5, \varepsilon_6 >$, in the Voigt notation. Hydrostatic, Bain and shear strain modes are represented by $s_{hydro} = \varepsilon|1,1,1,0,0,0>$, $s_{Bain} = \varepsilon|-2,1,1,0,0,0>$ and $s_{shear} = \varepsilon|0,0,0,1,1,1>$ respectively. Coefficients of the 3^{rd} order terms in H_{eff}^{Ni} are linear combinations of the 3^{rd} order elastic moduli.

Strain mode	Linear combination of 3^{rd} order coefficients	Linear combination of 3^{rd} order elastic moduli
s_{hydro}	$6B_{31} + 33.94B_{32} + 41.57B_{33}$	$\frac{1}{2}C_{111} + 3C_{112} + C_{123}$
s_{Bain}	$-12B_{31} + 8.49B_{32}$	$-C_{111} + 3C_{112} - 2C_{123}$
s_{shear}	$9.24B_{33}$	C_{456}

3.5.2 Effective Hamiltonian of optical phonons: H_{eff}^{Ti}

$H_{eff}^{Ti}(\vec{\tau}_i)$ models the energetics of optical phonons which are all stable ($\omega^2 > 0$). Hence, we include only harmonic interactions between $\vec{\tau}_i$'s up to third nearest neighbor sites with a general form permitted by the symmetry of $Pm\bar{3}m$ space group [23]:

Table 3.5: The amplitudes of phonon eigenmodes are in unit of lattice constant of B2 structure, and phonon eigenmodes are expressed in terms of atomic displacements $\hat{e}_{ph} = |Ti_x, Ti_y, Ti_z, Ni_x, Ni_y, Ni_z >$. The eigenmodes at M-point ($\frac{\pi}{a}(011)$) are $\eta_x = |0, 0, 0, 1, 0, 0 >$ of $M_{2'}$ phonon, $\eta_y = |0, 0, 0.33, 0, 0.94, 0 >$ and $\eta_z = |0, 0.33, 0, 0, 0, 0.94 >$ of doubly degenerate $M_{5'}$ mode. s_{hydro} and s_{shear} are two strain modes.

Mode	Linear combination of 4^{th} order coefficients	4^{th} order fitting coefficients in in polynomial (eV/f.u)
η_x	$32B_{41} + 64B_{45}$	468.68
η_y	$32B_{41} + 16B_{43} + 16B_{44} + 64B_{45}$	1057.35
$\frac{1}{\sqrt{2}}(\eta_y + \eta_z)$	$16B_{41} + 8B_{42} + 8B_{43} + 16B_{44} + 64B_{45}$	999.11
$\frac{1}{\sqrt{2}}(\eta_x + \eta_y)$	$16B_{41} + 8B_{42} + 4B_{43} + 8B_{44} + 64B_{45}$	637.52
s_{hydro}	$6B_{41} + 6B_{43} + 6B_{44} + 192B_{45} + 648B_{46}$	$\frac{1}{8}C_{1111} + C_{1112} + \frac{3}{4}C_{1122} + \frac{3}{2}C_{1123}$=815.68
s_{shear}	$0.75B_{41} + 0.375B_{42} + 30.75B_{45} + 168B_{46}$	$\frac{1}{8}C_{4444} + \frac{3}{4}C_{4455}$=112.34

$$
\begin{aligned}
H_{eff}^{Ti}(\vec{\tau}) &= \frac{1}{2}\sum_{i=1}^{N}[\tilde{A}_{01}|\vec{\tau}_i|^2 + \sum_{j=1}^{6}\{\tilde{A}_{11}|\vec{\tau}_{1ij}|^2 + \tilde{A}_{12}(\vec{\tau}_{1ij}\cdot\hat{d}_{1j})^2\} \\
&+ \sum_{j=1}^{12}\{\tilde{A}_{21}|\vec{\tau}_{2ij}|^2 + \tilde{A}_{22}(\vec{\tau}_{2ij}\cdot\hat{d}_{2j})^2\} + \sum_{j=1}^{8}\tilde{A}_{31}|\vec{\tau}_{3ij}|^2], \qquad (3.5)
\end{aligned}
$$

where $\vec{\tau}_i$ denotes Ti-centric LWFs at site i, $\vec{\tau}_{1ij}$, $\vec{\tau}_{2ij}$, $\vec{\tau}_{3ij}$ denote the LWFs differences between $\vec{\tau}_i$ and $\vec{\tau}_j$ at its first, second and third NN sites j respectively. $\tilde{A}_{ij}$'s are the coefficients of harmonic interactions in $H_{eff}^{Ti}(\vec{\tau})$. To determine the coefficients of terms in $H_{eff}^{Ti}(\vec{\tau}_i)$, we use force constants of optical phonons at high symmetric q-points (Γ, X, M and R). The linear combinations of the harmonic coefficients in H_{eff}^{Ti} subspace give the eigenvalues of optical phonons (See Table 3.6) at the respective q-points. The values of these coefficients are listed in Table 3.7.

Table 3.6: Linear combinations of coefficients in the harmonic terms in H_{eff}^{Ti} at a q-point give to the corresponding eigenvalues of optical phonons.

q-point	Linear combination of the coefficients	Eigenvalue of optical phonon (eV/f.u)
Γ_{15}	$\frac{1}{2}\tilde{A}_{01}$	37.77
$X_{4'}$	$\frac{1}{2}\tilde{A}_{01} + 2\tilde{A}_{11} + 2\tilde{A}_{12} + 8\tilde{A}_{21} + 4\tilde{A}_{22} + 8\tilde{A}_{23}$	65.32
$X_{5'}$	$\frac{1}{2}\tilde{A}_{01} + 2\tilde{A}_{11} + 8\tilde{A}_{21} + 2\tilde{A}_{22} + 8\tilde{A}_{23}$	20.30
$M_{4'}$	$\frac{1}{2}\tilde{A}_{01} + 4\tilde{A}_{11} + 8\tilde{A}_{21} + 4\tilde{A}_{22}$	17.18
$M_{5'}$	$\frac{1}{2}\tilde{A}_{01} + 4\tilde{A}_{11} + 2\tilde{A}_{12} + 8\tilde{A}_{21} + 2\tilde{A}_{22}$	55.52
R_{15}	$\frac{1}{2}\tilde{A}_{01} + 6\tilde{A}_{11} + 2\tilde{A}_{12} + 8\tilde{A}_{23}$	49.95

Table 3.7: Coefficients of harmonic and anharmonic terms in effective Hamiltonian in unit of eV/f.u..

Coeff.	Values	Coeff.	Values	Coeff.	Values
A_{11}	-2.6	$\tilde{A}_{11}$	-4.5	B_{41}	11.3
A_{12}	3.3	$\tilde{A}_{12}$	20.8	B_{42}	-1.6
A_{21}	4.6	$\tilde{A}_{21}$	-1.2	B_{43}	-16.9
A_{22}	0.3	$\tilde{A}_{22}$	1.7	B_{44}	53.7
A_{23}	-2.6	$\tilde{A}_{31}$	-0.3	B_{45}	1.7
A_{31}	0.8	B_{31}	0.8	B_{46}	0.3
A_{32}	3.2	B_{32}	-6.9	B_{61}	-286.1
$\tilde{A}_{01}$	75.6	B_{33}	-3.7	B_{81}	1614.3

3.5.3 Hamiltonian of homogeneous strain: linear and non-linear elastic energy

Large deformations (homogeneous strain) are involved during MT in NiTi as a result of its soft second-order elastic moduli. We considered non-linear elasticity ($H_{elastic}(\varepsilon_{\alpha\beta})$) with terms upto fourth order allowed by the cubic symmetry [91–96]. Using the Voigt notation ($\varepsilon_1 = \varepsilon_{xx}$, $\varepsilon_2 = \varepsilon_{yy}$, $\varepsilon_3 = \varepsilon_{zz}$, $\varepsilon_4 = 2\varepsilon_{yz}$, $\varepsilon_5 = 2\varepsilon_{zx}$ and $\varepsilon_6 = 2\varepsilon_{xy}$), elastic energy is expressed as:

$$
\begin{aligned}
H_{elastic}(\varepsilon) &= NC_1(\varepsilon_1+\varepsilon_2+\varepsilon_3) \\
&+ \frac{N}{2}\{C_{11}(\varepsilon_1^2+\varepsilon_2^2+\varepsilon_3^2)+2C_{12}(\varepsilon_1\varepsilon_2+\varepsilon_2\varepsilon_3+\varepsilon_3\varepsilon_1)+C_{44}(\varepsilon_4^2+\varepsilon_5^2+\varepsilon_6^2)\} \\
&+ \frac{N}{6}\{C_{111}(\varepsilon_1^3+\varepsilon_2^3+\varepsilon_3^3)+3C_{112}(\varepsilon_1^2(\varepsilon_2+\varepsilon_3)+\varepsilon_2^2(\varepsilon_3+\varepsilon_1)+\varepsilon_3^2(\varepsilon_1+\varepsilon_2)) \\
&+ 6C_{123}\varepsilon_1\varepsilon_2\varepsilon_3+3C_{144}(\varepsilon_1\varepsilon_4^2+\varepsilon_2\varepsilon_5^2+\varepsilon_3\varepsilon_6^2) \\
&+ 3C_{155}(\varepsilon_1(\varepsilon_5^2+\varepsilon_6^2)+\varepsilon_2(\varepsilon_6^2+\varepsilon_4^2)+\varepsilon_3(\varepsilon_4^2+\varepsilon_5^2))+6C_{456}\varepsilon_4\varepsilon_5\varepsilon_6\} \\
&+ \frac{N}{24}\{C_{1111}(\varepsilon_1^4+\varepsilon_2^4+\varepsilon_3^4)+4C_{1112}(\varepsilon_1^3(\varepsilon_2+\varepsilon_3)+\varepsilon_2^3(\varepsilon_3+\varepsilon_1)+\varepsilon_3^3(\varepsilon_1+\varepsilon_2)) \\
&+ 6C_{1122}(\varepsilon_1^2\varepsilon_2^2+\varepsilon_2^2\varepsilon_3^2+\varepsilon_3^2\varepsilon_1^2)+12C_{1123}\varepsilon_1\varepsilon_2\varepsilon_3(\varepsilon_1+\varepsilon_2+\varepsilon_3) \\
&+ 6C_{1144}(\varepsilon_1^2\varepsilon_4^2+\varepsilon_2^2\varepsilon_5^2+\varepsilon_3^2\varepsilon_6^2)+6C_{1155}(\varepsilon_1^2(\varepsilon_5^2+\varepsilon_6^2)+\varepsilon_2^2(\varepsilon_6^2+\varepsilon_4^2)+\varepsilon_3^2(\varepsilon_4^2+\varepsilon_5^2)) \\
&+ 12C_{1255}(\varepsilon_1\varepsilon_2(\varepsilon_4^2+\varepsilon_5^2)+\varepsilon_2\varepsilon_3(\varepsilon_5^2+\varepsilon_6^2)+\varepsilon_3\varepsilon_1(\varepsilon_6^2+\varepsilon_4^2)) \\
&+ 12C_{1266}(\varepsilon_1\varepsilon_2\varepsilon_6^2+\varepsilon_2\varepsilon_3\varepsilon_4^2+\varepsilon_3\varepsilon_1\varepsilon_5^2)+24C_{1456}\varepsilon_4\varepsilon_5\varepsilon_6(\varepsilon_1+\varepsilon_2+\varepsilon_3) \\
&+ C_{4444}(\varepsilon_4^4+\varepsilon_5^4+\varepsilon_6^4)+6C_{4455}(\varepsilon_4^2\varepsilon_5^2+\varepsilon_5^2\varepsilon_6^2+\varepsilon_6^2\varepsilon_4^2)\}, \qquad (3.6)
\end{aligned}
$$

where N is the number of unit cells, C_{ij}, C_{ijk} and C_{ijkl} are second-, third- and fourth-order elastic moduli, C_1 represents a pressure term. To calculate elastic moduli, we fit the total energy of structures distorted along different strain modes to fourth-order polynomial in ε. The linear combinations of second-, third- and fourth-order elastic moduli give second-, third- and fourth-order coefficient of the polynomial respectively (See Table 3.8), fit to energy of each strain mode using gnuplot software. We find the maximum fitting errors in first-, second-, third- and fourth-order coefficients to be $\pm 0.14\%$, $\pm 0.10\%$, $\pm 5.05\%$ and $\pm 5.10\%$ respectively, which are negligible. Our estimates of these compliances are listed in Table 3.9. While third- and fourth-order elastic moduli of NiTi have not been determined theoretically and experimentally to the best of our knowledge, our estimates of the linear elastic moduli are in good agreement with earlier theoretical [60, 97] and experimental works [98] (Table 3.10).

Table 3.8: In each type of strain modes $s_\alpha(\varepsilon) = |\varepsilon_1, \varepsilon_2, \varepsilon_3, \varepsilon_4, \varepsilon_5, \varepsilon_6 >$, the total energy is expressed as a polynomial function of ε. The linear combinations of second, third and forth order elastic moduli are equal to the values of second-, third- and forth- order coefficients of polynomial fit to the data.

Strain mode	Linear combination of C_{ij}	Linear combination of C_{ijk}	Linear combination of C_{ijkl}
$s_a = \varepsilon\|1,0,0,0,0,0>$	$\frac{1}{2}C_{11}$	$\frac{1}{6}C_{111}$	$\frac{1}{24}C_{1111}$
$s_b = \varepsilon\|1,1,0,0,0,0>$	$C_{11}+C_{12}$	$\frac{1}{3}C_{111}+C_{112}$	$\frac{1}{16}C_{1111}+\frac{1}{3}C_{1112}+\frac{1}{4}C_{1122}$
$s_c = \varepsilon\|1,-1,0,0,0,0>$	$C_{11}-C_{12}$	0	$\frac{1}{16}C_{1111}-\frac{1}{3}C_{1112}+\frac{1}{4}C_{1122}$
$s_d = \varepsilon\|1,1,1,0,0,0>$	$\frac{3}{2}C_{11}+3C_{12}$	$\frac{1}{2}C_{111}+3C_{112}+C_{123}$	$\frac{1}{8}C_{1111}+C_{1112}+\frac{1}{4}C_{1122}+\frac{3}{2}C_{1123}$
$s_e = \varepsilon\|0,0,0,1,0,0>$	$\frac{1}{2}C_{44}$	0	$\frac{1}{24}C_{4444}$
$s_f = \varepsilon\|0,0,0,1,1,1>$	$\frac{3}{2}C_{44}$	C_{456}	$\frac{1}{8}C_{4444}+\frac{3}{4}C_{4444}$
$s_g = \varepsilon\|1,0,0,1,0,0>$	$\frac{1}{2}C_{11}+\frac{1}{2}C_{44}$	$\frac{1}{6}C_{111}+\frac{1}{2}C_{144}$	$\frac{1}{24}C_{1111}+\frac{1}{4}C_{1144}+\frac{1}{24}C_{4444}$
$s_h = \varepsilon\|1,0,0,0,0,1>$	$\frac{1}{2}C_{11}+\frac{1}{2}C_{44}$	$\frac{1}{6}C_{111}+\frac{1}{2}C_{155}$	$\frac{1}{24}C_{1111}+\frac{1}{4}C_{1155}+\frac{1}{24}C_{4444}$
$s_i = \varepsilon\|1,1,0,1,0,0>$	$C_{11}+C_{12}+\frac{1}{2}C_{44}$	$\frac{1}{3}C_{111}+C_{112}+\frac{1}{2}C_{144}$ $+\frac{1}{2}C_{155}$	$\frac{1}{16}C_{1111}+\frac{1}{3}C_{1112}+\frac{1}{4}C_{1122}+\frac{1}{4}C_{1144}$ $+\frac{1}{4}C_{1155}+\frac{1}{2}C_{1255}+\frac{1}{24}C_{4444}$
$s_j = \varepsilon\|1,1,0,0,0,1>$	$C_{11}+C_{12}+\frac{1}{2}C_{44}$	$\frac{1}{3}C_{111}+C_{112}+\frac{1}{2}C_{155}$	$\frac{1}{16}C_{1111}+\frac{1}{3}C_{1112}+\frac{1}{4}C_{1122}$ $+\frac{1}{2}C_{1155}+\frac{1}{2}C_{1266}+\frac{1}{24}C_{4444}$
$s_k = \varepsilon\|1,0,0,1,1,1>$	$\frac{1}{2}C_{11}+\frac{3}{2}C_{44}$	$\frac{1}{3}C_{111}+C_{112}+\frac{1}{2}C_{144}$ $+C_{155}+C_{456}$	$\frac{1}{24}C_{1111}+\frac{1}{4}C_{1144}+\frac{1}{2}C_{1155}$ $+C_{1456}+\frac{1}{8}C_{4444}+\frac{3}{4}C_{4455}$

Table 3.9: Elastic moludi of $H_{elastic}(\varepsilon)$ in GPa, determined from first-principles.

Coeff.	Values	Coeff.	Values	Coeff.	Values
C_1	-1	C_{144}	-205	C_{1144}	2081
C_{11}	174	C_{155}	-201	C_{1155}	1700
C_{12}	155	C_{456}	-201	C_{1255}	2174
C_{44}	48	C_{1111}	15515	C_{1266}	458
C_{111}	-464	C_{1112}	-1806	C_{1456}	617
C_{112}	-544	C_{1122}	4732	C_{4444}	2145
C_{123}	-386	C_{1123}	760	C_{4455}	528

3.5.4 Coupling of homogeneous strain with phonons

Homogeneous strain and its coupling with LWFs ($\vec{\eta}$'s and $\vec{\tau}$'s) play a crucial role in MT. In $H_{spc}(\vec{\eta}_i, \vec{\tau}_i, \varepsilon_{\alpha\beta})$, we include couplings between homogeneous strains and (i) quadratic terms in $\vec{\eta}_i$'s (differences between $\vec{\eta}_i$ at site i and $\vec{\eta}_j$ at its first NN sites

Table 3.10: Second-order elastic moduli of B2 structure of NiTi in unit of GPa.

Method	C_{11}	C_{12}	$C' = \frac{1}{2}(C_{11} - C_{12})$	C_{44}
Present	174	154	10	48
Ref. [60]	183	146	19	46
Ref. [97]	168	144	12	50
Exp [98]	162	129	16.5	34

j, see Eq. (3.7)), and (ii) with products of Ti and Ni-centric LWFs (See Eq. 3.8). The former captures the coupling between primary order parameter, $M_{5'}$ mode and strain, while the latter gives mixing between acoustic and optical phonons due to strain distortions. We find that the third-order strain-phonon coupling terms are not sufficient to capture the details of low energy phases, and hence include fourth-order coupling between axial strain and Ni-centric LWFs (See Eq. 3.9).

$$
\begin{aligned}
H^3_{spc}(\vec{\eta},\varepsilon) &= \sum_{i=1}^{N}\sum_{j=1}^{6}\{g_{31}(\varepsilon_1+\varepsilon_2+\varepsilon_3)|\vec{\eta}_{1ij}|^2 \\
&+ g_{32}(\varepsilon_1\eta^2_{1ijx}+\varepsilon_2\eta^2_{1ijy}+\varepsilon_3\eta^2_{1ijz}) \\
&+ g_{33}(\varepsilon_1+\varepsilon_2+\varepsilon_3)(\vec{\eta}_{1ij}\cdot\hat{d}_{1j})^2 \\
&+ g_{34}(\varepsilon_1\eta^2_{1ijx}d^2_{1jx}+\varepsilon_2\eta^2_{1ijy}d^2_{1jy}+\varepsilon_3\eta^2_{1ijz}d^2_{1jz}) \\
&+ g_{35}(\varepsilon_1(\eta^2_{1ijy}+\eta^2_{1ijz})d^2_{1jx}+\varepsilon_2(\eta^2_{1ijz}+\eta^2_{1ijx})d^2_{1jy}+\varepsilon_3(\eta^2_{1ijx}+\eta^2_{1ijy})d^2_{1jz}) \\
&+ g_{36}(\varepsilon_4\eta_{1ijy}\eta_{1ijz}+\varepsilon_5\eta_{1ijz}\eta_{1ijx}+\varepsilon_6\eta_{1ijx}\eta_{1ijy}) \\
&+ g_{37}(\varepsilon_4\eta_{1ijy}\eta_{1ijz}d^2_{1jx}+\varepsilon_5\eta_{1ijz}\eta_{1ijx}d^2_{1jy}+\varepsilon_6\eta_{1ijx}\eta_{1ijy}d^2_{1jz})\}, \qquad (3.7)
\end{aligned}
$$

$$
\begin{aligned}
H^3_{spc}(\vec{\eta},\vec{\tau},\varepsilon) &= \sum_{i=1}^{N}[h_{31}(\varepsilon_1+\varepsilon_2+\varepsilon_3)\{\eta_{ix}\sum_{j=1}^{8}(\tau_{jy}d_{jy}+\tau_{jz}d_{jz})d_{jx}+c.p\} \\
&+ h_{32}\{\varepsilon_1\eta_{ix}\sum_{j=1}^{8}(\tau_{jy}d_{jy}+\tau_{jz}d_{jz})d_{jx}+c.p\} \\
&+ h_{33}\{\eta_{ix}\sum_{j=1}^{8}(\varepsilon_2\tau_{jy}d_{jy}+\varepsilon_3\tau_{jz}d_{jz})d_{jx}+c.p\} \\
&+ h_{34}\{\varepsilon_4\eta_{ix}\sum_{j=1}^{8}\tau_{jx}d_{jy}d_{jz}+c.p\} \\
&+ h_{35}\{\varepsilon_4\sum_{j=1}^{8}(\eta_{iy}\tau_{jy}+\eta_{iz}\tau_{jz})d_{jy}d_{jz}+c.p\} \\
&+ h_{36}\{\varepsilon_4\eta_{ix}\sum_{j=1}^{8}(\tau_{jy}d_{jz}+\tau_{jz}d_{jy})d_{jx}+c.p\} \\
&+ h_{37}\{\eta_{ix}\sum_{j=1}^{8}(\varepsilon_5\tau_{jy}+\varepsilon_6\tau_{jz})d_{jy}d_{jz}+c.p\}], \qquad (3.8)
\end{aligned}
$$

$$
\begin{aligned}
H^4_{spc}(\vec{\eta},\varepsilon) &= \sum_{i=1}^{N}\sum_{j=1}^{6}\{g_{41}(\varepsilon_1^2+\varepsilon_2^2+\varepsilon_3^2)|\vec{\eta}_{1ij}|^2 \\
&+ g_{42}(\varepsilon_1^2\eta_{1ijx}^2+\varepsilon_2^2\eta_{1ijy}^2+\varepsilon_3^2\eta_{1ijz}^2) \\
&+ g_{43}(\varepsilon_1(\varepsilon_2+\varepsilon_3)\eta_{1ijx}^2+\varepsilon_2(\varepsilon_3+\varepsilon_1)\eta_{1ijy}^2+\varepsilon_3(\varepsilon_1+\varepsilon_2)\eta_{1ijz}^2) \\
&+ g_{44}(\varepsilon_1\varepsilon_2\eta_{1ijz}^2+\varepsilon_2\varepsilon_3\eta_{1ijx}^2+\varepsilon_3\varepsilon_1\eta_{1ijy}^2), \qquad (3.9)
\end{aligned}
$$

where g_{ij}'s denote couplings of strain with Ni-centric LWFs, and h_{ij}'s are the third-order coupling that cause strain-induced mixing between acoustic and optic phonons. These coefficients were determined from calculations of structures obtained by freezing M-point phonon eigenvectors at the different values of strain. Values of the third- and fourth-order coupling coefficients (See Table 3.12) are obtained as first and second derivatives of harmonic coefficients with respect to strain respectively (See Table 3.11).

Table 3.11: At each type of strain modes $s_\alpha(\varepsilon) = |\varepsilon_1, \varepsilon_2, \varepsilon_3, \varepsilon_4, \varepsilon_5, \varepsilon_6 >$, value of third- and fourth-order strain-phonon coupling coefficients are obtained as first and second derivatives of harmonic force constants at different M-point phonon modes. $\eta_x = |0,0,0,1,0,0 >$ and $\tau_x = |1,0,0,0,0,0 >$ span the subspace of $M_{2'}$ and $M_{4'}$ phonons respectively, η_y and η_z span the subspace of doubly degenerate unstable acoustic phonon, while $\tau_y = |0,-0.94,0,0,0,0.33 >$ and $\tau_z = |0,0,-0.94,0,0.33,0,0 >$ span the subspace of doubly degenerate most stable optical phonon at M-point $(\frac{\pi}{a}(011)$.

Strain mode	Phonon mode	Linear combination of the coefficients	1^{st} derivative of eigenvalue (eV/f.u)
$s_a = \varepsilon\|1,0,0,0,0,0 >$	η_x	$8g_{31} + 8g_{32}$	-85.78
$s_a = \varepsilon\|1,0,0,0,0,0 >$	η_y	$8g_{31} + 4g_{33}$	58.21
$s_b = \varepsilon\|0,1,0,0,0,0 >$	η_y	$8g_{31} + 8g_{32} + 4g_{33} + 4g_{44}$	-107.87
$s_c = \varepsilon\|0,1,1,0,0,0 >$	η_x	$16g_{31} + 8g_{35}$	-134.16
$s_c = \varepsilon\|0,1,1,0,0,0 >$	η_y	$16g_{31} + 8g_{32} + 8g_{33} + 4g_{34} + 4g_{35}$	-94.31
$s_d = \varepsilon\|0,0,0,1,0,0 >$	$\frac{1}{\sqrt{2}}(\eta_y + \eta_z)$	$4g_{36}$	-71.83
$s_e = \varepsilon\|0,0,0,0,0,1 >$	$\frac{1}{\sqrt{2}}(\eta_x + \eta_y)$	$4g_{36} + 2g_{37}$	-31.57
$s_a = \varepsilon\|1,0,0,0,0,0 >$	$\frac{1}{2}(\eta_y + \eta_z + \tau_y + \tau_z)$	$4g_{31} + 2g_{33} + \frac{4}{3}h_{31}$	-1.05
$s_b = \varepsilon\|0,1,0,0,0,0 >$	$\frac{1}{\sqrt{2}}(\eta_y + \tau_z)$	$4g_{31} + 4g_{32} + 2g_{33} + 2g_{34}$ $+\frac{4}{3}h_{31} + \frac{4}{3}h_{32}$	-39.03
$s_f = \varepsilon\|0,1,1,0,0,0 >$	$\frac{1}{2}(\eta_y + \eta_z + \tau_y + \tau_z)$	$8g_{31} + 4g_{32} + 4g_{33} + 2g_{34}$ $+2g_{35} + \frac{8}{3}h_{31} + \frac{4}{3}h_{32} + \frac{4}{3}h_{33}$	1.98
$s_d = \varepsilon\|0,0,0,1,0,0 >$	$\frac{1}{\sqrt{2}}(\eta_x + \tau_x)$	$\frac{4}{3}h_{34}$	14.00
$s_d = \varepsilon\|0,0,0,1,0,0 >$	$\frac{1}{\sqrt{2}}(\eta_y + \tau_y)$	$\frac{4}{3}h_{35}$	-11.22
$s_g = \varepsilon\|0,0,0,0,1,0 >$	$\frac{1}{\sqrt{2}}(\eta_y + \tau_x)$	$\frac{4}{3}h_{36}$	34.34
$s_g = \varepsilon\|0,0,0,0,1,0 >$	$\frac{1}{\sqrt{2}}(\eta_x + \tau_y)$	$\frac{4}{3}h_{37}$	-21.86
Strain mode	Phonon mode	Linear combination of the coefficients	2^{nd} derivative of eigenvalue (eV/f.u)
$s_a = \varepsilon\|1,0,0,0,0,0 >$	η_y	$8g_{41}$	117.52
$s_b = \varepsilon\|0,1,0,0,0,0 >$	η_y	$8g_{41} + 8g_{42}$	1.16×10^3
$s_h = \varepsilon\|1,0,1,0,0,0 >$	η_y	$16g_{41} + 8g_{43}$	-9.11
$s_i = \varepsilon\|1,1,1,0,0,0 >$	η_y	$24g_{41} + 8g_{42} + 8g_{43} + 16g_{44}$	985.18

Table 3.12: Coefficients of strain-phonon couplings part of effective Hamiltonian in unit of eV/f.u..

Coeff.	Values	Coeff.	Values	Coeff.	Values
g_{31}	-2.8	g_{37}	20.1	h_{32}	33.8
g_{32}	-7.9	g_{41}	14.7	h_{33}	48.3
g_{33}	20.2	g_{42}	130.5	h_{34}	10.5
g_{34}	-25.7	g_{43}	-30.5	h_{35}	-8.4
g_{35}	-11.2	g_{44}	-10.4	h_{36}	25.8
g_{36}	-18.0	h_{31}	-22.6	h_{37}	-16.4

While our H_{eff} does not capture the details of BCO structure well, it reproduces the lattice parameters and energies of B2, B19 and B19′ structures with negligible errors relative to the DFT results (Table 3.13).

Table 3.13: Structural parameters (4 atoms per unit cell) and energies of B2, B19 and B19′ phases relative to B19′, obtained using DFT and H_{eff}.

Phase	Method	a($\mathring{A}$)	b($\mathring{A}$)	c($\mathring{A}$)	γ^o	$E - E_{B19'}$(meV/f.u)
B2	DFT	3.004	4.248	4.248	90	75.34
	H_{eff}	3.004	4.248	4.248	90	82.48
B19	DFT	2.832	4.589	4.168	90	28.34
	H_{eff}	2.812	4.713	4.101	90	35.00
B19′	FT	2.935	4.733	4.027	100.9	0.0
	H_{eff}	2.947	4.873	3.935	103.6	0.0

3.6 Monte Carlo simulations

We now analyze H_{eff} with Monte Carlo (MC) simulations on a periodic system containing $L \times L \times L$ (L = 16) unit cells of B2 structure. We used a single-flip update within Metropolis scheme and adjusted the step-size of configurational $\{\vec{\eta}_i$, $\vec{\tau}_i\}$ updates to maintain the acceptance ratio of ~ 0.5 near the transformation temperature. In each Monte Carlo sweep (MCS), we picked η_i, τ_i randomly (totally $2L^3$ updates) and homogeneous strain variables L times. Thus, each MCS involves $(2L^3 + L)$ attempts of updating configurations.

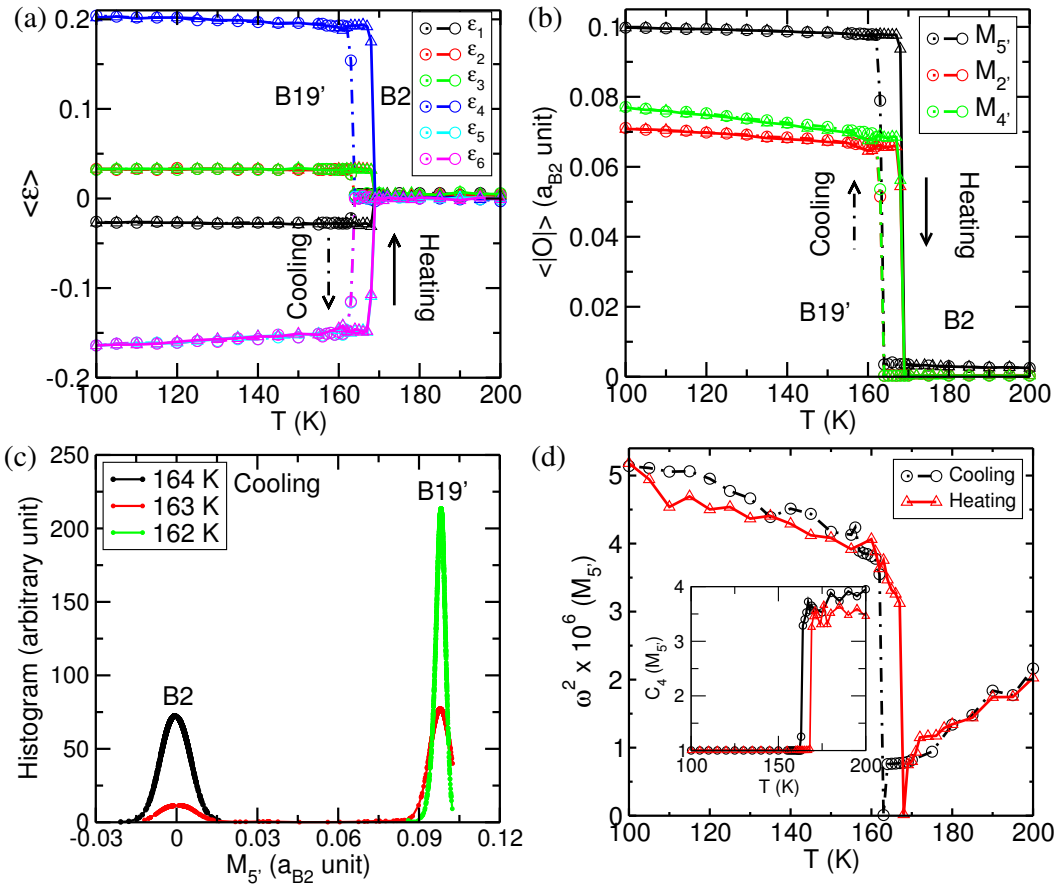

Figure 3.7: Averages of components of strain tensor (a), absolute values of $M_{5'}$, $M_{2'}$ and $M_{4'}$ modes (b) as a function of temperature at ambient pressure. Histograms of $M_{5'}$ mode obtained from configurations sampled during cooling (c) at T_M and its two temperatures in its close vicinity. Square of frequency of $M_{5'}$ phonon and its Binder cumulant (d).

To identify different phases from the configurations sampled in MC simulations at a given temperature, we accumulated absolute values of Fourier components of η_i and τ_i, and obtained averages of ($M_{5'}$, $M_{2'}$ and $M_{4'}$ modes), and averages of strain ($<\varepsilon>$) components at each temperature. To assess the possibility of hysteresis, we approach the transformation from high (low)-temperatures by cooling (heating) the system. In cooling simulations, we start from 200 K temperature, equilibrate the system to the cubic phase, and reduce the temperature in steps of 5 K (and 1 K near the transformation temperature), down to a low-temperature of 100 K. In heating

simulations, we start from T=100 K taking B19′ structure as the initial configuration and increase temperature in steps of 5 K (and 1 K near the transformation temperature) to a high-temperature of 200 K (we checked that our results do not depend on the choice of initial configuration). At each temperature, we used 10000 MCS for thermal equilibration and 50000 MCS for thermodynamic averaging.

Average values of homogeneous strain components ε (Fig. 3.7a), $M_{5'}$, $M_{2'}$ and $M_{4'}$ modes (Fig. 3.7b) vanish at high-temperatures, and change discontinuously to non-zero values at low-temperatures. In cooling simulations, this discontinuity marks the martensitic transformation at $T_M = 163$ K. In heating simulations, our model transforms to austenite phase at $T_A = 169$ K. It is clear (Fig. 3.7a and 3.7b) that NiTi transforms from B2 to B19′ structure directly ruling out the intermediate B19 structure. Results of our MC simulations reveal a sharp discontinuity in order parameters at T_M. Even more remarkable is that they change only weakly below T_M. Histograms of the primary order parameter obtained from cooling (Fig. 3.7c) simulations reveal (i) relatively narrow distributions and (ii) a sharp jump across T_M. Bimodal nature of the histogram at T_M confirms coexistence of B2 and B19′, and the first-order character of the MT. In order to further corroborate these results, we present frequency (ω) and Binder fourth order cumulant (C_4) of the primary order parameter (M_5' mode) obtained in both cooling and heating simulations:

$$\omega^2 \propto \frac{k_B T}{N}(\langle O^2\rangle - \langle O\rangle^2)^{-1}, \tag{3.10}$$

$$C_4 = \frac{\langle O^4\rangle}{\langle O^2\rangle^2}, \tag{3.11}$$

where $N = L^3$ is the number of unit cells used in simulations and O is $\vec{q} = \frac{\pi}{a}(011)$ Fourier component of η_y. Softening in $M_{5'}$ phonon frequency and its T-coefficients

(Fig. 3.7d) below and above T_M, and a discontinuity in C_4 (inset, Fig. 3.7d) of M_5' mode at T = 163 (169) K in cooling (heating) confirm that $M_{5'}$ mode is the primary order parameter of MT in NiTi. Our estimate of the equilibrium transition temperature ($T_0 = \frac{1}{2}(T_M + T_A)$) [99] is underestimated with respect to experiment (T_M = 318 K, T_A = 320 K and T_0 = 319) [77]. This is similar to the efficacy of model Hamiltonian schemes in prediction of ferroelectrics structural transitions [23]. This is probably because of the GGA-DFT errors in energies and structural parameters, and needs further investigation.

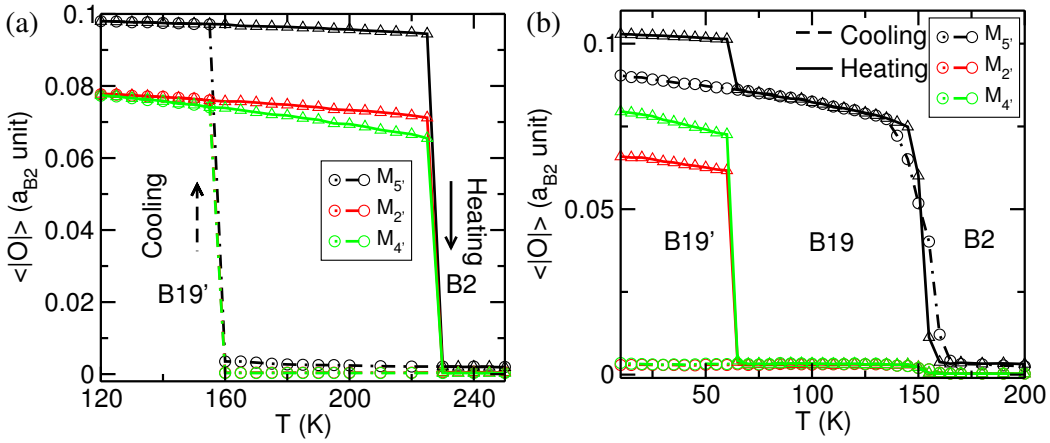

Figure 3.8: Average of absolute values of $M_{5'}$, $M_{2'}$ and $M_{4'}$ modes as a function of temperature at P = -5 GPa (a) and at P = 5 GPa (b).

To assess the sensitivity of our estimates of T_0 to DFT-errors in lattice constants, we simulated H_{eff} of NiTi at -5 GPa and 5 GPa pressures. At P =-5 GPa, transformation from B2 to B19′ structure (Fig. 3.8a) occurs at a notably higher temperature with hysteresis over a much wider range of temperature: $T_M \sim$ 155 K, $T_A \sim$ 225 K and T_0 = 190 K. At P = 5 GPa, in heating (we start from T=10 K taking B19′ structure as the initial configuration) simulations, the MT occurs in two steps (i) B19′ → B19 at 60 K, and (ii) B19 → B2 at 155 K (Fig. 3.8b), with a weaker hysteresis over ΔT = 5 K range. While in cooling simulations, B2 structure transforms into B19 structure at 155 K, and remains in this phase up on further cooling down

to 10 K (B19 structure does not transform into B19′ structure). This is probably because at P = 5 GPa, the energy difference between B19 and B19′ structure is small (Table 3.14) and the energy barrier is higher, needing longer simulation for a transition to occur. Thus, B19 phase can arise as a intermediate phase due to inhomogeneous pressure and stress fields in NiTi near the transformation temperature. Secondly, T_0 as well as the range of temperature of hysteresis in MT increase with negative pressure (i.e. increase in volume of the unit cell of B2 structure). We compared our pressure-induced martensitic transformation with the earlier experimental work [100], which has been done on Ni-rich (50.375 at.% Ni) composition of NiTi. Figure 6 of Ref. [100] shows that T_M increases with increasing uniaxial stress, which is unlikely in our work probably because we have applied hydrostatic pressure on equiatomic NiTi.

Table 3.14: Energy difference between B19′ and B19 structures determined by H_{eff} at different pressures.

Pressure (GPa)	$E_{B19'-B19}$ (meV/f.u.)
-5	-50
0	-35
5	-8.9

We now discuss comparison between our results with the work in Ref. [63] in which martensitic transition temperature was estimated using free energies obtained using thermodynamic integration within AIMD. While T_M predicted by our H_{eff} based analysis is underestimated with respect to experiment, free-energy based analysis [63] gives an overestimated T_M. As both the works are fundamentally based on density functional theory treated within the same approximation, it would appear that this discrepancy is likely due to further approximations or truncations in construction of the effective Hamiltonian. Indeed, this comparison uncovers important

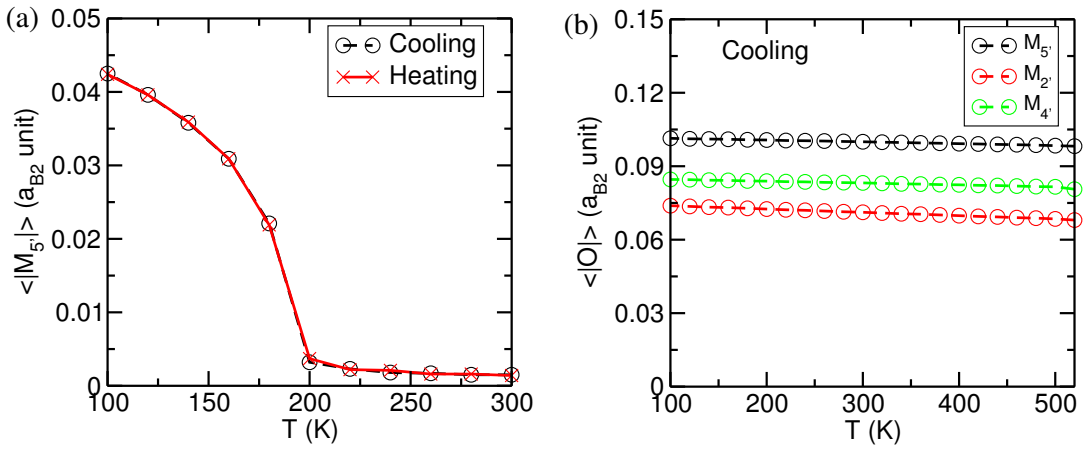

Figure 3.9: Absolute value of $M_{5'}$ modes (a), and absolute values of $M_{5'}$, $M_{2'}$ and $M_{4'}$ for strains clamped at zero, corresponding to the lattice parameters of B19′ structure (b) as a function of temperature at ambient pressure.

aspects of first-order structural phase transitions, which are typically fluctuation-driven first-order phase transition in which strain-phonon coupling plays a crucial role, as was shown in similar phase transitions in perovskite ferroelectrics [23, 101]. If fluctuations in strain ($\varepsilon_{\alpha\beta}$) are not allowed in a simulation, called as clamped lattice analysis, the same effective Hamiltonian gives a second order phase transition at much higher T_c. To verify this, we simulated our H_{eff} of NiTi with strain clamped at the lattice parameters of B2 and B19′'s structures and found that (a) the thermal hysteresis vanishes, confirming a second order transition, and (b) T_c's are much higher (200 K for zero strains of the cubic lattice, and higher than 500 K for strains clamped at the B19′'s lattice at P=0 GPa) (See Fig. 3.9). We note that free energy estimation in Ref. [63] is based on thermodynamic integration along a path in the structural (strain) space, and lattice constants are kept fixed in MD simulation at each point along this path. As fluctuations in strain are thus not included, the estimated T_M's from the resulting free energies are higher. More work is necessary to obtain deeper understanding of the martensitic transitions in this context.

The hysteresis found in the vicinity of martensitic transition in our heating and

cooling simulations is essentially due to first-order character of the martensitic transition, in a way similar to that found in simulations of ferroelectric phase transitions [23]. The origin of this has been identified in fluctuations generated by the strain-phonon coupling. While there is no time-scale in Monte Carlo simulations, the hysteresis does arise in our quasi-static simulations, in which temperature is varied in very small steps, and the system is equilibrated at each temperature. Such simulated hysteresis should apply to experimental measurements carried out at very slow rates of heating and cooling. As the systems simulated in our work (8192 atoms) are much too small, their phase transition occurs homogeneously, i.e. without nucleation and growth of domains (twins). Hence, it is not possible for such simulations to be directly related to M_s and M_f temperatures observed in experiments. The simulated phase transition occurs marking a sharp, global change in structure throughout the system. Indeed, our work forms a starting point of multi-scale modeling and simulations [102] that will allow us to treat much larger systems.

3.7 Landau theoretical analysis of H_{eff}

To determine the couplings that are responsible for the observed MT in NiTi, we now present a Landau theory obtained by projecting the H_{eff} into the subspace of phonons at M-point $\frac{\pi}{a}(011)$ and strain degrees of freedom, (i) $H_{eff}^{Ni}(\vec{\eta}_i)$ and $H_{eff}^{Ti}(\vec{\tau}_i)$ projected on $H_{ph}^{Landau}(\eta_x, \eta_y, \tau_x)$ (Eq. 3.12), and (ii) $H_{spc}(\vec{\eta}_i, \vec{\tau}_i, \varepsilon_{\alpha\beta})$ projected on $H_{spc}^{Landau}(\eta_x, \eta_y, \tau_x, \varepsilon_1, \varepsilon_2, \varepsilon_4, \varepsilon_5)$ (Eq. 3.13). To make Landau theoretical analysis simple, we exclude the high frequency $M_{5'}$ optical phonon mode, which has a negligible contribution to the relevant structures of NiTi (Table 3.15). While this simplification is made to facilitate analytical treatment, we include all the terms in our exact numerical analysis results of which are shown in Fig. 3.10. In the projected

subspace, η_y and η_z span the subspace of doubly degenerate unstable $M_{5'}$ phonon modes, η_x and τ_x span the subspace of $M_{2'}$ and $M_{4'}$ phonon modes respectively. We restrict to structures with the symmetry of orthorhombic and monoclinic phases of NiTi with $\eta_z = \eta_y$, $\varepsilon_3 = \varepsilon_2$ and $\varepsilon_6 = \varepsilon_5$, and write Hamiltonian in these subspace:

$$\begin{aligned} H_{ph}^{Landau}(\eta_x, \eta_y, \tau_x) &= a_1\eta_x^2 + a_2\eta_y^2 + a_3\tau_x^2 + a_4\eta_x^4 + a_5\eta_y^4 + a_6\eta_x^2\eta_y^2 \\ &+ a_7(\eta_x^2 + 2\eta_y^2)^3 + a_8(\eta_x^2 + 2\eta_y^2)^4, \end{aligned} \tag{3.12}$$

$$\begin{aligned} H_{spc}^{Landau}(\eta_x, \eta_y, \tau_x, \varepsilon_1, \varepsilon_2, \varepsilon_4, \varepsilon_5) &= (g_1\varepsilon_1 + g_2\varepsilon_2)\eta_x^2 + (g_3\varepsilon_1 + g_4\varepsilon_2 + g_5\varepsilon_4)\eta_y^2 \\ &+ g_6\varepsilon_5\eta_x\eta_y + g_7\varepsilon_5\tau_x\eta_y + g_8\varepsilon_4\eta_x\tau_x \\ &+ (g_9\varepsilon_1^2 + g_{10}\varepsilon_2^2 + g_{11}\varepsilon_1\varepsilon_2)\eta_x^2 \\ &+ (g_{12}\varepsilon_1^2 + g_{13}\varepsilon_2^2 + g_{14}\varepsilon_1\varepsilon_2)\eta_y^2, \end{aligned} \tag{3.13}$$

where a_i and g_i are the coefficients of phonon and strain-phonon coupling terms in the Landau energy function respectively (their values are listed in Table 3.16). The instability of $M_{5'}$ mode (a_2 =-8.4 eV/f.u. < 0) corresponds to $\{0\bar{1}1\}$ <0 1 1> shuffle, whose coupling with ε_1 (g_3=116.4 eV/f.u.) is positive, and with ε_2 (g_4=-188.6 eV/f.u.) is negative. Therefore, ε_1 must be negative and $\varepsilon_3 = \varepsilon_2$ positive to reduce the energy of system, consistent with Bain strain distortion that lowers the symmetry of cubic structure of NiTi to tetragonal one. Coupling of η_y with ε_4 ($\{010\}$<0 0 1> pure shear, g_5=-143.7 eV/f.u.), transforms B2 structure to B19 structure. Though η_x and τ_x represent stable phonons at M-point and linear elastic moduli are positive definite [103], the non-basal shear strain $\varepsilon_6 = \varepsilon_5$ couples strongly with η_x, τ_x and η_y (g_6= -126.3 eV/f.u. and g_7=137.4 eV/f.u.) stabilizing B19′ structure relative to B19 structure through structural distortions involving M_2' and M_4' modes. Rest of the terms in Landau energy function play a supporting role in giving correct details of

energetics and lattice parameters of B19 and B19′ structures. From exact analysis including all the terms, we determined the phase diagram of stability of B19 and B19′ structures (See Fig. 3.10) in the plane of these g-couplings, which can thus be used as descriptors of stability of these phases. If the values of these couplings (g_6 and g_7) were weak, B2 structure of NiTi would transform through its MT to B19 structure, not B19′. The primary order parameter (phonon mode $M_{5'}$) drives the MT, M_2' and M_4' modes and strains constitute the secondary order parameters of the MT in NiTi that determine stabilization of B19 vs B19′ phases. Our analysis suggests that the three order parameters [80] are not sufficient to study MT in NiTi.

Table 3.15: Values of amplitudes of LWFs and strains for different phases of NiTi, obtained using DFT, H_{eff} and H_{Landau}. LWFs are in unit of a_{B2}.

Phase	Method	$M_{5'}$ $\eta_y = \eta_z$	$M_{2'}$ η_x	$M_{4'}$ τ_x	$M_{5'}$ $\tau_y = \tau_z$	ε_1	$\varepsilon_2 = \varepsilon_3$	ε_4	$\varepsilon_5 = \varepsilon_6$
B19	DFT	0.075	0.000	0.000	-0.003	-0.057	0.031	0.099	0.000
	H_{eff}	0.093	0.000	0.000	-0.003	-0.064	0.038	0.145	0.000
	H_{Landau}	0.093	0.000	0.000	0.000	-0.062	0.037	0.146	0.000
B19′	DFT	0.095	0.066	-0.096	-0.002	-0.028	0.029	0.162	-0.141
	H_{eff}	0.102	0.075	-0.083	-0.004	-0.028	0.034	0.214	-0.177
	H_{Landau}	0.104	0.072	-0.083	0.000	-0.032	0.036	0.212	-0.172

3.8 Structural disorder and microstructures relevant to MT in NiTi

In addition to bulk crystalline phases, a martensitic transformation invariably involves planar faults and microstructures (e.g. twinning and stacking faults). We now demonstrate the efficacy of H_{eff} in capturing the physics of phases with structural disorder and microstructures in NiTi. We present stability analysis of (i) average austenitic structures reported in Refs. [104, 105], and (ii) $(100)[011]_{B2}$ twinning and stacking faults that occur in the martensitic B19′ structure.

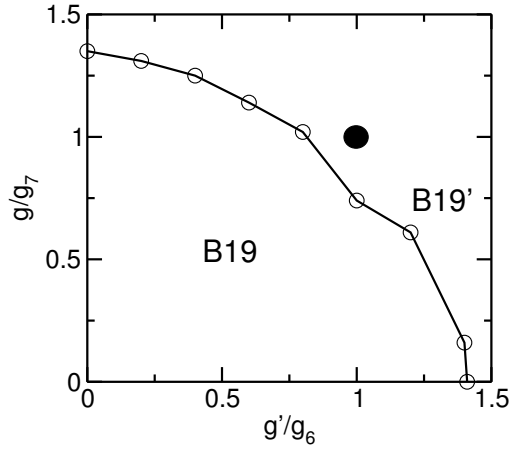

Figure 3.10: Phase-diagram of the relative stability of B19 and B19′ structures of NiTi as a function of third-order strain-phonon coupling coefficients g and g'. Black filled circle shows the actual values of g_6 and g_7 which falls in B19′ phase region in phase-diagram.

Table 3.16: Coefficients of terms in Landau energy function are linear combinations of the parameters in H_{eff}.

Landau coeff.	H_{eff} coeff.	Values (eV/f.u)
a_1	$4A_{11} + 4A_{21} + 4A_{22}$	9.2
a_2	$8A_{11} + 4A_{12} + 4A_{21} + 4A_{22} + 8A_{23}$	-8.4
a_3	$\frac{1}{2}\tilde{A}_{01} + 4\tilde{A}_{11} + 8\tilde{A}_{21} + 4\tilde{A}_{22}$	17.2
a_4	$32B_{41} + 64B_{45}$	468.9
a_5	$64B_{41} + 32B_{42} + 32B_{43} + 64B_{44} + 256B_{45}$	4.0×10^3
a_6	$64B_{42} + 64B_{44} + 256B_{45}$	2.1×10^3
a_7	$128B_{61}$	-3.7×10^4
a_8	$512B_{81}$	8.3×10^5
g_1	$8g_{31} + 8g_{32}$	-85.8
g_2	$16g_{31} + 8g_{35}$	-134.2
g_3	$16g_{31} + 8g_{33}$	116.4
g_4	$32g_{31} + 16g_{32} + 16g_{33} + 8g_{34} + 8g_{35}$	-188.6
g_5	$8g_{36}$	-143.7
g_6	$16g_{36} + 8g_{37}$	-126.3
g_7	$\frac{16}{3}h_{36}$	137.4
g_8	$\frac{8}{3}h_{34}$	28.0
g_9	$8g_{41} + 8g_{42}$	1.2×10^3
g_{10}	$16g_{41} + 8g_{43}$	-9.1
g_{11}	$16g_{44}$	-167.0
g_{12}	$16g_{41}$	235.0
g_{13}	$32g_{41} + 16g_{42} + 16g_{44}$	2.4×10^3
g_{14}	$16g_{43} + 16g_{44}$	-655.3

3.8.1 Stablity of average austenitic structures

To simulate the reported average austenitic structures, we start with B2 structure and relax its structural distortions in the subspace of unstable $M_{5'}$ phonons using

H_{eff} in MC simulation at T=10 K, constraning $\vec{\tau}_i's$ and ε to be zero. We find a structure resulting from a combination of two unstable $M_{5'}$ phonons at distinct M-points, $\frac{\pi}{a}(011)$ and $\frac{\pi}{a}(101)$, which break the translational symmetry of B2 structure, transforming it to a stable hexagonal austenite structure reported in Refs. [104,105]. This hexagonal structure (See Fig. 3.11a) has a periodic unit cell with 24 atoms (12 Ni and 12 Ti atoms) and $a_{hex} = b_{hex} = 2\sqrt{2}a$ and $c_{hex} = \sqrt{3}a$ (a is the lattice parameter of B2 structure) along $[0\bar{1}1]_{B2}$, $[\bar{1}01]_{B2}$ and $[111]_{B2}$ directions respectively. It is lower in the energy by 9.8 $meV/f.u.$ than the B2 structure, and higher in the energy by 71 $meV/f.u.$ than the B19′ structure. To stabilize this austenitic structure, Ni and Ti atoms displace from their high symmetry positions in the B2 structure along the eigenvectors of unstable $M_{5'}$ phonons such that the average structure remains B2. This is one of the many possible stable austenitic structures, and similar to the hexagonal structure of Refs. [104, 105]. The main difference between this hexagonal structure and that of Refs. [104, 105] is the size of the respective periodic unit cell. The hexagonal structure reported in Refs. [104,105] has 54-atoms unit cell, where $a_{hex} = b_{hex} = 3\sqrt{2}a$ and $c_{hex} = \sqrt{3}a$. Thus, H_{eff} does capture the physics and stability of average austenite structure like the one reported in Refs. [104, 105].

3.8.2 Microstructure of NiTi

To examine microstructures relevant to the MT in NiTi, we simulated $(100)[011]_{B2}$ twinning and stacking faults in its martensitic B19′ structure using H_{eff}. Separated by a (100) plane of the B2 structure, we introduced two domains (See Fig. 3.11b-3.11d) in a $L \times L \times L$ system. Domains (I, $x \leq L/2$) and (II, $x > L/2$) contain states of B19′ structure with distinct orientation, charecterized by order parameters. In the twinned structure, $M_{5'}$ and non-basal shear (ε_5 and ε_6) order parameters have opposite values in the two domains. On the other hand, in stacking faulted structure,

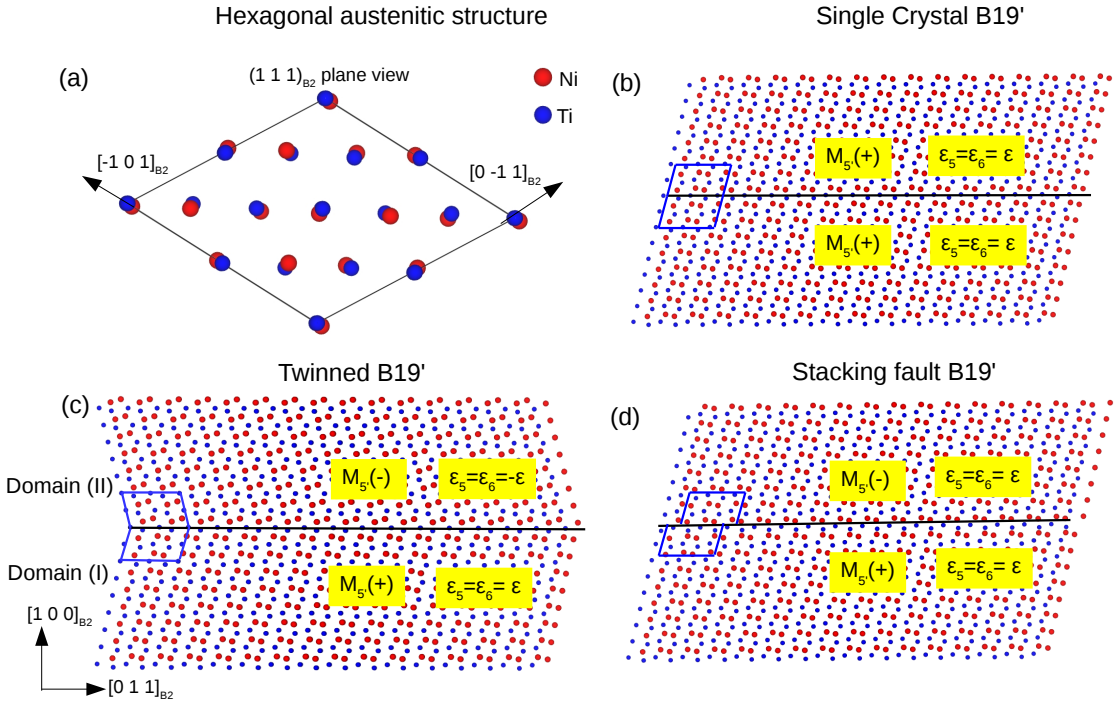

Figure 3.11: Analysis based on H_{eff} gives stable atomic structure of the hexagonal austenitic phase (a). Optimized atomic structures of single-crystal (b), twinned B19′ (c), and stacking faulted (d) B19′ phase of NiTi obtained from MC simulations of H_{eff} at 10 K temperature. Blue boxes in (b), (c) and (d) represent B19′ structural unit cell. $M_{5'}(+)$ is the primary order parameter, and $M_{5'}(-)$ represents its opposite value. ε_5 and ε_6 are the components of non-basal shear strain, which are the same in both domains of the stacking faulted structures, while have opposite values in the two domains of twinned structure of NiTi.

$M_{5'}$, $M_{2'}$ and $M_{4'}$ have opposite values in the two domains though non-basal shear strains are the same. Hydrostatic, Bain and pure shear strains (secondary order parameters) are same in both domains of twinned and stacking faulted structures. We constructed the twinning and stacking faults in B19′ structure of NiTi using the optimized values of order parameters obtained by H_{eff}. We estimated faults formation energy in B19′ structure of NiTi as follows.

$$E_{FE} = \frac{E_{FP} - nE_{B19'}}{2A}, \tag{3.14}$$

where E_{FE}, E_{FP} and $E_{B19'}$ are the faults (twinning and stacking fault) formation,

faulted plane and single crystal B19′ structure's energy, respectively. n is the number of unit cells lie on the plane which has the cross-sectional area A. Our estimates of the twinning and stacking fault energies using Eq. (3.14) are 96.3 mJ/m^2 and 217.4 mJ/m^2, respectively, confirming that twinning faults are more likely to occur than stacking faults in NiTi. Our MC simulations at T= 10 K initialized with the structures containing twinning and stacking faults reveal that both the structures remain stable in their respective forms, and that the twinned structure is lower in energy than the stacking faulted structure (See Table 3.17). While our H_{eff}-based estimates of twinning and stacking faults of NiTi are bit different in comparison with their DFT values [106], their relative stability is captured qualitatively well by our effective Hamiltonian. In the phonon-based theoretical framework of our H_{eff}, a ferroelastic domain wall separating domains of B19′ phases with distinct order parameters orientation give the planar twinning faults are known to be relevant to the MT in NiTi.

Table 3.17: The statistical averages of absolute values of $M_{5'}$, $M_{2'}$ and $M_{4'}$, averages of components of strain tensor in the different structures of NiTi calculated by MC simulations at T=10 K. $< |M_{5'}| >$, $< \varepsilon_5 >$ and $< \varepsilon_5 >$ are zero in twinned structure, $< |M_{5'}| >$, $< |M_{2'}| >$ and $< |M_{4'}| >$ are zero in stacking faulted strucures, because these parameters have opposite values in both domains of their respective faulted structures.

Statistical averages	Stable Austenitic structure	Single crystal B19′	Twinned B19′	Stacking fault B19′
$< E > (meV/f.u)$	-8.5	-77.0	-46.5	-14.9
$< \lvert M_{5'} \rvert >$	0.051	0.102	0	0
$< \lvert M_{2'} \rvert >$	0	0.075	0.075	0
$< \lvert M_{4'} \rvert >$	0	0.085	0.086	0
$< \varepsilon_1 >$	0	-0.027	-0.027	-0.023
$< \varepsilon_2 >$	0	0.033	0.033	0.032
$< \varepsilon_3 >$	0	0.033	0.033	0.032
$< \varepsilon_4 >$	0	0.215	0.214	0.212
$< \varepsilon_5 >$	0	0.177	0	0.177
$< \varepsilon_6 >$	0	0.177	0	0.177

3.9 Summary

In summary, we have presented a microscopic picture of martensitic phase transformation in NiTi in terms of its phonons and their interactions derived from first-principles and captured in an effective Hamiltonian. We have shown that vibrational entropy of soft modes stabilizes the monoclinic martensite B19′ structure over its BCO structure at T>43 K. Through Monte Carlo simulations of an effective Hamiltonian derived to capture its low-energy landscape of NiTi, we (a) determine its soft modes and establish the cell-doubling $M_{5'}$ phonon of the cubic phase as the primary order parameter of MT, and (b) there are SIX other secondary order parameters that are relevant to the MT in NiTi. We show that pressure can introduce an intermediate phase during the MT, thanks to the interesting physics of seven coupled order parameters. Using Landau theoretical analysis, we show that relative strengths of the third-order coupling between primary and secondary order parameters including strain determine the specific symmetry of low-T structures emerging from its MT. These can be used as first-principles descriptors in designing materials with improved shape memory properties through substitutional alloying in NiTi. We finally show that our H_{eff} qualitatively captures stability of other stable average austenitic structures, twinning and stacking faults in NiTi, which are relevant to its MT.

Chapter 4

Martensitic Structural Transformation in PtTi: A High-temperature Shape Memory Alloy

4.1 Introduction

High-temperature shape memory alloys (HTSMAs) have been used extensively to improve the efficiency of the automotive, aerospace and energy exploration industries. HTSMAs undergo a martensitic transformation (MT) at $T_M > 400$ K [107], and exhibit a shape memory effect [52]. Though the binary NiTi alloy is a promising shape memory alloy (SMA), its martensitic transformation temperature (T_M) is close to room temperature [77], which limits its use in high-temperature shape memory applications. However, MT in binary PtTi occurs at a much higher temperature T_M =1343 K [108], making it ideal for use in technological high-temperature shape memory applications. Experimentally [108–111], it was found that the crystal

of PtTi changes from cubic B2 structure to orthorhombic B19 structure during the MT, B19 being its ground state. However, first-principles calculations concluded that B19′ is the ground state structure of PtTi [60, 112] and not B19. Thermal properties of the B2 structure of PtTi have been studied using first-principles calculation, and martensitic transformation using P^4 method [113]. They estimated $T_M = 1171$ K, in good agreement with experiment. Fundamental understanding of (i) the ground state structure, relative stability of B19 and B19′ structures, and (ii) the precise atomistic mechanism of the MT in PtTi still needs to be understood.

Metallurgists typically explain MT using strain as the order parameter, the best example being the BCC-FCC transformation in steel [10]. Within soft-mode theory [114] it was argued that soft-phonon mode, strain and their couplings are important to structural phase transitions, and successfully explained this kind of phase transformations in ferroelectric materials [22, 115]. This approach has been extended successfully to study MT in NiTi SMA [45]. The biggest advantage of this theory is that we start from high-symmetry structure as the reference and identify soft-phonon modes and their symmetry allowed coupling with strain governing the structural transformations. First-principles calculations have been used [112] to calculate energetics of different structures of PtTi, reporting which phonon modes are responsible for its martensitic transformation in PtTi. However, the issue of the ground state and thorough statistical mechanical analysis of the MT in PtTi are needed for its deeper understanding.

In this chapter, we present detailed first-principles and Landau theoretical analysis of the MT in PtTi with focus on soft-phonon modes and strain and goal to uncover the microscopic governing mechanisms and couplings. Using this, (i) we determine, the primary and secondary order parameters, and (ii) identify the microscopic coupling between strain and phonons, which are responsible for the MT. Our

goal here is to give a thorough analysis of MT in PtTi within the framework of effective Hamiltonian (H_{eff}) that we used in chapter 3 to study MT in NiTi. In Sec. 4.2, we present details of first-principles calculations and crystal structures of different phases of PtTi. In Sec. 4.3, we present phonon spectra and dispersion of B2, B19 and B19′ structures, T-dependent free energies of B19 and B19′ structures to resolve the issue of their relative stability at low-T. In Sec. 4.4, we find the relevant symmetry invariant subspace of phonons and order parameters involved in MT in PtTi. In Sec. 4.5, we determine PtTi-specific parameters of the effective Hamiltonian to capture low-energy landscape of its B19 structure. In Sec. 4.6, we present results of Monte Carlo simulations of H_{eff} to determine temperature dependent MT in PtTi, followed by Landau theoretical analysis in Sec. 4.7 to identify specific couplings in H_{eff} that stabilize its low-T structure, and finally, we summarize our work in Sec. 4.8.

4.2 First-principles computational details and structural parameters

Our first-principles calculations within the density functional theory (DFT) are based on the plane-wave pseudopotential scheme as implemented in the Quantum Espresso (QE) package [81], with a generalized gradient approximation (GGA) and Perdew-Burke-Ernzerhof (PBE) [32] form of exchange-correlation energy functional. We use an energy cutoff of 40 Ry and 320 Ry to truncate the plane-wave basis set for representing Kohn-Sham wave functions and charge density respectively. In self-consistent Kohn-Sham (KS) calculations with primitive unit cells, Brillouin zone (BZ) integrations were sampled on uniform meshes of $20 \times 20 \times 20$ k-points for B2 structure, and $20 \times 12 \times 12$ k-points for B19 and B19′ structures. We relaxed structures to minimize energy with respect to lattice parameters and atomic positions

until the magnitude of stresses are less than 3 kbar and Hellmann-Feynman force on each atom is less than 5 meV/$\mathring{A}$. We determined lattice-dynamical properties of PtTi phases within the framework of density functional perturbation theory (DFPT) as implemented in QE code [81]. Phonons and dynamical matrices were obtained on a uniform $6 \times 6 \times 6$ q-point mesh in BZ for B2, and $2 \times 2 \times 2$ q-point mesh in the BZ for B19 and B19′ structures.

We obtained the structural parameters and energies of B2, B19 and B19′ structures of PtTi using first-principles simulations, and benchmarked our methods through good agreement with earlier theoretical results [112], reconfirming that B19′ is the ground state of PtTi (See Table 4.1). Though B19′ structure is not yet observed experimentally, our calculated lattice parameters of B2 and B19 structures are in good agreement with experimental results [109].

Table 4.1: Crystal structural parameters (4 atoms per unit cell) and energies of B2, B19 and B19′ structures of PtTi relative to B19 structure as a reference, obtained by DFT calculations.

Phase	Space group	Method	a($\mathring{A}$)	b($\mathring{A}$)	c($\mathring{A}$)	γ^o	$E - E_{B19'}$(meV/f.u)
B2	$Pm\bar{3}m$	GGA	3.18	4.50	4.50	90	267.8
		LDA [112]	3.13	4.43	4.43	90	151.2
		Exp. [109]	3.19	4.51	4.51	90	
B19	Pmma	GGA	2.78	4.87	4.63	90	0
		LDA [112]	2.73	4.80	4.55	90	0
		Exp. [109]	3.73	4.79	4.55	90	
B19′	$P2_1/m$	GGA	2.78	4.89	4.61	93.5	-4.9
		LDA [112]	2.74	4.82	4.53	93.6	-4.9

4.3 Phonon spectra and relative stability of PtTi phases

To determine the thermodynamic stability of B2, B19 and B19′ structures at low-temperature, we calculated their phonon dispersion using DFPT. We find that $M_{5'}$

phonon mode is the strongest lattice instability of B2 structure (ω $\sim$97i cm^{-1}, Fig. 4.1a) and is in good agreement with results of Ref. [112, 116]. In the phonon dispersion of B19 structure, one of the transverse acoustic (TA) phonon branches is unstable (ω $\sim$50i cm^{-1}) along $\Gamma \rightarrow Y$ direction (Fig. 4.1b) making it an unstable structure at T=0 K. Phonon dispersion of B19$'$ structure, the ground state, exhibits no instability anywhere in the Brillouin zone (Fig. 4.1c). We now estimate the free energies of B19 and B19$'$ within the harmonic (stable phonons) and anharmonic (unstable phonons) approximation of quantum oscillators using Eq. (3.1). At T = 0 K, $\Delta G = G_{B19'} - G_{B19}$ = -1.60 meV/f.u., confirms that theoretically B19$'$ is stable against B19 structures at low-temperature. However, at T > 112 (133) K B19 structure gains stability relative to B19$'$ structure based on the free energy estimated with (without) including contributions of unstable modes to free energy of B19 structure (Fig. 4.1d), thus providing a possible solution to the issue of B19$'$ structure as unexpected ground state of PtTi. Inclusion of contributions of the unstable modes to free energy leads to stabilization of B19 structure at a slightly lower temperature (Fig. 4.1d), because weak instabilities in the TA phonon branch of B19 structure contribute strongly to vibrational entropy. We note that the difference between structural parameters and energetics of B19 and B19$'$ structure is rather small (Table 4.1) and their relative stability depends on quantum vibrational energy which is not captured by Monte Carlo or Molecular dynamics simulations. Therefore, we will focus on the energy landscape B2 and B19 structures in our statistical mechanical analysis of the MT.

4.4 Identification of order parameters

We identified the order parameters of the martensitic tranformation in PtTi, that link its low-symmetry B19 and high-symmetry B2 structures in terms of phonon and

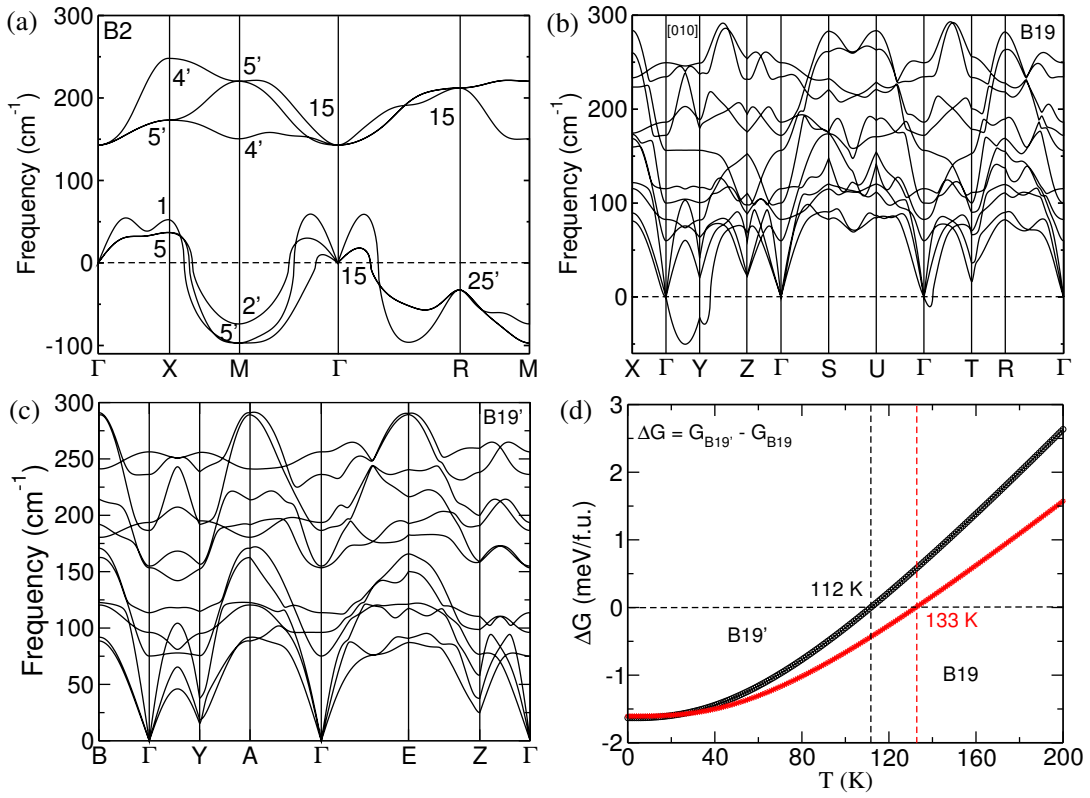

Figure 4.1: Phonon dispersion of B2 (a), B19 (b), B19′ (c) structures of PtTi obtained using DFPT calculations. Unstable modes with imaginary frequencies ($\omega^2 < 0$) are shown with negative values. Difference between free-energies of B19′ and B19 structures black (red) lines show with (without) contribution of unstable modes of B19 structure to free energy (d). It is clear, B19 structure is stabilized above 112 (133) K by vibrational entropy with (without) including unstable phonons of B19 in free energy.

strain modes of the B2 structure. Phonon modes and strains of B2 structure take into account of atomic displacements and lattice distortion of this structure, respectively. $M_{5'}$ phonon at M-point ($\frac{\pi}{a}(011)$) drives the B2 to B19 structural transformation with orthorhombic lattice distortion of $1 \times \sqrt{2} \times \sqrt{2}$ super-cell of B2 structure (Fig. 3.4a, 3.4d in chapter 3). It being the strongest lattice instability of B2 structure, $M_{5'}$ mode is the primary order parameter. The quantitative estimation of amplitudes of phonons and strains involved as order parameters in B2 to B19 transformation are listed in Table 4.2. It is evident from our results that four order parameters $M_{5'}$ phonon mode, Bain strain (s_2), hydrostatic strain (s_3) and pure shear (s_4) are the

order parameters of B2 to B19 transformation.

Table 4.2: Order parameters (M-point phonon modes at $\vec{q} = \frac{\pi}{a}(011)$ of the cubic B2 structure and strain tensor components) associated with B19 structure, obtained from first-principles calculations. The amplitudes of phonon eigenmodes are in unit of lattice constant of B2 structure, and phonon eigenmodes are expressed in terms of atomic displacements $\hat{e}_{ph} = |Ti_x, Ti_y, Ti_z, Pt_x, Pt_y, Pt_z >$. The strain eigenmodes $s = |\varepsilon_1, \varepsilon_2, \varepsilon_3, \varepsilon_4, \varepsilon_5, \varepsilon_6 >$, are in the Voigt notation.

Modes	Eigenmode	Character	B2	B19
$M_{5'}$	$\|0, 0.51, 0.51, 0, 0.86, 0.86 >$	$\{0\bar{1}1\}$<011> Basal shuffle	0	0.085
$M_{2'}$	$\|0, 0, 0, 1, 0, 0 >$	$\{0\bar{1}1\}$<100>, Pt displacements	0	0
$M_{4'}$	$\|1, 0, 0, 0, 0, 0 >$	$\{0\bar{1}1\}$<100>, Ti displacements	0	0
s_1	$\frac{1}{\sqrt{2}}\|0, 1, -1, 0, 0, 0 >$	$\{0\bar{1}1\}$<011> Basal shear	0	0
s_2	$\frac{1}{\sqrt{6}}\|-2, 1, 1, 0, 0, 0 >$	Bain strain	0	0.149
s_3	$\frac{1}{\sqrt{3}}\|1, 1, 1, 0, 0, 0 >$	Hydrostatic strain	0	-0.006
s_4	$\|0, 0, 0, 1, 0, 0 >$	{010}<001> Pure shear	0	0.054
s_5	$\frac{1}{\sqrt{2}}\|0, 0, 0, 0, 1, 1 >$	{100}<011> Non-basal shear	0	0

4.5 Effective Hamiltonian

Both PtTi and NiTi have the same structure (B2) of the austenite phase, and their martensitic transformations are governed by M-point phonon and strain modes. Subspaces of acoustic and optical phonons of PtTi are separated by a gap in frequencies (Fig. 4.1a) like in NiTi (Fig. 3.3a in chapter 3), and these phonons dominated by Pt and Ti displacements respectively. Though in NiTi seven order parameters ($M_{5'}$, $M_{2'}$, $M_{4'}$, s_2, s_3, s_4 and s_5, see Table 3.2 in chapter 3) are involved where transformation occurs from B2 to B19′ structure, only four order parameters ($M_{5'}$, s_2, s_3 and s_4) are involved in the transformation from B2 to B19 structure of PtTi. These four order parameters are common to the MTs of the two alloys. The similarity between MTs in PtTi and NiTi allows us to use the same form of effective Hamiltonian (H_{eff}) to explain MT in PtTi, though the coefficients in this Hamiltonian are PtTi-specific. Subspace of acoustic phonons in NiTi and PtTi are dominated by Ni and Pt displacements respectively. Therefore, here we replace the Ni-centric LWFs to Pt-centric LWFs to represent the subspace of acoustic phonons. Now, H_{eff}

can be expressed as an explicit symmetry invariant Taylor expansion in Pt-centric LWFs ($\vec{\eta}_i$), Ti-centric LWFs ($\vec{\tau}_i$) and strains ($\varepsilon_{\alpha\beta}$), i indicating the lattice unit cell to which $\vec{\eta}_i$ and $\vec{\tau}_i$ belong. H_{eff} consists of four parts:

$$H_{eff} = H_{eff}^{Pt}(\vec{\eta}_i) + H_{eff}^{Ti}(\vec{\tau}_i) + H_{spc}(\vec{\eta}_i, \vec{\tau}_i, \varepsilon_{\alpha\beta}) + H_{elastic}(\varepsilon_{\alpha\beta}), \tag{4.1}$$

where $H_{eff}^{Pt}(\vec{\eta}_i)$ and $H_{eff}^{Ti}(\vec{\tau}_i)$ operate in the subspaces of acoustic and optic phonons respectively. $H_{elastic}(\varepsilon_{\alpha\beta})$ is the linear and nonlinear elastic energy of homogeneous strain $\varepsilon_{\alpha\beta}$, and the coupling of $\varepsilon_{\alpha\beta}$ with both sets of LWFs is included in $H_{spc}(\vec{\eta}_i, \vec{\tau}_i, \varepsilon_{\alpha\beta})$. The detailed derivation of this Hamiltonian and procedure for computing its parameters are presented in Sec.3.5 of chapter 3. We follow here the same procedure to determine H_{eff} of PtTi. Calculated coefficients of phonon and strain-phonon couplings part of H_{eff} are listed in Table 4.3, while non-linear elastic moduli of the B2 structure (coefficients of $H_{elastic}(\varepsilon_{\alpha\beta})$) of PtTi are listed in Table 4.4.

Though the B19′ structure is the ground state of PtTi, it destabilzes to B19 structure due to quantum fluctuations. Our H_{eff} thus does not capture the details B19′ structure. Our H_{eff} reproduces the lattice parameters and energies of B19 structure with negligible errors relative to the first-principles results (Table 4.5).

4.6 Monte Carlo simulations

Having derived the H_{eff} of PtTi from first-principles, we now present analysis with Monte Carlo (MC) simulations of H_{eff} on a periodic system containing $L \times L \times L$ (L = 16) unit cells of B2 structure of PtTi. We used Metropolis algorithm with a single-flip update of configurational variables $\{\vec{\eta}_i, \vec{\tau}_i\}$ maintaining the acceptance ratio of ~ 0.5 near transformation temperature. In every Monte Carlo sweep (MCS),

Table 4.3: Coefficients of harmonic (A_{ij} and $\tilde{A}_{ij}$), anharmonic (B_{ij}) phonons and strain-phonon couplings (g_{ij} and h_{ij}) terms in the effective Hamiltonian in the unit of eV/f.u., obtained with first-principles calculations.

Coeff.	Values	Coeff.	Values	Coeff.	Values
A_{11}	-5.0	$\tilde{A}_{11}$	-3.0	B_{41}	104.8
A_{12}	0.2	$\tilde{A}_{12}$	16.3	B_{42}	260.4
A_{21}	2.0	$\tilde{A}_{21}$	1.5	B_{43}	83.7
A_{22}	-1.7	$\tilde{A}_{22}$	-2.3	B_{44}	-78.5
A_{23}	-1.4	$\tilde{A}_{31}$	-0.5	B_{45}	6.9
A_{31}	2.2	B_{31}	-13.7	B_{46}	-0.9
A_{32}	3.2	B_{32}	-6.5	B_{61}	-1373.4
$\tilde{A}_{01}$	58.2	B_{33}	-7.8	B_{81}	7893.5
g_{31}	1.3	g_{37}	17.0	h_{32}	70.3
g_{32}	-18.7	g_{41}	2.0	h_{33}	51.9
g_{33}	23.4	g_{42}	304.3	h_{34}	28.6
g_{34}	-55.3	g_{43}	-62.0	h_{35}	12.2
g_{35}	-19.2	g_{44}	-86.2	h_{36}	19.3
g_{36}	-21.0	h_{31}	-39.3	h_{37}	10.4

Table 4.4: Elastic moludi of $H_{elastic}(\varepsilon)$ in GPa, determined from first-principles.

Coeff.	Values	Coeff.	Values	Coeff.	Values
C_1	-1	C_{144}	-474	C_{1144}	5093
C_{11}	174	C_{155}	-464	C_{1155}	2352
C_{12}	257	C_{456}	-426	C_{1255}	1251
C_{44}	63	C_{1111}	11381	C_{1266}	664
C_{111}	-862	C_{1112}	-3355	C_{1456}	1273
C_{112}	-751	C_{1122}	4510	C_{4444}	3146
C_{123}	-1020	C_{1123}	4526	C_{4455}	1335

Table 4.5: Structural parameters (4 atoms per unit cell) and energies of B2 and B19 structures relative to B19, obtained using first-principles and H_{eff}.

Phase	Method	a($\mathring{A}$)	b($\mathring{A}$)	c($\mathring{A}$)	γ^o	$E - E_{B19}$(meV/f.u)
B2	GGA	3.18	4.50	4.50	90.0	267.8
	H_{eff}	3.18	4.50	4.50	90.0	268.6
B19	GGA	2.78	4.87	4.63	90.0	0.0
	H_{eff}	2.81	4.93	4.55	90.0	0.0

we picked η_i, τ_i randomly (totally $2L^3$ updates) and homogeneous strain variables L times. Therefore, every MCS has a total $(2L^3 + L)$ attempts for updating the configuration of model system. In order to recognize austenite and martensite phases from configurations used in Monte Carlo simulations, we collected absolute values of the Fourier components of η_i and τ_i, obtained averages of $M_{5'}$, $M_{2'}$ and $M_{4'}$ phonon modes, and averages of strain ($< \varepsilon >$) at each temperature. We performed our MC simulations by cooling and heating the system in the range of 400 to 700 K temperature to assess the possibility of hysteresis. In cooling simulations, we start with B2 structure from 700 K temperature, equilibrate the system into this structure, and decrease the temperature in steps of 10 K (2 K near the transformation temperature), down to a low-temperature of 400 K. In heating simulations, we start from T=400 K taking B19 structure as the initial configuration (though results do not depend on the choice of the initial configuration of system), and increase the temperature in steps of 10 K (2 K near the transformation temperature) to a high-temperature of 700 K. At each temperature, we used 10000 MCS for thermal equilibration and 50000 MCS for statistical averaging of various observables.

Averages absolute value of the primary order parameter $M_{5'}$ (Fig. 4.2a) vanishes at high-temperatures, and changes discontinuously to a non-zero value at T $< T_M$. In cooling simulations, this discontinuity marks the martensitic transformation at $T_M = 536$ K. In heating simulations, our model transforms the martensite phase into the austenite phase at $T_A = 542$ K. Average values of $M_{2'}$ and $M_{4'}$ modes remain zero throughout the temperature range (Fig. 4.2a), and confirm that PtTi transforms from B2 to B19 structure in the martensitic transformation. Discontinuity in primary order parameter at the transformation temperature and hysteresis of 6 K temperature in cooling and heating simulations reveal first-order character of this transformation. Histograms of the primary order parameter obtained from cooling (Fig. 4.2d) simulations reveal (i) relatively narrow distributions and (ii) a

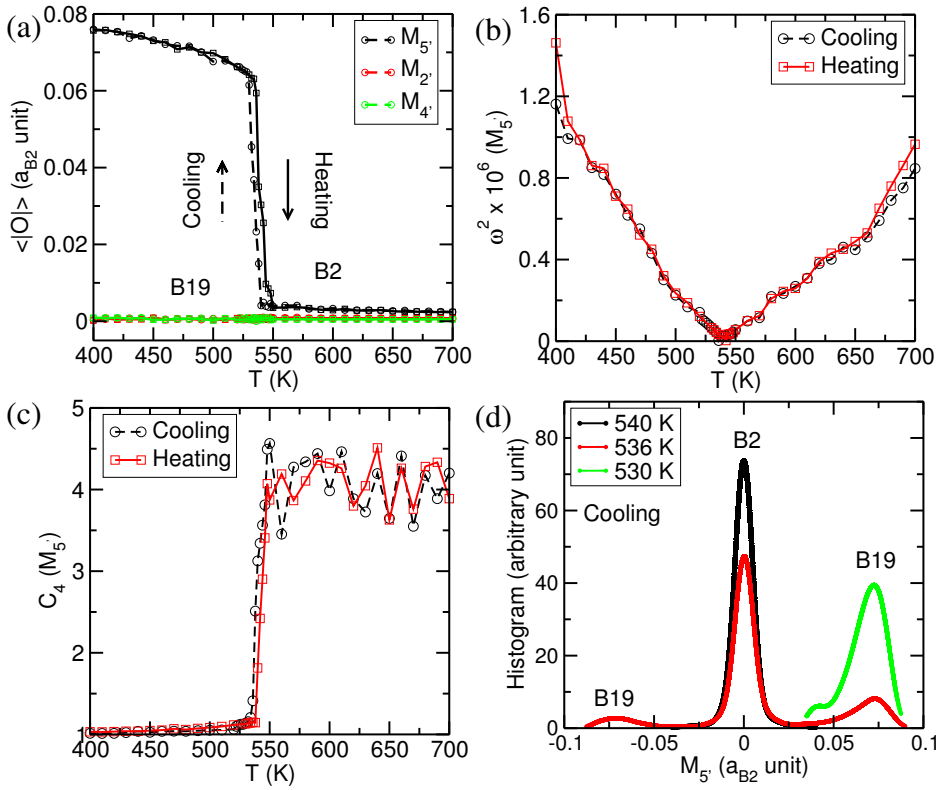

Figure 4.2: Averages of absolute values of $M_{5'}$, $M_{2'}$ and $M_{4'}$ modes (a) as a function of temperature at ambient pressure. Square of frequency of $M_{5'}$ phonon (b), its Binder cumulant (c), and histograms of $M_{5'}$ mode obtained from configurations sampled during cooling (d) at T_M and its nearest temperatures.

sharp jump across $T = T_M$. The bimodal nature of the histogram at T_M confirms the coexistence of B2 and B19, and hence first-order character of the MT. For further confirmation of these results, we obtained square of frequency (ω) and Binder fourth-order cumulant (C_4) of the primary order parameter (M_5' mode) using Eq. (3.10) and Eq. (3.11) respectively, in both cooling and heating runs of simulations. Softening of $M_{5'}$ phonon frequency and its T-coefficients (Fig. 4.2b) below and above T_M, and a discontinuity in C_4 (Fig. 4.2c) of M_5' mode at T = 536 (542) K in cooling (heating) confirm that $M_{5'}$ mode is the primary order parameter of MT in PtTi. The equilibrium transformation temperature ($T_c = \frac{1}{2}(T_M + T_A) = 539$ K) is much underestimated here with respect to experiment ($T_c = 1318$ K), similar to the errors in martensitic transformation in NiTi [45] and ferroelectric phase transition in

$PbTiO_3$ [23]. This is probably because of the GGA-DFT errors in energies and structural parameters and needs further investigation.

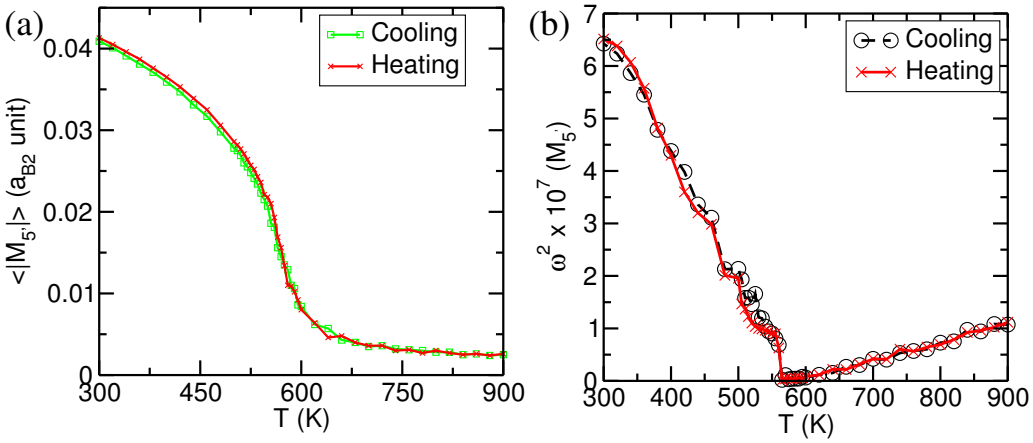

Figure 4.3: Average of absolute value (a) and square of frequency (b) of primary order parameter $M_{5'}$ mode as a function of temperature in the clamped lattice parameters of B2 structure of PtTi.

We now discuss the clamped lattice analysis of our effective Hamiltonian uncovering important aspects of first-order phase transformation where the strain-phonon coupling plays a crucial role. To verify this, we performed Monte Carlo simulations using the same H_{eff} of PtTi with strain clamped at the lattice parameters of B2 structure ($\varepsilon_{\alpha\beta} = 0$) and find that (i) the thermal hysteresis vanishes that confirming a second order phase transition, and (ii) $T_c = 565$ K (Fig. 4.3a and b). If fluctuations in strain are not allowed in simulation, the same H_{eff} may give a second order transformation at much higher temperature T_c.

4.7 Landau theoretical analysis of H_{eff}

To determine the specific couplings in H_{eff} that are relevant to the martensitic transformation in PtTi, we present a Landau theoretical analysis by projecting the full effective Hamiltonian into the subspace of phonons at M-point ($\frac{\pi}{a}(011)$) and strain degrees of freedom (Eq. 4.2 and 4.3). In the projected subspace, η_y and η_z

span the subspace of doubly degenerate unstable $M_{5'}$ phonon modes, η_x and τ_x span the subspace of $M_{2'}$ and $M_{4'}$ phonon modes respectively. Unlike in NiTi, the contribution of doubly degenerate high frequency $M_{5'}$ optical phonon mode (τ_y and τ_z) also have significant contribution (Table 4.6) in the MT in PtTi that directly relate to the atomic displacements. Therefore, we have included these variables in our analysis of Landau theory of PtTi. We restrict the resulting structures of projected Hamiltonian to the symmetry of relevant martensitic phases of PtTi with $\eta_z = \eta_y$, $\tau_z = \tau_y$, $\varepsilon_3 = \varepsilon_2$ and $\varepsilon_6 = \varepsilon_5$, and Hamiltonian of their coupled dynamics:

$$\begin{aligned} H_{ph}^{Landau}(\eta,\tau) &= a_1\eta_x^2 + a_2\eta_y^2 + a_3\tau_x^2 + a_4\tau_y^2 + a_5\eta_x^4 + a_6\eta_y^4 + a_7\eta_x^2\eta_y^2 \\ &+ a_8(\eta_x^2 + 2\eta_y^2)^3 + a_9(\eta_x^2 + 2\eta_y^2)^4 \end{aligned} \tag{4.2}$$

$$\begin{aligned} H_{spc}^{Landau}(\eta,\tau,\varepsilon) &= (g_1\varepsilon_1 + g_2\varepsilon_2)\eta_x^2 + (g_3\varepsilon_1 + g_4\varepsilon_2 + g_5\varepsilon_4)\eta_y^2 \\ &+ g_6\varepsilon_5\eta_x\eta_y + g_7\varepsilon_5\tau_x\eta_y + g_8\varepsilon_4\eta_x\tau_x \\ &+ (g_9\varepsilon_1 + g_{10}\varepsilon_2 + g_{11}\varepsilon_4)\eta_y\tau_z + g_{12}\varepsilon_5\eta_x\tau_y \\ &+ (g_{13}\varepsilon_1^2 + g_{14}\varepsilon_2^2 + g_{15}\varepsilon_1\varepsilon_2)\eta_x^2 \\ &+ (g_{16}\varepsilon_1^2 + g_{17}\varepsilon_2^2 + g_{18}\varepsilon_1\varepsilon_2)\eta_y^2 \end{aligned} \tag{4.3}$$

where a_i's and g_i's are the coefficients of phonons and strain-phonon coupling terms in the Landau energy function respectively and their values are listed in Table 4.7. The instability of $M_{5'}$ mode (a_2 =-49.1 eV/f.u. < 0) corresponds to $\{0\bar{1}1\}$ <0 1 1> shuffle, whose coupling with ε_1 (g_3=208.7 eV/f.u.) is positive, and with ε_2 (g_4=-478.1 eV/f.u.) is negative. Therefore, ε_1 must be negative and $\varepsilon_3 = \varepsilon_2$ positive to minimize the energy of system, consistent with Bain strain distortion that lowers the symmetry of cubic structure of PtTi to tetragonal one. Coupling of η_y with ε_4 ($\{010\}$<0 0 1> pure shear, g_5=-167.7 eV/f.u.) transforms B2 structure to B19 structure.

Table 4.6: Values of LWF at M-point $\pi/a(011)$ and strains for different phases of PtTi obtained using first-principles and effevtive Hamiltonian.

Phase	Method	ε_1	$\varepsilon_2 = \varepsilon_3$	ε_4	$\varepsilon_5 = \varepsilon_6$	η_x	$\eta_y = \eta_z$	τ_x	$\tau_y = \tau_z$
B2	GGA	0.000	0.000	0.000	0.000	0.000	0.000	0.000	0.000
	H_{eff}	0.000	0.000	0.000	0.000	0.000	0.000	0.000	0.000
B19	GGA	-0.125	0.057	0.054	0.000	0.000	0.085	0.000	-0.014
	H_{eff}	-0.116	0.056	0.086	0.000	0.000	0.088	0.000	-0.016

Table 4.7: Coefficients of terms in Landau energy function are linear combinations of the parameters in H_{eff}.

Landau coeff.	H_{eff} coeff.	Values (eV/f.u)
a_1	$4A_{11} + 4A_{21} + 4A_{22}$	-18.8
a_2	$8A_{11} + 4A_{12} + 4A_{21} + 4A_{22} + 8A_{23}$	-49.1
a_3	$\frac{1}{2}\tilde{A}_{01} + 4\tilde{A}_{11} + 8\tilde{A}_{21} + 4\tilde{A}_{22}$	20.1
a_4	$\tilde{A}_{01} + 8\tilde{A}_{11} + 4\tilde{A}_{12} + 16\tilde{A}_{21} + 4\tilde{A}_{22}$	114.9
a_5	$32B_{41} + 64B_{45}$	3.8×10^3
a_6	$64B_{41} + 32B_{42} + 32B_{43} + 64B_{44} + 256B_{45}$	1.4×10^4
a_7	$64B_{42} + 64B_{44} + 256B_{45}$	1.3×10^4
a_8	$128B_{61}$	-1.8×10^5
a_9	$512B_{81}$	4.0×10^6
g_1	$8g_{31} + 8g_{32}$	-139.2
g_2	$16g_{31} + 8g_{35}$	-132.2
g_3	$16g_{31} + 8g_{33}$	208.7
g_4	$32g_{31} + 16g_{32} + 16g_{33} + 8g_{34} + 8g_{35}$	-478.1
g_5	$8g_{36}$	-167.7
g_6	$16g_{36} + 8g_{37}$	-200.1
g_7	$\frac{16}{3}h_{36}$	103.2
g_8	$\frac{8}{3}h_{34}$	76.3
g_9	$\frac{16}{3}h_{31}$	-209.8
g_{10}	$\frac{16}{3}(2h_{31} + h_{32} + h_{33}$	231.9
g_{11}	$\frac{16}{3}h_{35}$	64.9
g_{12}	$\frac{16}{3}h_{37}$	55.3
g_{13}	$8g_{41} + 8g_{42}$	2.4×10^3
g_{14}	$16g_{41} + 8g_{43}$	-464.8
g_{15}	$16g_{44}$	-1.3×10^3
g_{16}	$16g_{41}$	31.4
g_{17}	$32g_{41} + 16g_{42} + 16g_{44}$	3.6×10^3
g_{18}	$16g_{43} + 16g_{44}$	-2.4×10^3

Though the $M_{2'}$ mode also unstable (a_1 =-18.8 eV/f.u < 0), its fourth-order phonon-phonon coupling ($a_7 = 1.3 \times 10^4$) with $M_{5'}$ mode and strain suppress its

contribution in MT. In further analysis of third order strain-phonon couplings, we found that couplings of non-basal shear $\varepsilon_6 = \varepsilon_5$ with η_x, τ_x and η_y (g_6= -200.1 eV/f.u. and g_7=103.2 eV/f.u.) are relatively weak (Fig. 4.4) and do not favor of B2 to B19′ transformation. Rest of the terms in Landau energy function play a supporting role to capture correct energetics and lattice parameters of B19 structure. We derived the phase diagram of stability of B19 and B19′ structures (Fig. 4.4) in the plane of these g-couplings, the descriptors of stability of these phases. It is clear from the phase diagram that B2 structure of PtTi would transform through its MT to B19′ structure instead of B19 if the values of these couplings (g_6 and g_7) were strong. The couplings between primary order parameter (phonon mode $M_{5'}$) driving the MT and strains as the secondary order parameters determine the relative stabilization of B19 versus B19′ phases.

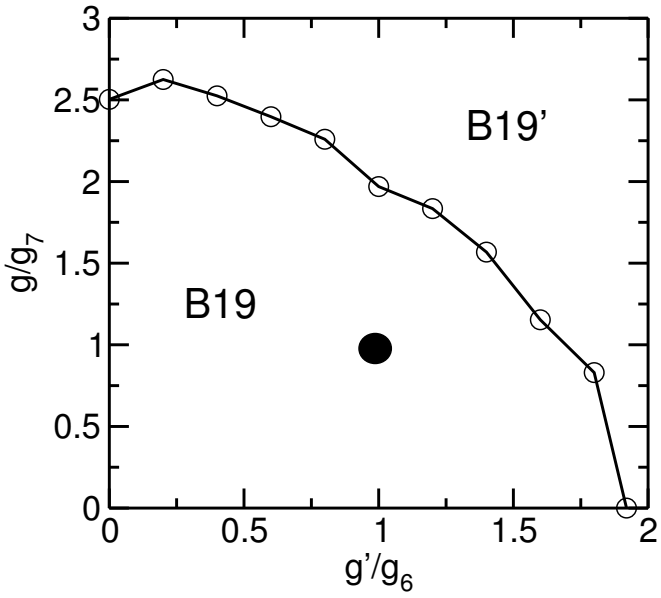

Figure 4.4: Phase diagram of the relative stability of B19 and B19′ structures of PtTi as a function of third-order strain-phonon coupling coefficients g and g'. Black filled circle shows the actual values of g_6 and g_7 which falls in the B19 structure region in phase-diagram.

4.8 Summary

We presented a possible resolution of the issue of ground state structure (B19 versus B19′) of PtTi by calculating their free energies: we show that vibrational entropy of soft modes stabilizes the B19 martensite structure at T>112 K. Through an effective Hamiltonian of PtTi derived from first-principles, we (a) determine its soft modes and establish the cell-doubling $M_{5'}$ phonon of the cubic phase as the primary order parameter of MT, and (b) there are three other secondary order parameters that are relevant to the MT in PtTi. Through Landau theory, we show that relative strengths of the third-order coupling of the primary order parameter with secondary order parameters determine the specific symmetry of low-T structures emerging at its MT. Most importantly, successful description of the martensitic transformation in PtTi validates our effective Hamiltonian approach, and opens up the avenue to study MTs in other materials.

Chapter 5

Theory of β to α Phase Transformation in Titanium

5.1 Introduction

Titanium (Ti) is an important metallic material widely used in industrial, aerospace, marine and medical applications. The pressure-temperature (P-T) phase diagram of Ti [117,118] demonstrates that (i) it undergoes through a martensitic transformation (MT) from high-temperature body-centered cubic (BCC or β) phase to hexagonal close-packed (HCP or α) phase at 1155 K temperature and ambient pressure, (ii) its α phase transforms under pressure into hexagonal open-packed (HOP or ω) phase, and (iii) its β phase also directly transforms into ω structure above a triple point. The MT in titanium is similar to that occuring in NiTi, a shape memory alloy. Despite this, any of the low-temperature structures of titanium do not exhibit the shape memory behavior like NiTi. This is because the nearest neighbor (NN) atoms have identical atomic arrangements, and have more than one way to transform from α to β structure at atomic level. Experimentally, α structure is the equilibrium

state of Ti [117,118] at room temperature and ambient pressure. Theoretical calculations indicate, instead, that ω is the ground state structure [119–123]. It is well known that a martensitic transformation is a non-diffusive first-order phase transformation involving atomic displacements and lattice distortion of the parent phase of a material. The MT in titanium has been investigated through experiments and theoretical [124–126] analysis over the years.

Studies of the transformation pathways connecting the three structures of Ti have shown that β to α transformation occurs via $\{0\bar{1}1\}<011>$ shuffle corresponding to softening of an acoustic phonon [127] at $q_M = \frac{\pi}{a}(011)$ wave-vector, known as the Burgers mechanism [128] of β to α transformation in Zirconium, and is similar to the B2 to B19 transformation in the shape memory alloys [79]. The β to ω transformation occurs via plane collapse along the [111] direction of the BCC structure corresponding to softening of a longitudinal acoustic phonon [129–131] at $q_\omega = \frac{2}{3}(111)$ wave-vector. Trinkle and co-workers [132] determined the path of α to ω transformation. Though soft phonons provide a piece of important information relevant to the transformation, contribution of strain is not quite clear yet, which is essential to the MT.

It is also not clear (i) how the strain-phonon coupling influences the MT as we have seen in MT in NiTi [45], and (ii) which order parameters govern this transformation in Ti. β and α structures and their transformation is relevant to many industrial applications of titanium alloys. For this, (i) alpha stabilizers are aluminum, oxygen, nitrogen or carbon whose addition to titanium raises the α to β transition temperature, and (ii) beta stabilizers are molybdenum, vanadium, tantalum, niobium or manganese whose addition lowers the α to β transition temperature. Therefore, our focus here is on the β to α transformation, particularly to develop a quantitatively accurate microscopic model and theory to determine how coupled phonons and strain constitute the mechanism of β to α phase transformation.

In this chapter, we present a thorough investigation of temperature-induced β to α phase transformation in titanium, based on effective Hamiltonian H_{eff} which is constructed from first-principles, and Landau theoretical analysis with focus on order parameters involved in this transformation. In Sec. 5.2, we present the computational details of first-principles methods, optimized structural parameters of different structures of Ti and their energies. In Sec. 5.3, we present phonon spectra of the conventional unit cell of β and α structures and discuss their lattice stability. In Sec. 5.4, we identify the order parameters that are relevant to β to α phase transformation. In Sec. 5.5, we present a detailed description of construction of effective Hamiltonian (H_{eff}) taking β as the reference structure to capture the low energy landscape of α structure of titanium. In Sec. 5.6, we present results of Monte Carlo simulations of H_{eff} using a Fortran code developed. In Sec. 5.7, we present Landau theoretical analysis to identify the specific strain-phonon couplings in H_{eff} that govern the β to α martensitic transformation in titanium, and then we will summarize our work in Sec. 5.8. Our work facilitates general understanding of β to α stabilizers in Ti alloys.

5.2 Computational methods and structural parameters

Our first-principles calculations are performed within the density functional theory (DFT) based on the plane-wave pseudopotential scheme implemented in the Quantum Espresso (QE) package [81], with a generalized gradient approximation (GGA) and PW91 [133] form of exchange-correlation energy functional. Results for properties of Ti are sensitive to energy cutoff on basis set and k-points, and hence we use a relatively high accuracy parameters in our calculations. We use energy

cutoffs of 50 Ry and 400 Ry to truncate plane-wave basis sets used for representing Kohn-Sham wave functions and charge density respectively. In self-consistent Kohn-Sham (KS) calculations, Brillouin zone integrations were sampled on uniform meshes of $24 \times 24 \times 24$ k-points for β, $24 \times 24 \times 18$ k-points for α and $24 \times 24 \times 36$ k-points for ω structures. We relaxed structures to minimize energy with respect to lattice parameters and atomic positions until the magnitude of stresses are less than 1 kbar and Hellmann-Feynman force on each atom is less than 1 meV/$\mathring{A}$. We reconfirm structural parameters and relative energies of the structures of Ti using calculations based on SCAN meta-GGA exchange-correlation functional [83, 84] as implemented in the VASP code [85,86] along with projector augmented wave (PAW) potentials [87]. Within the framework of DFPT, we determined dynamical matrices and phonons at q-points on a $6 \times 6 \times 6$ mesh for β, and $6 \times 6 \times 2$ mesh in the BZ for α structures. We performed first-principles calculations using different computations schemes and flavors of exchange-correlational functional and have optimized the structural parameters of all three Ti phases. Our estimates of structural parameters and energies of the β, α and ω structures of Ti agree well with earlier theoretical results [125], and reconfirm that ω is the ground stable structure of Ti at 0 K temperature and ambient pressure (Table 5.1). Our calculated lattice parameters of β, α and ω structures are also in good agreement with experiment [127, 134, 135].

5.3 Lattice stabilities of β and α structures: Phonon spectra

To assess the stability of β and α structures at low-T, we obtained phonon spectra of β (using conventional unit cell) and α structures within the framework of first-principles DFPT. We show that phonon-dispersion of β structure (Fig. 5.1a) in the conventional cubic unit cell has many unstable phonon branches throughout the BZ

Table 5.1: Structural parameters and energies of β, α and ω phases of Ti relative to α phase, obtained with different computational schemes of first-principles calculations.

Phase	Space group	Wyckoff positions	Method	a ($\AA$)	c/a	Volume($\AA^3$)	$E - E_\alpha$ (meV/atom)
β	$Im\bar{3}m$	$2a(0,0,0)$	GGA (PW91)	3.25		17.16	106.5
(BCC)			SCAN metaGGA	3.22		16.69	119.5
			GGA (PW91) [125]	3.26		17.32	108.0
			Exp [127]	3.31		18.13	
α	$P6_3/mmc$	$2c(1/3,2/3,1/4)$	GGA (PW91)	2.94	1.58	17.39	0
(HCP)			SCAN metaGGA	2.91	1.58	16.86	0
			GGA (PW91) [125]	2.95	1.58	17.56	0
			Exp [134]	2.95	1.59	17.68	
ω	$P6/mmm$	$1a(0,0,0)$	GGA (PW91)	4.57	0.62	17.08	-5.8
(Hexagonal)			SCAN metaGGA	4.45	0.62	16.64	-24.5
			GGA (PW91) [125]	4.59	0.62	17.31	-5.0
			Exp [135]	4.62	0.61	17.42	

making it unstable at low-T. Among them, the doubly degenerate $M_{5'}$ phonon at wave-vector M is the strongest instability ($\omega \sim 170i\ cm^{-1}$). Phonon dispersion of α structure (Fig. 5.1b) exhibits no instability anywhere in BZ, confirming that α structure is stable at low-T.

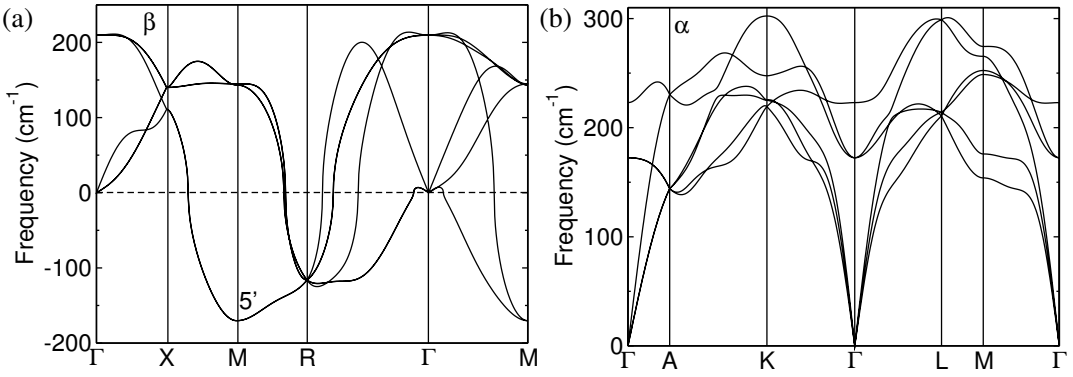

Figure 5.1: Phonon dispersion along high-symmetry lines of conventional unit cell of β (a) and α (b) structures of titanium obtained using DFPT simulations. Unstable modes with imaginary frequencies ($\omega^2 < 0$) are shown with negative values.

5.4 Identification of order parameters

Taking unit cell with two atoms basis of the β structure as a reference, we established a structural link between this and α structure of Ti by expressing their relative atomic positions and lattice distortions in terms of its phonon modes and strains of

β structure respectively. We find that the doubly degenerate unstable $M_{5'}$ phonon mode of β structure that dispalce alternating $\{0\bar{1}1\}$ planes opposite to each other in $< 011 >$ direction with Bain strain (s_2), hydrostatic strain (s_3) and pure shear (s_4) govern the β to α structural transformation (Fig. 5.2). The quantitative estimation of amplitudes of phonons and strains involved in β to α transformation are listed in Table 5.2. Clearly, four order parameters ($M_{5'}$, s_2, s_3 and s_4) are involved in the β to α transformation similar to those in B2 to B19 transformation in PtTi and NiTi.

Table 5.2: Order parameters (phonon modes at $\vec{q}_M = \frac{\pi}{a}(011)$ wave-vector of the conventional unit cell of β structure and strain) associated with β and α structures of Ti, obtained from first-principles calculations. The amplitude of phonon eigenmodes are in units of lattice constant of β structure. Phonon eigenmodes are in terms of atomic displacements $\hat{e}_{ph} = |\tau_x, \tau_y, \tau_z, \tau'_x, \tau'_y, \tau'_z >$ (τ_α and τ'_α are the displacemets of atoms at corner and center of unit cell respectively). The strain eigenmodes $s = |\varepsilon_1, \varepsilon_2, \varepsilon_3, \varepsilon_4, \varepsilon_5, \varepsilon_6 >$, here we have used the Voigt notations ($\varepsilon_1 = \varepsilon_{xx}$, $\varepsilon_2 = \varepsilon_{yy}$, $\varepsilon_3 = \varepsilon_{zz}$, $\varepsilon_4 = 2\varepsilon_{yz}$, $\varepsilon_5 = 2\varepsilon_{zx}$ and $\varepsilon_6 = 2\varepsilon_{xy}$).

Modes	Eigenmode	Character	β	α
$M_{5'}$	$\frac{1}{2}\|0,1,1,0,1,1>$	$\{0\bar{1}1\} < 011 >$ Basal shuffling	0	0.174
$M_{2'}$	$\|0,0,0,1,0,0>$	$\{0\bar{1}1\}$<100>, τ_z displacements	0	0
$M_{4'}$	$\|1,0,0,0,0,0>$	$\{0\bar{1}1\}$<100>, τ'_z displacements	0	0
s_1	$\frac{1}{\sqrt{2}}\|0,1,-1,0,0,0>$	$\{0\bar{1}1\}$<011> Basal shear	0	0
s_2	$\frac{1}{\sqrt{6}}\|-2,1,1,0,0,0>$	Bain strain	0	0.127
s_3	$\frac{1}{\sqrt{3}}\|1,1,1,0,0,0>$	Hydrostatic strain	0	0.009
s_4	$\|0,0,0,1,0,0>$	{010}<001> Pure shear	0	0.097
s_5	$\frac{1}{\sqrt{2}}\|0,0,0,0,1,1>$	{100}<011> Non-basal shear	0	0

5.5 Construction of effective Hamiltonian

Having identified the phonons and strains responsible for β to α phase transformation in Ti, we constructed an effective Hamiltonian (H_{eff}) following the scheme of lattice Wannier functions (LWFs) in Ref. [22] to model the low-energy landscape of

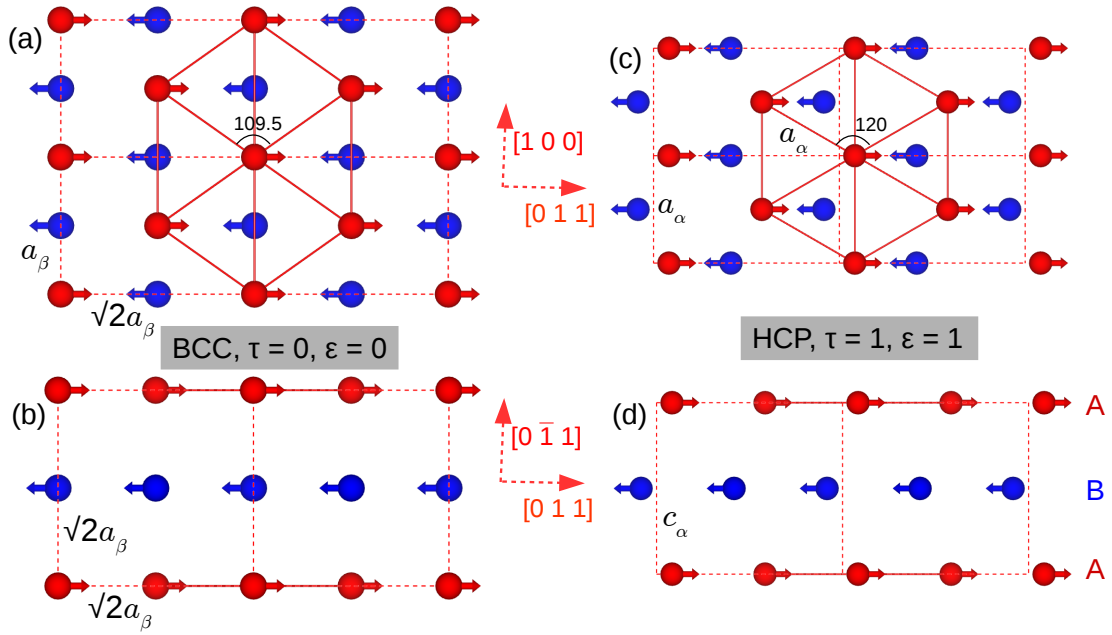

Figure 5.2: Cell-doubling phonon modes of the high symmetry β structure that constitute order parameters of $\beta \rightarrow \alpha$ structural transformations. Atomic displacements of $M_{5'}$ $(0\bar{1}1)$ view (a), (100) view (b) at $\vec{q} = \pi/a(011)$, shown in $1 \times \sqrt{2} \times \sqrt{2}$ supercell of conventional unit cell of β structure. While $M_{5'}$ phonon and hexagonal strain give α structure $(0\bar{1}1)$ view (c), (100) view (d). The planar unit at $c/2$ distance along $[0\ \bar{1}\ 1]$ direction contains Ti (blue).

Ti as function of these phonons and strains. In this process, we identify the symmetry invariant subspaces of phonons starting with the full phonon dispersion of the β structure obtained along the high symmetry lines ($\Gamma \rightarrow X \rightarrow M \rightarrow \Gamma \rightarrow R \rightarrow M$, see Fig. 5.1a) in the BZ of the cubic unit cell. Unlike in NiTi, where atoms at the corner and the center of the cubic unit cell are different and acoustic and optical phonons are separated by frequency gap, β structure has identical atoms at the corner and center of the conventional cubic unit cell, and hence no gap between acoustic and optical phonons, which are inseparable in its phonon dispersion (Fig 5.1a). In the conventional unit cell of β structure both corner and central atoms are identical and interchangeable, and hence their LWFs must have identical subspace. Therefore, we write H_{eff} of titanium in the subspace of atomic displacements instead of phonon modes, unlike effective Hamiltonian of NiTi. Using symmetries and eigenvectors of

the zone boundary phonons, we determine $\vec{\tau}$ and $\vec{\tau}'$ localized LWFs centered at corner and center of the conventional unit cell of β structure, respectively. Using the cubic symmetry of β structure, we express H_{eff} as a symmetry invariant Taylor expansion in $\vec{\tau}_i$, $\vec{\tau}'_i$ and homogeneous strains ($\varepsilon_{\alpha\beta}$), i indicating the unit cell. H_{eff} consists of three parts:

$$H_{eff}(\vec{\tau}_i, \vec{\tau}'_i, \varepsilon) = H_{ph}(\vec{\tau}_i, \vec{\tau}'_i) + H_{elastic}(\varepsilon_{\alpha\beta}) + H_{spc}(\vec{\tau}_i, \vec{\tau}'_i, \varepsilon_{\alpha\beta}) \tag{5.1}$$

where $H_{ph}(\vec{\tau}_i, \vec{\tau}'_i)$ operates in the subcpaces of Ti atomic displacements, $H_{elastic}(\varepsilon_{\alpha\beta})$ is linear and nonlinear elastic energy of homogeneous strains $\varepsilon_{\alpha\beta}$ and the coupling of $\varepsilon_{\alpha\beta}$ with set of LWFs is included in $H_{spc}(\vec{\tau}_i, \vec{\tau}'_i, \varepsilon_{\alpha\beta})$. α and β in $\varepsilon_{\alpha\beta}$ denote cartesian coordinates x, y and z.

5.5.1 Effective Hamiltonian of phonons: $H_{ph}(\vec{\tau}_i, \vec{\tau}'_i)$

$H_{ph}(\vec{\tau}_i, \vec{\tau}'_i)$ represents energetics of phonons and inhomogeneous strain, which include all the lattice instabilities of unstable modes (Fig. 5.1a) of the β structure of Ti, It includes harmonic and anharmonic terms, which relate to linear and nonlinear elastic energy terms in $H_{elastic}$ in the long-wavelength limit. This part of effective Hamiltonian is invariant under translational and rotational symmetries. To impose translational symmetry, we express energy terms using differences in LWFs ($\vec{\tau}_i$ and $\vec{\tau}'_i$) at neighboring sites and their dot products.

In the harmonic part of $H_{ph}(\vec{\tau}_i, \vec{\tau}'_i)$, we consider differences between $\vec{\tau}_i$'s in $H^1_{har}(\vec{\tau})$ and $\vec{\tau}'_i$'s in $H^2_{har}(\vec{\tau}')$ up to third NN sites, and their interactions in $H^3_{har}(\vec{\tau}, \vec{\tau}')$ with a general form permitted by the symmetry of space group $Pm\bar{3}m$ as,

$$
\begin{aligned}
H^1_{har}(\vec{\tau}) &= \frac{1}{2}\sum_{i=1}^{N}[\sum_{j=1}^{6}\{A_{11}|\vec{\tau}_{1ij}|^2 + A_{12}(\vec{\tau}_{1ij}\cdot\hat{d}_{1j})^2\} \\
&+ \sum_{j=1}^{12}\{A_{21}(\vec{\tau}_{2ij}\cdot\hat{d}_{2j})^2 + A_{22}(\vec{\tau}_{2ij}\cdot\hat{d}_{21j})^2 + A_{23}(\vec{\tau}_{2ij}\cdot\hat{d}_{22j})^2\} \\
&+ \sum_{j=1}^{8}\{A_{31}|\vec{\tau}_{3ij}|^2 + A_{32}(\vec{\tau}_{3ij}\cdot\hat{d}_{3j})^2\}], \qquad (5.2)
\end{aligned}
$$

$$
\begin{aligned}
H^2_{har}(\vec{\tau}') &= \frac{1}{2}\sum_{i=1}^{N}[\sum_{j=1}^{6}\{A_{11}|\vec{\tau}'_{1ij}|^2 + A_{12}(\vec{\tau}'_{1ij}\cdot\hat{d}_{1j})^2\} \\
&+ \sum_{j=1}^{12}\{A_{21}(\vec{\tau}'_{2ij}\cdot\hat{d}_{2j})^2 + A_{22}(\vec{\tau}'_{2ij}\cdot\hat{d}_{21j})^2 + A_{23}(\vec{\tau}'_{2ij}\cdot\hat{d}_{22j})^2\} \\
&+ \sum_{j=1}^{8}\{A_{31}|\vec{\tau}'_{3ij}|^2 + A_{32}(\vec{\tau}'_{3ij}\cdot\hat{d}_{3j})^2\}], \qquad (5.3)
\end{aligned}
$$

$$
H^3_{har}(\vec{\tau},\vec{\tau}') = \sum_{i=1}^{N}\sum_{j=1}^{8}\{A_{01}|\vec{\tau}_{0ij}|^2 + A_{02}(\tau_{0ijx}\tau_{0ijy}d_{0jx}d_{0jy} + c.p)\}], \qquad (5.4)
$$

where $\vec{\tau}_{1ij}$, $\vec{\tau}_{2ij}$, $\vec{\tau}_{3ij}$ ($\vec{\tau}'_{1ij}$, $\vec{\tau}'_{2ij}$, $\vec{\tau}'_{3ij}$) denote the LWFs differences between $\vec{\tau}_i$ ($\vec{\tau}'_i$) at site i and its $\vec{\tau}_j$ ($\vec{\tau}'_j$) at first, second and third NNs at site j respectively. Whereas, $\vec{\tau}_{0ij}$ shows the difference between $\vec{\tau}_i$ and its first NNs $\vec{\tau}'_j$. $\hat{d}_{1j}$, $\hat{d}_{2j}$,$\hat{d}_{3j}$ denote unit vectors along the directions to first, second and third NN sites j respectively. $\hat{d}_{21j}$ and $\hat{d}_{22j}$ are unit vectors perpendicular to $\hat{d}_{2j}$. $\hat{d}_{0j}$ shows unit vector along the direction of first NN $\vec{\tau}'_j$ of $\vec{\tau}_i$. A_{ij}'s are the harmonic coefficients and determined from force constants of phonons at high symmetry q-points (Γ, X, M and R) and $\vec{q}_\lambda = \frac{\pi}{3a}(1,1,1)$. Linear combinations of these coefficients give the corresponding eigenvalues of phonons.

Since we have eight equations (Table 5.3) and nine coefficients, we use singular value decomposition (SVD) to determine these coefficients, and have listed them in Table 5.6.

Table 5.3: Linear combinations of coefficients in the harmonic part of H_{eff} at a q wave-vector give the eigenvalue of corresponding phonon. $M^a_{5'}$ and $M^o_{5'}$ are doubly degenerate unstable acoustic and stable optical phonon modes respectively.

Phonon modes	Linear combination of the coefficients	Eigenvalue of phonon modes (eV/f.u)
Γ_{15}	$8A_{01}$	44.1
X_1	$4A_{01}+2A_{11}+2A_{12}+4A_{21}+4A_{22}+8A_{31}+\frac{8}{3}A_{32}$	11.5
X_5	$4A_{01}+2A_{11}+2A_{21}+2A_{22}+4A_{23}+8A_{31}+\frac{8}{3}A_{32}$	18.2
$M_{2'}$	$4A_{01}+4A_{11}+4A_{21}+4A_{22}$	22.4
$M^a_{5'}$	$4A_{01}-\frac{2}{3}A_{02}+4A_{11}+2A_{12}+2A_{21}+2A_{22}+4A_{23}$	-21.0
$M^o_{5'}$	$4A_{01}+\frac{2}{3}A_{02}+4A_{11}+2A_{12}+2A_{21}+2A_{22}+4A_{23}$	19.1
$R_{25'}$	$4A_{01}+6A_{11}+2A_{12}+8A_{31}+\frac{8}{3}A_{32}$	-11.0
λ_1	$2.25A_{01}-0.252A_{02}+2.25A_{11}+0.75A_{12}+1.5A_{21}+0.75A_{23}+2.25A_{31}+0.25A_{32}$	-3.8

In the anharmonic part of $H_{ph}(\vec{\tau}_i,\vec{\tau}'_i)$, we consider interaction between $\vec{\tau}_i$'s in $H^1_{anh}(\vec{\tau})$ and $\vec{\tau}'_i$'s in $H^2_{anh}(\vec{\tau}')$, both being identical and interchangeable. In the third-order terms, we include interaction up to the second NNs that are needed to include inhomogeneous strain in the long-wavelength limit. Due to cubic symmetry, odd-order terms do not contribute to the energy of phonons at high-symmetry q-point but do contribute in the long-wavelength limit. We approximated interaction in the third-order terms by considering the dominant term in interaction with NN sites allowed by the cubic symmetry. Fourth-order terms include the cubic anisotropy, while sixth- and eighth-order terms are simplified by restricting to isotropic terms in differences between $\vec{\tau}_i$'s ($\vec{\tau}'_i$) up to first NNs.

$$\begin{aligned} H^1_{anh}(\vec{\tau}) &= \sum_{i=1}^{N}[\sum_{j=1}^{6} B_{31}(\vec{\tau}_{1ij}\cdot\hat{d}_{1j})^3+\sum_{j=1}^{12} B_{32}(\vec{\tau}_{2ij}\cdot\hat{d}_{2j})^3 \\ &+ \sum_{j=1}^{6}\{B_{41}|\vec{\tau}_{1ij}|^4+B_{42}(\tau^2_{1ijx}\tau^2_{1ijy}+\tau^2_{1ijy}\tau^2_{1ijz}+\tau^2_{1ijz}\tau^2_{1ijx}) \\ &+ B_{61}|\vec{\tau}_{1ij}|^6+B_{81}|\vec{\tau}_{1ij}|^8\}], \end{aligned} \tag{5.5}$$

$$
\begin{aligned}
H^2_{anh}(\vec{\tau}') &= \sum_{i=1}^{N}[\sum_{j=1}^{6} B_{31}(\vec{\tau}'_{1ij}\cdot\hat{d}_{1j})^3 + \sum_{j=1}^{12} B_{32}(\vec{\tau}'_{2ij}\cdot\hat{d}_{2j})^3 \\
&+ \sum_{j=1}^{6}\{B_{41}|\vec{\tau}'_{1ij}|^4 + B_{42}(\tau'^2_{1ijx}\tau'^2_{1ijy} + \tau'^2_{1ijy}\tau'^2_{1ijz} + \tau'^2_{1ijz}\tau'^2_{1ijx}) \\
&+ B_{61}|\vec{\tau}'_{1ij}|^6 + B_{81}|\vec{\tau}'_{1ij}|^8\}], \qquad (5.6)
\end{aligned}
$$

where B_{ij}'s are coefficients of anharmonic terms. Third-order coefficients (B_{31} and B_{32}) are related to the nonlinear elastic moduli, and are obtained from the corresponding third-order elastic moduli. Since there are only two coefficients, we use two inequivalent strain modes (uniaxial strain and Bain strain) to calculate these coefficients (Table 3.4). The two fourth-order coefficients are determined from energies of structure obtained by freezing doubly degenerate unstable $M_{5'}$ (Table 3.5). We fitted the energy of these configurations of structural distortions to these phonon modes using a polynomial of 8^{th} order. To determine the coefficients of sixth- and eight-order terms, ($32B_{61} = -3.98 \times 10^4$ eV/f.u) and ($64B_{81} = 4.51 \times 10^5$ eV/f.u), we fit the polynomial to double-well energy of $M_{5'}$ mode (Fig. 5.3).

Table 5.4: Strain mode is represented with $s = |\varepsilon_1, \varepsilon_2, \varepsilon_3, \varepsilon_4, \varepsilon_5, \varepsilon_6 >$, in the Voigt notation. Uniaxial and Bain strain modes are represented by $s_{uniax} = \varepsilon|1, 0, 0, 0, 0, 0 >$ and $s_{Bain} = \varepsilon|-2, 1, 1, 0, 0, 0 >$ respectively. Coefficients of the 3^{rd} order terms are linear combinations of the 3^{rd} order elastic moduli.

Strain mode	Linear combination of 3^{rd} order coefficients	Linear combination of 3^{rd} order elastic moduli
s_{uniax}	$2B_{31} + 2.82B_{32}$	$\frac{1}{6}C_{111} = -23.0$
s_{Bain}	$-12B_{31} + 8.49B_{32}$	$-C_{111} + 3C_{112} - 2C_{123} = 40.9$

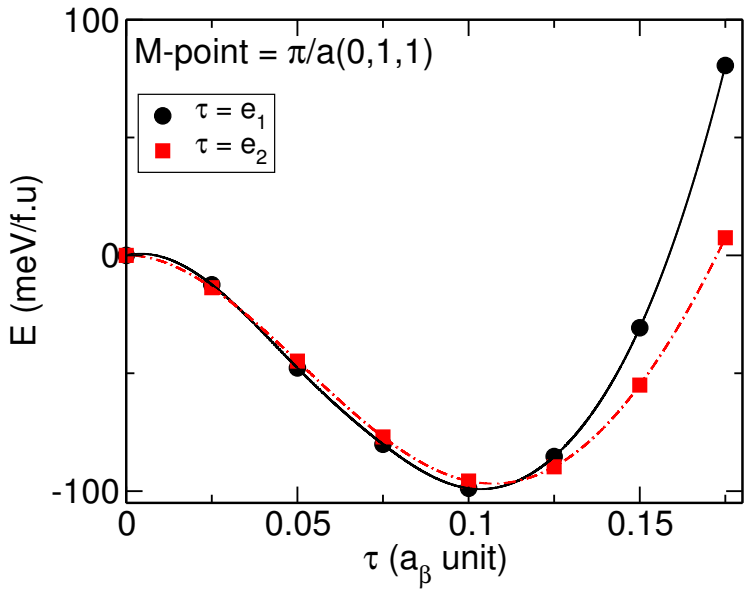

Figure 5.3: Energies of cell-doubling structural distortions (τ at $\vec{q} = \frac{\pi}{a}(0,1,1)$), $e_1 = \frac{1}{\sqrt{2}}|0,1,0,0,0,1>$ and $e_2 = \frac{1}{2}|0,1,1,0,1,1>$ are the phonon eigenvectors of doubly degenerate unstable $M_{5'}$ phonon modes and their linear combination, respectively. Lines represent the fits obtained with the 4^{th}, 6^{th} and 8^{th} anharmonic parameters in H_{eff}.

Table 5.5: The amplitudes of phonon modes at M-point ($\frac{\pi}{a}(011)$) are in unit of lattice constant of β structure, and their eigenvectors are expressed in terms of atomic displacements $\hat{e} = |\tau_x, \tau_y, \tau_z, \tau'_x, \tau'_y, \tau'_z>$. $\hat{e}_1^M$ and $\hat{e}_2^M$ are the eigenvectors of unstable $M_{5'}$ mode and linear combination of its degenerate mode, respectively.

Mode	Linear combination of 4^{th} order coefficients	4^{th} order fitting coefficients in in polynomial (eV/f.u)
$\hat{e}_1^M = \frac{1}{\sqrt{2}}\|0,1,0,0,0,1>$	$16B_{41}$	468.68
$\hat{e}_2^M = \frac{1}{2}\|0,1,1,0,1,1>$	$16B_{41} + 4B_{42}$	999.11

Table 5.6: Coefficients of harmonic and anharmonic terms in effective Hamiltonian in unit of eV/f.u.

Coeff.	Values	Coeff.	Values	Coeff.	Values
A_{01}	5.5	A_{22}	0.4	B_{41}	127.1
A_{02}	30.1	A_{23}	-0.6	B_{42}	-135.2
A_{11}	-2.8	A_{31}	0.1	B_{61}	-1244.0
A_{12}	-7.5	A_{32}	-0.7	B_{81}	7041.9
A_{21}	2.5	B_{31}	-5.5		

5.5.2 Hamiltonian of homogeneous strain

In a martensitic β to α transformation a large lattice deformation occurs hinting the importance of elastic energy of homogeneous strain, and we find that the 2^{nd}

order elastic constant C' (See Table 5.8) of axial strains is unstable. Therefore, in the homogeneous strain Hamiltonian we consider non-linear elasticity up to fourth-order in axial strains allowed by the cubic symmetry. For shear strain, second-order terms are found to be sufficient to capture elastic energy landscape.

$$\begin{aligned} H_s\{\varepsilon\} &= \frac{N}{2}\{C_{11}(\varepsilon_1^2+\varepsilon_2^2+\varepsilon_3^2)+2C_{12}(\varepsilon_1\varepsilon_2+\varepsilon_2\varepsilon_3+\varepsilon_3\varepsilon_1)+C_{44}(\varepsilon_4^2+\varepsilon_5^2+\varepsilon_6^2)\} \\ &+ \frac{N}{6}\{C_{111}(\varepsilon_1^3+\varepsilon_2^3+\varepsilon_3^3)+3C_{112}(\varepsilon_1^2(\varepsilon_2+\varepsilon_3)+\varepsilon_2^2(\varepsilon_3+\varepsilon_1)+\varepsilon_3^2(\varepsilon_1+\varepsilon_2)) \\ &+ 6C_{123}\varepsilon_1\varepsilon_2\varepsilon_3\} \\ &+ \frac{N}{24}\{C_{1111}(\varepsilon_1^4+\varepsilon_2^4+\varepsilon_3^4)+4C_{1112}(\varepsilon_1^3(\varepsilon_2+\varepsilon_3)+\varepsilon_2^3(\varepsilon_3+\varepsilon_1)+\varepsilon_3^3(\varepsilon_1+\varepsilon_2)) \\ &+ 6C_{1122}(\varepsilon_1^2\varepsilon_2^2+\varepsilon_2^2\varepsilon_3^2+\varepsilon_3^2\varepsilon_1^2)+12C_{1123}\varepsilon_1\varepsilon_2\varepsilon_3(\varepsilon_1+\varepsilon_2+\varepsilon_3)\} \end{aligned} \tag{5.7}$$

where N is the number of unit cells, C_{ij}, C_{ijk} and C_{ijkl} are second-, third- and fourth-order elastic moduli. To calculate elastic moduli, we fit the energy of structures distorted along with different strain modes to fourth-order polynomial in ε, and linear combinations of second-, third- and fourth-order elastic moduli give second-, third- and fourth-order coefficient of the polynomial respectively (Table 5.7). Our estimates of these compliances are listed in Table 5.8.

Table 5.7: In each type of strain modes $s(\varepsilon) = |\varepsilon_1, \varepsilon_2, \varepsilon_3, \varepsilon_4, \varepsilon_5, \varepsilon_6 >$, the total energy is expressed as a polynomial function of ε. The linear combinations of second, third and forth order elastic moduli are equal to the values of second-, third- and forth-order coefficients of polynomial fit to the data.

Strain mode	Linear combination of C_{ij}	Linear combination of C_{ijk}	Linear combination of C_{ijkl}
$s_a = \varepsilon\|1,0,0,0,0,0>$	$\frac{1}{2}C_{11}$	$\frac{1}{6}C_{111}$	$\frac{1}{24}C_{1111}$
$s_b = \varepsilon\|1,1,0,0,0,0>$	$C_{11}+C_{12}$	$\frac{1}{3}C_{111}+C_{112}$	$\frac{1}{16}C_{1111}+\frac{1}{3}C_{1112}+\frac{1}{4}C_{1122}$
$s_c = \varepsilon\|1,-1,0,0,0,0>$	$C_{11}-C_{12}$	0	$\frac{1}{16}C_{1111}-\frac{1}{3}C_{1112}+\frac{1}{4}C_{1122}$
$s_d = \varepsilon\|1,1,1,0,0,0>$	$\frac{3}{2}C_{11}+3C_{12}$	$\frac{1}{2}C_{111}+3C_{112}+C_{123}$	$\frac{1}{8}C_{1111}+C_{1112}+\frac{1}{4}C_{1122}+\frac{3}{2}C_{1123}$
$s_e = \varepsilon\|0,0,0,1,1,1>$	$\frac{3}{2}C_{44}$		

Table 5.8: Elastic moludi of $H_{elastic}(\varepsilon)$ in GPa, determined from first-principles.

Coeff.	Values	Coeff.	Values	Coeff.	Values
C_{11}	117	C_{111}	-817	C_{1112}	400
C_{12}	157	C_{112}	-517	C_{1122}	6161
C'	-20	C_{123}	-487	C_{1123}	-1164
C_{44}	57	C_{1111}	5831		

5.5.3 Coupling between homogeneous strain and phonons

Coupling of homogeneous strain with phonons is important in MTs where atomic displacements occur along with lattice deformations, and plays a crucial role. We include third-order couplings between homogeneous strains (i) quadratic terms of $\vec{\tau}_i$'s ($\vec{\tau}'_i$'s) in H^1_{spc} (H^2_{spc}) taking differences between $\vec{\tau}_i$ ($\vec{\tau}'_i$) at site i and $\vec{\tau}_j$ ($\vec{\tau}'_j$) at its first and second NN sites j (Eq. 5.8 and 5.9), and (ii) with products of τ_i and τ'_i in H^3_{spc} (Eq. 5.10). To make sure that H_{eff} gives the lowest energy phase α, it is necessury to take interactions upto the second NNs sites at third-order. However, we find that only third-order strain-phonon coupling is not sufficient to capture the details of α phase, and hence include fourth-order couplings between strain and τ_i (τ'_i) and given in H^4_{spc} (H^5_{spc}) (Eq. 5.11 and 5.12).

$$
\begin{aligned}
H^1_{spc}(\vec{\tau},\varepsilon) &= \sum_{i=1}^{N}[\sum_{j=1}^{6}\{g_{30}(\varepsilon_1+\varepsilon_2+\varepsilon_3)|\vec{\tau}_{1ij}|^2 \\
&+ g_{31}(\varepsilon_1\tau^2_{1ijx}+\varepsilon_2\tau^2_{1ijy}+\varepsilon_3\tau^2_{1ijz}) \\
&+ g_{32}(\varepsilon_1+\varepsilon_2+\varepsilon_3)(\vec{\tau}_{1ij}\cdot\hat{d}_{1j})^2 \\
&+ g_{33}(\varepsilon_1\tau^2_{1ijx}d^2_{1jx}+\varepsilon_2\tau^2_{1ijy}d^2_{1jy}+\varepsilon_3\tau^2_{1ijz}d^2_{1jz}) \\
&+ g_{34}(\varepsilon_1(\tau^2_{1ijy}+\tau^2_{1ijz})d^2_{1jx}+\varepsilon_2(\tau^2_{1ijz}+\tau^2_{1ijx})d^2_{1jy}+\varepsilon_3(\tau^2_{1ijx}+\tau^2_{1ijy})d^2_{1jz}) \\
&+ g_{35}(\varepsilon_4\tau_{1ijy}\tau_{1ijz}+\varepsilon_5\tau_{1ijz}\tau_{1ijx}+\varepsilon_6\tau_{1ijx}\tau_{1ijy}) \\
&+ g_{36}(\varepsilon_4\tau_{1ijy}\tau_{1ijz}d^2_{1jx}+\varepsilon_5\tau_{1ijz}\tau_{1ijx}d^2_{1jy}+\varepsilon_6\tau_{1ijx}\tau_{1ijy}d^2_{1jz}) \\
&+ \sum_{j=1}^{12}\{g_{37}(\varepsilon_1+\varepsilon_2+\varepsilon_3)|\vec{\tau}_{2ij}|^2 \\
&+ g_{38}(\varepsilon_1\tau^2_{2ijx}+\varepsilon_2\tau^2_{2ijy}+\varepsilon_3\tau^2_{2ijz}) \\
&+ g_{39}(\varepsilon_4\tau_{2ijy}\tau_{2ijz}+\varepsilon_5\tau_{2ijz}\tau_{2ijx}+\varepsilon_6\tau_{2ijx}\tau_{2ijy})\}], \qquad (5.8)
\end{aligned}
$$

$$
\begin{aligned}
H^2_{spc}(\vec{\tau}',\varepsilon) &= \sum_{i=1}^{N}[\sum_{j=1}^{6}\{g_{30}(\varepsilon_1+\varepsilon_2+\varepsilon_3)|\vec{\tau}'_{1ij}|^2 \\
&+ g_{31}(\varepsilon_1\tau'^2_{1ijx}+\varepsilon_2\tau'^2_{1ijy}+\varepsilon_3\tau'^2_{1ijz}) \\
&+ g_{32}(\varepsilon_1+\varepsilon_2+\varepsilon_3)(\vec{\tau}'_{1ij}\cdot\hat{d}_{1j})^2 \\
&+ g_{33}(\varepsilon_1\tau'^2_{1ijx}d^2_{1jx}+\varepsilon_2\tau'^2_{1ijy}d^2_{1jy}+\varepsilon_3\tau'^2_{1ijz}d^2_{1jz}) \\
&+ g_{34}(\varepsilon_1(\tau'^2_{1ijy}+\tau'^2_{1ijz})d^2_{1jx}+\varepsilon_2(\tau'^2_{1ijz}+\tau'^2_{1ijx})d^2_{1jy}+\varepsilon_3(\tau'^2_{1ijx}+\tau'^2_{1ijy})d^2_{1jz}) \\
&+ g_{35}(\varepsilon_4\tau'_{1ijy}\tau'_{1ijz}+\varepsilon_5\tau'_{1ijz}\tau'_{1ijx}+\varepsilon_6\tau'_{1ijx}\tau'_{1ijy}) \\
&+ g_{36}(\varepsilon_4\tau'_{1ijy}\tau'_{1ijz}d^2_{1jx}+\varepsilon_5\tau'_{1ijz}\tau'_{1ijx}d^2_{1jy}+\varepsilon_6\tau'_{1ijx}\tau'_{1ijy}d^2_{1jz}) \\
&+ \sum_{j=1}^{12}\{g_{37}(\varepsilon_1+\varepsilon_2+\varepsilon_3)|\vec{\tau}'_{2ij}|^2 \\
&+ g_{38}(\varepsilon_1\tau'^2_{2ijx}+\varepsilon_2\tau'^2_{2ijy}+\varepsilon_3\tau'^2_{2ijz}) \\
&+ g_{39}(\varepsilon_4\tau'_{2ijy}\tau'_{2ijz}+\varepsilon_5\tau'_{2ijz}\tau'_{2ijx}+\varepsilon_6\tau'_{2ijx}\tau'_{2ijy})\}], \qquad (5.9)
\end{aligned}
$$

$$
\begin{aligned}
H^3_{spc}(\vec{\tau},\vec{\tau}',\varepsilon) &= \sum_{i=1}^{N}\sum_{j=1}^{8}[h_{30}(\varepsilon_1+\varepsilon_2+\varepsilon_3)\{\tau_{0ijx}\tau_{0ijy}d_{0jx}d_{0jy}+c.p\} \\
&+ h_{31}\{\varepsilon_1\tau_{0ijy}\tau_{0ijz}d_{0jy}d_{0jz}+c.p\} \\
&+ h_{32}\{\varepsilon_4\tau^2_{0ijx}d_{0jy}d_{0jz}+c.p\} \\
&+ h_{33}\{\varepsilon_4(\tau^2_{0ijy}+\tau^2_{0ijz})d_{0jy}d_{0jz}+c.p\} \\
&+ h_{34}\{\tau_{0ijx}(\varepsilon_5\tau_{0ijz}+\varepsilon_6\tau_{0ijy})d_{0jy}d_{0jz}+c.p\}] \qquad (5.10)
\end{aligned}
$$

$$
\begin{aligned}
H^4_{spc}(\vec{\tau},\varepsilon) &= \sum_{i=1}^{N}\sum_{j=1}^{8}\{g_{40}(\varepsilon_1^2+\varepsilon_2^2+\varepsilon_3^2)|\vec{\tau}_{1ij}|^2 \\
&+ g_{41}(\varepsilon_1^2\tau_{1ijx}^2+\varepsilon_2^2\tau_{1ijy}^2+\varepsilon_3^2\tau_{1ijz}^2) \\
&+ g_{42}(\varepsilon_1\varepsilon_2\tau_{1ijz}^2+\varepsilon_2\varepsilon_3\tau_{1ijx}^2+\varepsilon_3\varepsilon_1\tau_{1ijy}^2) \\
&+ g_{43}(\varepsilon_1(\varepsilon_2+\varepsilon_3)\tau_{1ijx}^2+\varepsilon_2(\varepsilon_3+\varepsilon_1)\tau_{1ijy}^2+\varepsilon_3(\varepsilon_1+\varepsilon_2)\tau_{1ijz}^2) \\
&+ g_{44}(\varepsilon_4^2(\tau_{0ijy}^2+\tau_{0ijz}^2)+\varepsilon_5^2(\tau_{0ijz}^2+\tau_{0ijx}^2)+\varepsilon_6^2(\tau_{0ijx}^2+\tau_{0ijy}^2))\},
\end{aligned}
\tag{5.11}
$$

$$
\begin{aligned}
H^5_{spc}(\vec{\tau}',\varepsilon) &= \sum_{i=1}^{N}\sum_{j=1}^{8}\{g_{40}(\varepsilon_1^2+\varepsilon_2^2+\varepsilon_3^2)|\vec{\tau}'_{1ij}|^2 \\
&+ g_{41}(\varepsilon_1^2\tau_{1ijx}'^2+\varepsilon_2^2\tau_{1ijy}'^2+\varepsilon_3^2\tau_{1ijz}'^2) \\
&+ g_{42}(\varepsilon_1\varepsilon_2\tau_{1ijz}'^2+\varepsilon_2\varepsilon_3\tau_{1ijx}'^2+\varepsilon_3\varepsilon_1\tau_{1ijy}'^2) \\
&+ g_{43}(\varepsilon_1(\varepsilon_2+\varepsilon_3)\tau_{1ijx}'^2+\varepsilon_2(\varepsilon_3+\varepsilon_1)\tau_{1ijy}'^2+\varepsilon_3(\varepsilon_1+\varepsilon_2)\tau_{1ijz}'^2) \\
&+ g_{44}(\varepsilon_4^2(\tau_{0ijy}'^2+\tau_{0ijz}'^2)+\varepsilon_5^2(\tau_{0ijz}'^2+\tau_{0ijx}'^2)+\varepsilon_6^2(\tau_{0ijx}'^2+\tau_{0ijy}'^2))\},
\end{aligned}
\tag{5.12}
$$

where g_{ij}'s denote couplings of strain with τ_i and τ_i', individually, and h_{ij}'s are the third-order couplings that cause strain-induced mixing between τ_i and τ_i' LWFs. These coefficients were determined from calculations of structures obtained by freezing M-point and R-point phonon modes at the different values of strain. Values of the third- and fourth-order coupling coefficients are determined as first and second derivatives of harmonic coefficients with respect to strain respectively (Table 5.9), and listed in Table 5.10.

Our H_{eff} reproduces the lattice parameters and energies of β and α structures with negligible errors relative to the DFT results (Table 5.11).

Table 5.9: At each type of strain modes $s(\varepsilon) = |\varepsilon_1, \varepsilon_2, \varepsilon_3, \varepsilon_4, \varepsilon_5, \varepsilon_6 >$, value of third order strain phonon coupling coefficients are obtained as first derivatives of harmonic force constants at different phonon modes ($\hat{e}(\tau) = |\tau_x, \tau_y, \tau_z, \tau'_x, \tau'_y, \tau'_z >$) of M-point and R-point wave-vector. Fourth order strain phonon coupling are obtained as second derivative of harmonic force constants of unstable $M_{5'}$ phonon mode ($\hat{e}_2^M = \frac{\tau}{2}|0,1,1,0,1,1>$).

Strain mode	Phonon mode at M-point($\frac{\pi}{a}$(011)	Linear combination of the coefficients	1^{st} derivative of eigenvalue (eV/f.u)
$s_a = \varepsilon\|1,0,0,0,0,0>$	$\hat{e}_1^M = \tau\|1,0,0,0,0,0>$	$8g_{30} + 8g_{31} + 16g_{37} + 16g_{38}$	82.0
$s_b = \varepsilon\|0,1,1,0,0,0>$	$\hat{e}_1^M = \tau\|1,0,0,0,0,0>$	$16g_{30} + 8g_{34} + 32g_{37}$	-53.7
$s_a = \varepsilon\|1,0,0,0,0,0>$	$\hat{e}_2^M = \frac{\tau}{2}\|0,1,1,0,1,1>$	$-\frac{4}{3}h_{30} - \frac{4}{3}h_{31} + 8g_{30} + 4g_{32} + 16g_{37}$	28.7
$s_a = \varepsilon\|1,0,0,0,0,0>$	$\hat{e}_3^M = \frac{\tau}{2}\|0,1,1,0,\bar{1},\bar{1}>$	$\frac{4}{3}h_{30} + \frac{4}{3}h_{31} + 8g_{30} + 4g_{32} + 16g_{37}$	-128.9
$s_a = \varepsilon\|1,0,0,0,0,0>$	$\hat{e}_4^M = \frac{\tau}{\sqrt{2}}\|0,1,0,0,0,1>$	$8g_{30} + 4g_{32} + 4g_{34} + 16g_{37}$	-75.0
$s_c = \varepsilon\|1,1,0,0,0,0>$	$\hat{e}_2^M = \frac{\tau}{2}\|0,1,1,0,1,1>$	$-\frac{8}{3}h_{30} + 16g_{30} + 8g_{31} + 8g_{32} + 4g_{33}$ $+4g_{34} + 32g_{37} + 16g_{38}$	-99.0
$s_c = \varepsilon\|1,1,0,0,0,1>$	$\hat{e}_3^M = \frac{\tau}{2}\|0,1,1,0,\bar{1},\bar{1}>$	$\frac{8}{3}h_{30} + 16g_{30} + 8g_{31} + 8g_{32} + 4g_{33}$ $+4g_{34} + 32g_{37} + 16g_{38}$	-119.5
$s_d = \varepsilon\|0,0,0,1,0,0>$	$\hat{e}_5^M = \frac{\tau}{\sqrt{2}}\|1,0,0,1,0,0>$	$-\frac{16}{3}h_{32}$	10.2
$s_d = \varepsilon\|0,0,0,1,0,0>$	$\hat{e}_2^M = \frac{\tau}{2}\|0,1,1,0,1,1>$	$-\frac{8}{3}h_{33} + 4g_{35} + 8g_{39}$	-50.9
$s_d = \varepsilon\|0,0,0,1,0,0>$	$\hat{e}_3^M = \frac{\tau}{2}\|0,1,1,0,\bar{1},\bar{1}>$	$\frac{8}{3}h_{33} + 4g_{35} + 8g_{39}$	-105.3
$s_e = \varepsilon\|0,0,0,0,1,0>$	$\hat{e}_6^M = \frac{\tau}{2}\|\sqrt{2},\bar{1},0,0,0,1>$	$-0.94h_{34} - 2.83g_{35} - 1.41g_{36} - 5.66g_{39}$	35.0
$s_e = \varepsilon\|0,0,0,0,1,0>$	$\hat{e}_7^M = \frac{\tau}{2}\|0,1,0,\sqrt{2},0,1>$	$-0.94h_{34} + 2.83g_{35} + 1.41g_{36} + 5.66g_{39}$	-21.5
$s_a = \varepsilon\|1,0,0,0,0,0>$	$\hat{e}_1^R = \tau\|1,0,0,0,0,0>$	$12g_{30} + 12g_{31} + 4g_{32} + 4g_{33}$	-129.1
$s_f = \varepsilon\|1,1,1,0,0,0>$	$\hat{e}_1^R = \tau\|1,0,0,0,0,0>$	$36g_{30} + 12g_{31} + 12g_{32} + 4g_{33} + 8g_{34}$	-177.4
$s_g = \varepsilon\|0,0,0,1,1,1>$	$\hat{e}_2^R = \frac{\tau}{\sqrt{3}}\|1,1,1,0,0,0>$	$12g_{35} + 4g_{36}$	-100.2
Strain mode	Phonon mode at M-point($\frac{\pi}{a}$(011)	Linear combination of the coefficients	2^{nd} derivative of eigenvalue (eV/f.u)
$s_a = \varepsilon\|1,0,0,0,0,0>$	$\hat{e}_2^M = \frac{\tau}{2}\|0,1,1,0,1,1>$	$8g_{40}$	61.4
$s_h = \varepsilon\|0,1,0,0,0,0>$	$\hat{e}_2^M = \frac{\tau}{2}\|0,1,1,0,1,1>$	$8g_{40} + 4g_{41}$	481.9
$s_b = \varepsilon\|0,1,1,0,0,0>$	$\hat{e}_2^M = \frac{\tau}{2}\|0,1,1,0,1,1>$	$16g_{40} + 8g_{41} + 8g_{43}$	451.1
$s_f = \varepsilon\|1,1,1,0,0,0>$	$\hat{e}_2^M = \frac{\tau}{2}\|0,1,1,0,1,1>$	$24g_{40} + 8g_{41} + 8g_{42} + 16g_{43}$	345.4
$s_e = \varepsilon\|0,0,0,0,1,0>$	$\hat{e}_2^M = \frac{\tau}{2}\|0,1,1,0,1,1>$	$8g_{44}$	86.1

Table 5.10: Coefficients of coupling between strain and atomic displacements part of effective Hamiltonian in unit of eV/f.u..

Coeff.	Values	Coeff.	Values	Coeff.	Values
g_{30}	4.1	g_{37}	-2.2	g_{44}	10.8
g_{31}	-5.1	g_{38}	7.8	h_{30}	-3.9
g_{32}	-12.0	g_{39}	-2.4	h_{31}	-55.3
g_{33}	-17.0	g_{40}	20.2	h_{32}	-1.9
g_{34}	-6.2	g_{41}	80.1	h_{33}	-10.2
g_{35}	-14.7	g_{42}	30.7	h_{34}	-7.2
g_{36}	19.1	g_{43}	-64.1		

Table 5.11: Structural parameters and energies of β and α phases relative to α, obtained using DFT and effevtive Hamiltonian.

Phase	Method	a($\mathring{A}$)	c/a	Volume ($\mathring{A}^3$)	$E - E_\alpha$(meV/atom)
β	PW91	3.25		17.16	106
	H_{eff}	3.25		17.16	116
α	PW91	2.94	1.58	17.39	0.0
	H_{eff}	2.93	1.58	17.22	0.0

5.6 Monte Carlo Simulations

After having full effective Hamiltonian that reproduces β and α structures accurately in comparision with DFT results, we analyze this Hamiltonian with Monte Carlo (MC) simulations on a periodic system containing $L \times L \times L$ (L = 16) unit cells of β structure. We used a single-flip configuration update within Metropolis scheme and adjusted the step-size of configurational $\{\vec{\tau}_i, \vec{\tau}'_i\}$ updates to maintain the acceptance ratio of ~ 0.5 near the transformation temperature. In each Monte Carlo sweep (MCS), we picked τ_i and τ'_i randomly (totally $2L^3$ updates) and homogeneous strain variables L times. Thus, each MCS involves $(2L^3 + L)$ attempts of updating the configuration of the system. To identify different phases from the configurations sampled in MC simulations at a given temperature, we accumulated absolute values of Fourier components of τ_i and τ'_i, project them on eigenvectors of M-point phonon modes ($M_{5'}$, $M_{2'}$ and $M_{4'}$) and obtained their ensemble averages, and of strain

(<ε>) components at each temperature. To assess the possibility of hysteresis, we approach the transformation from high (low)-temperatures by cooling (heating) the system. In cooling simulations, we start from 600 K temperature, equilibrate the system to the cubic phase, and reduce the temperature in steps of 10 K (and 2 K near the transformation temperature), down to the 400 K temperature. In heating simulations, we start from T=400 K taking α structure as the initial configuration and increase the temperature in steps of 10 K (and 2 K near the transformation temperature) to a high-temperature of 600 K (we checked that our results do not depend on the choice of initial configuration). At each temperature, we used 10000 MCS for thermal equilibration and 50000 MCS for thermodynamic averaging of various observables.

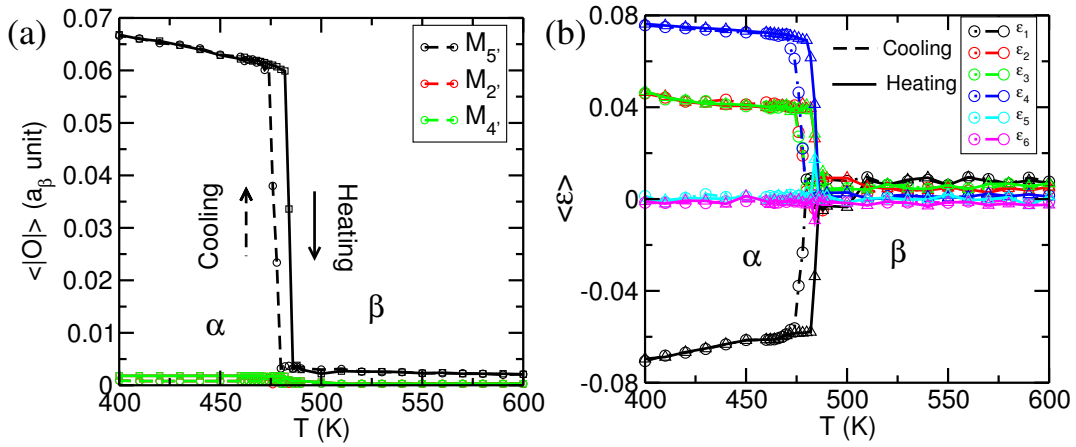

Figure 5.4: Averages of absolute values of $M_{5'}$, $M_{2'}$ and $M_{4'}$ modes (a) and components of strain tensor (b) as a function of temperature at ambient pressure.

Average values of the $|M_{5'}|$, $|M_{2'}|$ and $|M_{4'}|$ (Fig. 5.4a) and homogeneous strain components ε (Fig. 5.4b) vanish at high-temperatures, and change discontinuously to non-zero values at $T < T_M$. In cooling simulations, this discontinuity marks the MT at $T_M = 478$ K. In heating simulations α structure transforms into β structure at $T_A = 484$ K. From these Monte Carlo simulations we find that averages of $|M_{2'}|$,

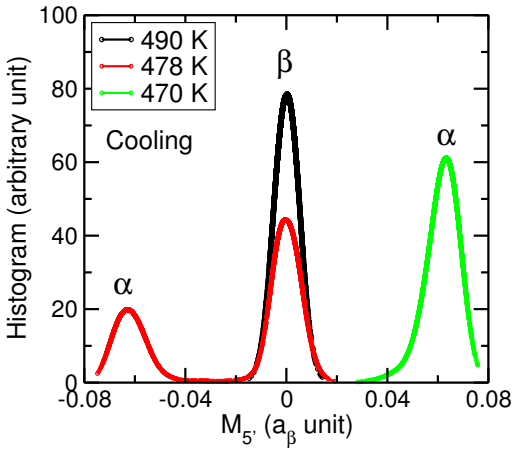

Figure 5.5: Histograms of $M_{5'}$ mode obtained from configurations sampled during cooling at T_M and its two temperatures in its close vicinity.

$|M_{4'}|$ and components of non-basal shear (ε_5 and ε_6) remains zero at all temperatures (Fig. 5.4a and 5.4b), confirming that titanium transforms from β to α structure at ambient pressure. MC simulations reveal a discontinuity in order parameters at T_M and hysteresis of ΔT ~6 K in cooling and heating simulations indicate the first-order character of MT in titanium. We also analyze the histograms of primary order parameter ($M_{5'}$) obtained from cooling (Fig. 5.5) simulations, which reveal (i) relatively narrow and sharp distributions of ordering parameters and (ii) a sharp jump across T_M. Bimodal nature of the histogram at T_M confirms the coexistence of β and α, and the first-order character of the MT. In order to further corroborate these results, we ploted square of frequency (ω) and Binder fourth order cumulant (C_4) of M_5' mode using Eq. 3.10 and Eq. 3.11 in cooling and heating simulations respectively. Softening in $M_{5'}$ phonon frequency and its T-coefficients (Fig. 5.6a) below and above T_M, and a discontinuity in C_4 (Fig. 5.6b) of M_5' mode at T = 478 (484) K in cooling (heating) confirm that $M_{5'}$ mode is the primary order parameter in β to α transformation in pure titanium. Our estimate of the equilibrium transition temperature ($T_c = \frac{1}{2}(T_M + T_A) = 481$ K) is much underestimated with respect to experiment ($T_c = 1155$ K) [117], similar to the errors in our estimates

of transformation temperature in NiTi [45], PtTi (chapter 4) and in ferroelectrics structural transformations [23]. This is probably because of the GGA-DFT errors in energies and structural parameters, and needs further analysis.

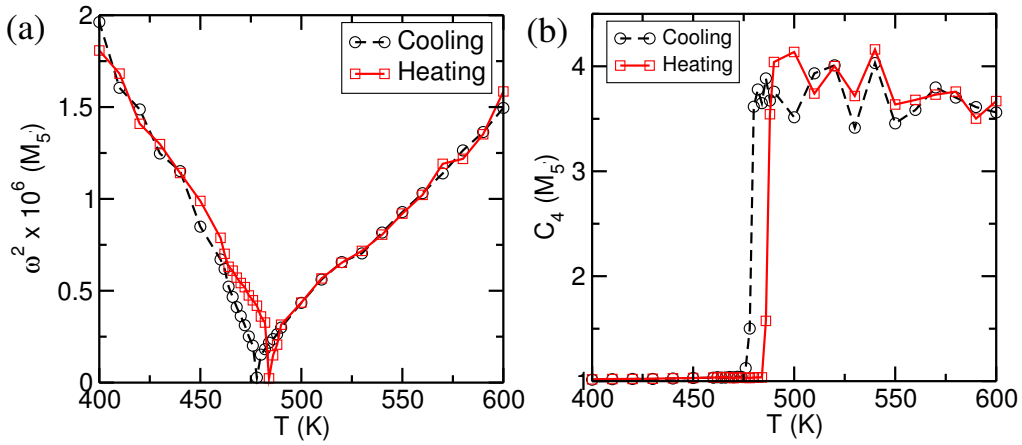

Figure 5.6: Square of frequency (a) and Binder fourth order cumulant (b) of primary order parameter $M_{5'}$ phonon mode.

5.7 Landau theoretical analysis of effective Hamiltonian

To analyze H_{eff} and determine couplings that are relevant to the observed MT in titanium, we present a Landau theory obtained by projecting the full H_{eff} into the subspace of only in the non-zero order parameters $M_{5'}$ phonon at M-point $\frac{\pi}{a}(011)$ wave-vector and strain components involved in strain order parameters. In the projected subspace, τ span the subspace of primary order parameter given by $M_{5'}$ phonon mode, restricting to the symmetries of the hexagonal phase of titanium with $\varepsilon_3 = \varepsilon_2$ and $\varepsilon_6 = \varepsilon_5 = 0$,

$$
\begin{aligned}
H_{Landau}(\tau,\varepsilon) &= a_1\tau^2 + a_2\tau^4 + a_3\tau^6 + a_4\tau^8 \\
&+ (g_1\varepsilon_1 + g_2\varepsilon_2 + g_3\varepsilon_4)\tau^2 \\
&+ (g_4\varepsilon_1^2 + g_5\varepsilon_2^2 + g_6\varepsilon_1\varepsilon_2 + g_7\varepsilon_4^2)\tau^2, \qquad (5.13)
\end{aligned}
$$

where a_i's and g_i's are the coefficients of terms in $M_{5'}$ phonon and its coupling with strains respectively. Values of these coefficients are the linear combinations of respective coefficients of the full H_{eff} and listed in Table 5.12. Instability of M_5' mode (a_1 =-21.4 eV/f.u. < 0) corresponds to $\{0\bar{1}1\}$ <0 1 1> shuffle, whose coupling with ε_1 (g_1=28.7 eV/f.u.) is positive, and with ε_2 (g_2=-98.0 eV/f.u.) is negative. Therefore, ε_1 must be negative and $\varepsilon_3 = \varepsilon_2$ positive to minimize the energy of system, consistent with Bain strain distortion that lowers the symmetry of cubic structure to tetragonal one. Coupling of τ with ε_4 ($\{010\}$<0 0 1> pure shear, g_3=50.9 eV/f.u.) transforms β structure to α structure. Rest of the terms in $H_{Landau}(\tau,\varepsilon)$ are to capture the correct structural parameters and energetics of α structure.

Table 5.12: Coefficients of Landau energy expression are the linear combination of the coefficients of H_{eff}.

Landau coeff.	H_{eff} coeff.	Values (eV/unit cell)
a_1	$4A_{01} - \frac{2}{3}A_{02} + 4A_{11} + 2A_{12} + 2A_{21} + 2A_{22} + 4A_{23}$	-21.4
a_2	$16B_{41} + 4B_{42}$	1.49×10^3
a_3	$32B_{61}$	-3.98×10^4
a_4	$64B_{81}$	4.51×10^5
g_1	$-\frac{4}{3}(h_{30} + h_{31}) + 8g_{30} + 4g_{32} + 16g_{37}$	28.7
g_2	$-\frac{8}{3}h_{30} + 16g_{30} + 8g_{31} + 8g_{32} + 4g_{33} + 4g_{34} + 32g_{37} + 16g_{38}$	-98.0
g_3	$-\frac{8}{3}h_{33} + 4g_{35} + 8g_{39}$	50.9
g_4	$8g_{40}$	161.4
g_5	$16g_{40} + 8g_{41} + 8g_{43}$	451.1
g_6	$8g_{42} + 8g_{43}$	-267.1
g_7	$8g_{44}$	86.1

5.8 Summary

In summary, we presented a thorough statistical mechanical analysis of an effective Hamiltonian derived to capture its low-energy landscape of Ti using Monte Carlo simulations. We (a) determined its soft modes and establish the cell-doubling $M_{5'}$ phonon mode of the β structure as the primary order parameter of MT, and (b) there are three other secondary order parameters marking the MT in Ti. Our predictions of β to α transformation temperature are underestimated with respect to experiments, and further analysis is needed to understand this.

Chapter 6

Fourier-Landau Theory of Martensitic Transformations in Group IV B Transition Metals

6.1 Introduction

Group IV B transition metals undergo following martensitic transformations (MT): from (i) high-temperature body-centered cubic (BCC or β) phase to hexagonal close-packed (HCP or α) phase, (ii) α phase under pressure to hexagonal open-packed (HOP or ω) phase, and (iii) β phase to ω phase above a triple point [117]. Experimentally, α structure is the ground state at room temperature and ambient pressure, ω phase stabilizes under pressure and β is the stable phase at high temperatures (below the melting point) of these transition metals [117]. However, first-principles theoretical calculations support that ω structure is the ground state phase of Ti and Zr, while α phase is the ground state structure of Hf [136, 137]. The MTs in group IV B metals have been extensively studied in experimental [117,135,138,139]

and theoretical [125, 136, 137, 140] analysis over the last few decades. It is well established from these studies that (i) β to α transformation occurs via $\{0\bar{1}1\}<011>$ shuffle corresponding to instability of a transverse acoustic (TA_1) phonon [127, 128] at wave-vector $N = \frac{1}{2}(011)$ of β-phase and (ii) β to ω transformation occurs via plane collapse along the [111] direction of the β structure corresponding to instability of a longitudinal acoustic (LA) phonon [129–131] at $q_\omega = \frac{2}{3}(111)$ wave-vector.

Earlier first-principles based calculations [121, 125, 136, 140, 141] were focused on calculating the structural parameters, electronic and vibrational properties of these metals and comparing them with experiments. A few of them estimated transformation temperatures determining free-energy of different structures of Ti, Zr and Hf elemental metals [125,136]. Though theoretical understanding of different structures and unstable phonons that link the parent β phase to product α and ω phases is achieved quite well, certain aspects of Landau-like theory to model energy landscapes associated with paths connecting β structure to α and ω structures are not quite clear.

In this chapter, we present a Landau theoretical analysis of martensitic transformations in group IV B transition metals with focus on the primary order parameters of these transformations. In Sec. 6.2, we present details of first-principles calculations and optimized structural parameters of different structures of group IV B elemental metals and their energies. In Sec. 6.3, we present phonon spectra of their β structure and discuss various lattice instabilities in the BCC structure of these metals. In Sec. 6.4, we present energy along the path of (i) β to α and (ii) β to ω martensitic transformations in these metallic materials and show that a periodic generalization of Landau free energy function is necessary to capture the physics of these transformations. We finally summarize our work in Sec. 6.5.

6.2 Computational methods and structural stability

We performed first-principles calculations within density functional theory (DFT) using a plane-wave pseudopotential scheme implemented in the Quantum Espresso (QE) package [81], with a local density approximation (LDA) in a Perdew-Zunger [82] parametrized form of exchange-correlation energy functional. Results for properties of group IV B metals are sensitive to energy cutoff used to truncate basis sets and k-points, and hence we use fairly high accuracy parameters in our calculations. We use energy cutoffs of 50 Ry and 400 Ry to truncate plane-wave basis sets used for representing Kohn-Sham wave functions and charge density, respectively. Brillouin zone integrations in Kohn-Sham calculations were sampled on uniform meshes of $24 \times 24 \times 24$ k-points for β, $24 \times 24 \times 18$ k-points for α and $24 \times 24 \times 36$ k-points for ω structures. We relaxed structures to minimize energy with respect to lattice parameters and atomic positions until the magnitude of stresses is less than 5 kbar and Hellmann-Feynman force on each atom is less than 1 meV/$\mathring{A}$. Within the framework of DFPT, we determined dynamical matrices and phonons at q-points on a $4 \times 4 \times 4$ mesh.

Our estimates of structural parameters (Table 6.1) are underestimated with respect to experiments [138] as is typical of LDA based DFT calculations. Relative energies of different structures of Ti, Zr and Hf reconfirm that ω is the ground stable structure of Ti and Zr while α is the groud state of Hf at 0 K temperature and ambient pressure (Table 6.1). These results are consistent with results of earlier theoretical works [136, 137].

Table 6.1: Structural parameters and energies of β, α and ω phases of Ti, Zr and Hf relative to their α phases respectively, obtained with first-principles LDA DFT calculations.

		Ti			Zr			Hf		
Phase	Method	a ($\AA$)	c/a	$E-E_\alpha$ (meV/atom)	a ($\AA$)	c/a	$E-E_\alpha$ (meV/atom)	a ($\AA$)	c/a	$E-E_\alpha$ (meV/atom)
β	LDA	3.16		108	3.48		45	3.42		151
	Exp [138]	3.28			3.59			3.55		
α	LDA	2.94	1.58	0	3.15	1.62	0	3.11	1.58	0
	Exp [138]	2.95	1.59		3.23	1.59		3.19	1.58	
ω	LDA	4.58	0.62	-5	4.92	0.63	-14	4.82	0.62	23
	Exp [138]	4.62	0.61		5.04	0.62		4.98	0.62	

6.3 Phonon dispersion of BCC (β) structure

We determined phonon spectra of group IV B elemental crystal stats in their β structures using DFPT calculations, and find unstable phonons at many wave-vectors through the BZ, showing the structural instability of β-phase of these materials at low-T. Our results agree well with earlier theoretical results [142, 143]. In these materials, the transverse acoustic (TA_1) phonon mode at N ($= \frac{1}{2}(011)$) wave-vector constitute the strongest lattice instability of β structure (Fig. 6.1a). This N point instability is responsible for the $\beta \rightarrow \alpha$ martensitic transformation in these transition metals, as we showed in our work on martensitic transformation in Ti in chapter 5 (where M wave-vector in the BZ of the conventional cubic unit cell of β structure is equivalent to N wave-vector in the BZ of its primitive unit cell).

6.4 Landau theory

Landau theory models free energy function of order parameters of structural transformations typically expressed as symmetry allowed polynomial using the parent phase as the reference. It captures physics of all symmetry equivalent odered states. We use these ideas to model the energy along path of martensitic transformations

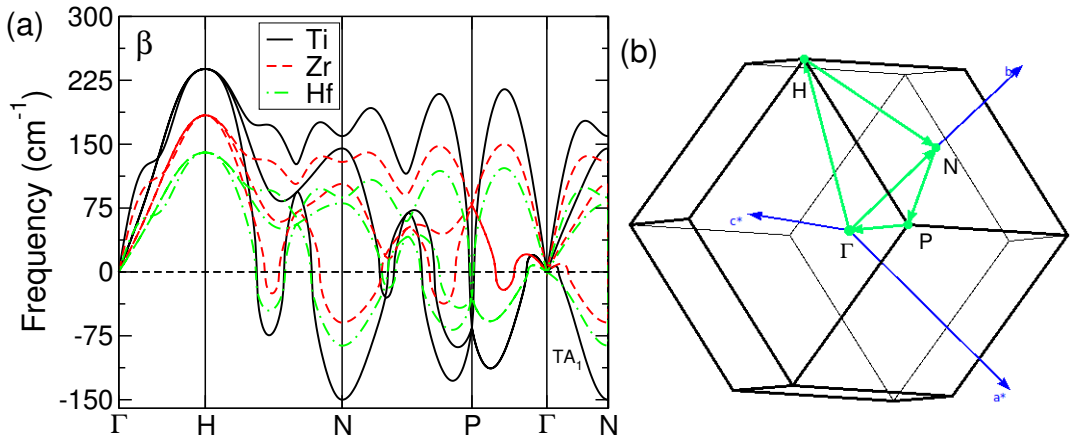

Figure 6.1: Phonon dispersion (a) along high-symmetry lines in Brillouin zone (b) of primitive unit cell of β structures of Ti (black), Zr (red) and Hf (green) obtained using DFPT simulations. Unstable modes with imaginary frequencies ($\omega^2 < 0$) are shown with negative values.

expressed in terms of the order parameters of (i) β to α, and (ii) β to ω transformations in the group IV B transition metals. We demonstrate that the polynomial free-energy function in conventional Landau theory needs to be generalized here to a Fourier series to capture the translational symmetry of the crystalline lattice.

6.4.1 $\beta \rightarrow \alpha$ transformation

Unstable TA_1 phonon at N wave-vector is the primary order parameter of β to α martensitic transformation that describes the required lattice distortion of β structure leading to α structure. At a particular value of the amplitude of eigenvector of this TA_1 phonon and strain β transforms to α structure (see Fig. 5.2 and Table 5.2 in chapter 5, N and M wave-vectors in the BZs of primitive and conventional unit cells of β structure respectively are the same.). At different values of the magnitude of primary order parameter, we relaxed the distorted structure with 2-atoms super cell generated by N wave-vector phonon. We find that at $u = 0.092$, β structure transforms to α structure. We also observe that the energy landscape is a periodic function of u, with periodicity of $u_0 = 0.5$. Such behavior of energy landscape forces

us to use a periodic function as a model. As $E(u)$ in Fig 6.2 is an even function, we fitted this energy curve to a Fourier series:

$$E(u) = E_0 + \sum_{n=1}^{N=4} a_n cos(\frac{4n\pi}{u_0}u), \tag{6.1}$$

where E_0 and a_n's are the parameters (Fourier coefficients) defining the periodic function. u_0 denotes the periodicity in crystal lattice. We find that a series with at $N = 4$ in Eq. 6.1 fits energy landscape quite well, and its coefficients are presented in Table 6.2. Now the free-energy $F(u)$ as a function of order parameter can be estimate using,

$$F(u) = E(u) + g \int dx |\frac{du}{dx}|^2, \tag{6.2}$$

where g (> 0) is a coefficients, and last term in Eq. 6.2 denotes the kinetic energy that minimize the free-energy if $|u|$ does not vary along x. $F(u)$ can we use to invastigate β to α martensitic transformations in group IV B metals.

Table 6.2: Coefficients of Fourier-Landau energy function (in unit of meV/atom).

Coefficients (meV/atom)	Ti	Zr	Hf
E_0	32.5	69.4	29.8
a_1	-138.3	-153.6	-185.2
a_2	85.4	83.5	105.9
a_3	11.5	6.1	40.3
a_4	-3.2	-13.6	-3.0

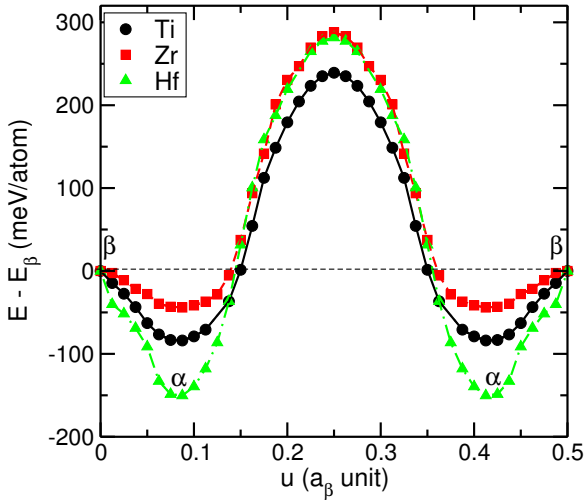

Figure 6.2: Energy landscape as a function of unstable transverse acoustic (TA_1) phonon mode u at $q_N = \frac{1}{2}(011)$ wave-vector.

6.4.2 $\beta \rightarrow \omega$ transformation

Longitudinal acoustic (LA) phonon at $q_\omega = \frac{2}{3}(111)$ wave-vector is the primary order parameter of β to ω transformation. At a particular value of the amplitude of eigenvector of this LA phonon, pair of (111) planes of BCC structure collapse into one resulting in tripling of periodic cell of β structure, and transforming it to ω structure (see Fig. 6.3). At different values of the magnitude of primary order parameter, we relaxed the three atoms super cell of the distorted structure generated by q_ω wave-vector phonon. We find that at $u = 0.1667$, β structure transforms to ω structure, and the associated energy landscape of the path is periodic function of u with a period of $u = 1$, forcing us to use a Fourier series (a periodic function) to fit this. As we see in Fig. 6.3, the energy is neither even nor odd, and we fit this energy landscape to a Fourier series:

$$E(u) \quad = \quad E_0 + \sum_{n=1}^{N=4} \{a_n cos(\frac{2n\pi}{u_0}u) + b_n sin(\frac{2n\pi}{u_0}u)\}, \tag{6.3}$$

where E_0, a_n's and b_n are the Fourier coefficients. We find that at $N = 4$, Eq. 6.3

fits the energy landscape quite well, and its coefficients are given in Table 6.3. Now we can use Eq. 6.2 and Eq. 6.3 to study martensitic transformation from β to ω in Ti, Zr and Hf.

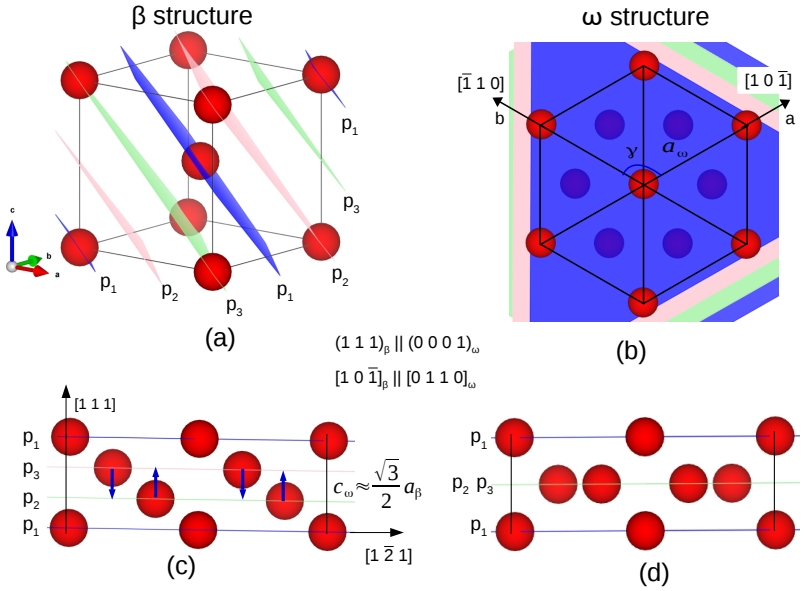

Figure 6.3: Unit cell of β structure showing (1 1 1) planes at a distance of $\frac{\sqrt{3}}{6}a_\beta$ (a), (0001) plane view of ω structure obtaining by the freezing of LA phonon at wave-vector $q_\omega = \frac{2}{3}(111)$ (b), atomic displacements of LA mode in the cell-tripling of the β structure that constitute order parameters of $\beta \rightarrow \omega$ structural transformations (c) and (0 1 1 0) plane view of ω structure (d).

Table 6.3: Coefficients of Fourier-Landau energy function in unit of meV/atom.

Coefficients (meV/atom)	Ti	Zr	Hf
E_0	73.6	103.3	82.4
a_1	-83.3	-89.8	-97.0
a_2	-8.3	-17.3	-10.9
a_3	3.7	7.7	10.3
a_4	15.6	13.3	16.7
b_1	144.0	155.2	167.7
b_2	14.1	29.7	18.7
b_3	0.01	0.01	0.02
b_4	27.2	23.3	29.1

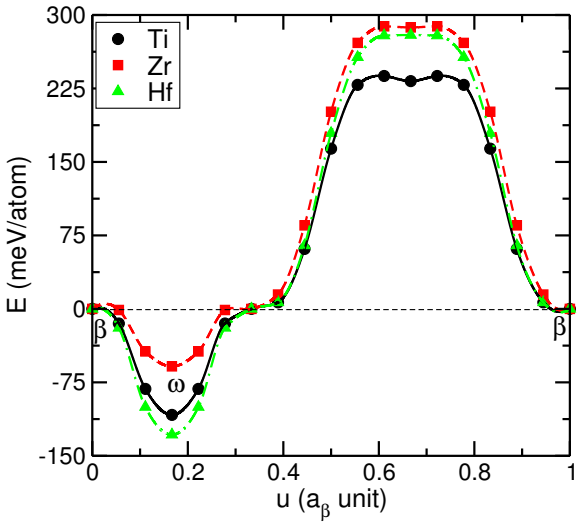

Figure 6.4: Energy landscape as a function of longitudinal acoustic phonon mode u at $q_\omega = \frac{2}{3}(111)$ wave-vector.

6.5 Summary

In summary, we presented Landau theoretical analysis of the energy along paths of (i) β to α and (ii) β to ω martensitic transformations in group IV B transition metals. These paths are parametrized by the respective phonon-related order parameters: phonon modes TA_1 at N and LA at q_ω wave-vectors respectively for $\beta \rightarrow \alpha$ and $\beta \rightarrow \omega$ transformations. We show that Landau-like energy function for these paths of martensitic transformations in the Ti, Zr and Hf elemental metals are periodic and require generalization of the polynomial free energy function in conventional Landau theory to a Fourier series.

Chapter 7

Summary

The central theme of this thesis has been to determine interatomic interactions using first-principles simulations providing access to detailed information on atomistic scale and connect it to macroscopic properties of a material. We have extensively investigated how unstable phonons, nonlinear elasticity and their coupling govern martensitic transformations in metallic materials. Materials studied here are very important in technologies ranging from medical applications to the robotic, aerospace and automotive industries: NiTi and PtTi shape memory alloys, and group IV B elemental transition metals (Ti, Zr and Hf). In our analysis, we have employed a combination of first-principles calculations based on density functional theory, method of lattice Wannier functions for construction of materials-specific effective Hamiltonian, and analysis based on Landau theories.

One of the new methods developed here was for estimating the contribution of unstable phonons to free-energies. It has been successfully achieved by treating them as quantum anharmonic oscillators including the fourth-order anharmonic term in their model Hamiltonian. Solving this Hamiltonian of anharmonic oscillators using a higher-order finite difference method of the kinetic energy operator on a uniform grid in real-space, we presented a scheme to estimate free-energies of these phonons.

We resolved some of the puzzling issues pertaining to relative stability of various martensitic phases in NiTi and PtTi by calculating their free-energies using this scheme.

In the second project, we constructed a materials-specific effective Hamiltonian using the method of lattice Wannier functions in the symmetry invariant subspaces of phonons and strain modes. Materials-specific parameters in this Hamiltonian have been determined from well-designed sets of first-principles calculations. We have performed Monte Carlo simulations of the resulting effective Hamiltonians and investigated the martensitic transformations in NiTi, PtTi and pure titanium metals. Though results of our Monte Carlo simulations underestimate the martensitic transformation temperature (T_M) of these three systems needing further investigation, they uncovered amazingly rich physics of several coupled order parameters, which is key to achieving large deformation without plasticity in shape memory alloys (NiTi and PtTi). We have shown that the unstable $M_{5'}$ phonon mode of austenite phase of these three materials drives the martensitic transformation as the primary order parameter. There are SIX other secondary order parameters in NiTi, and other THREE secondary order parameters in PtTi and Ti, governing their respective martensitic transformations. Within Landau theoretical analysis of the effective Hamiltonian, we show that relative strengths of the third-order couplings of primary order parameter with secondary order parameters fundamentally determine the symmetry of low-T structures emerging at the structural transformation in a given material.

In the final stage of this thesis, we have developed a Fourier generalization of Landau theory, called Fourier-Landau theory, that is essential for a unified description of microstructure and the martensitic transformations in these materials. Using this theory, we have successfully modeled the path of martensitic transformations in the group IV B transition metals.

We summarize our work in a schematic diagram (see Fig. 7.1) which expresses flow of ideas in the topics covered in this thesis. In summary, we have shown that first-principles methods are quite powerful as a tool in investigation of structural stability and low-T properties of materials. These methods provide atomistic information to identify relevant degrees of freedom and determine parameters that model their interactions with an effective Hamiltonian which can be simulated to study finite temperature properties of materials like structural phase transformations.

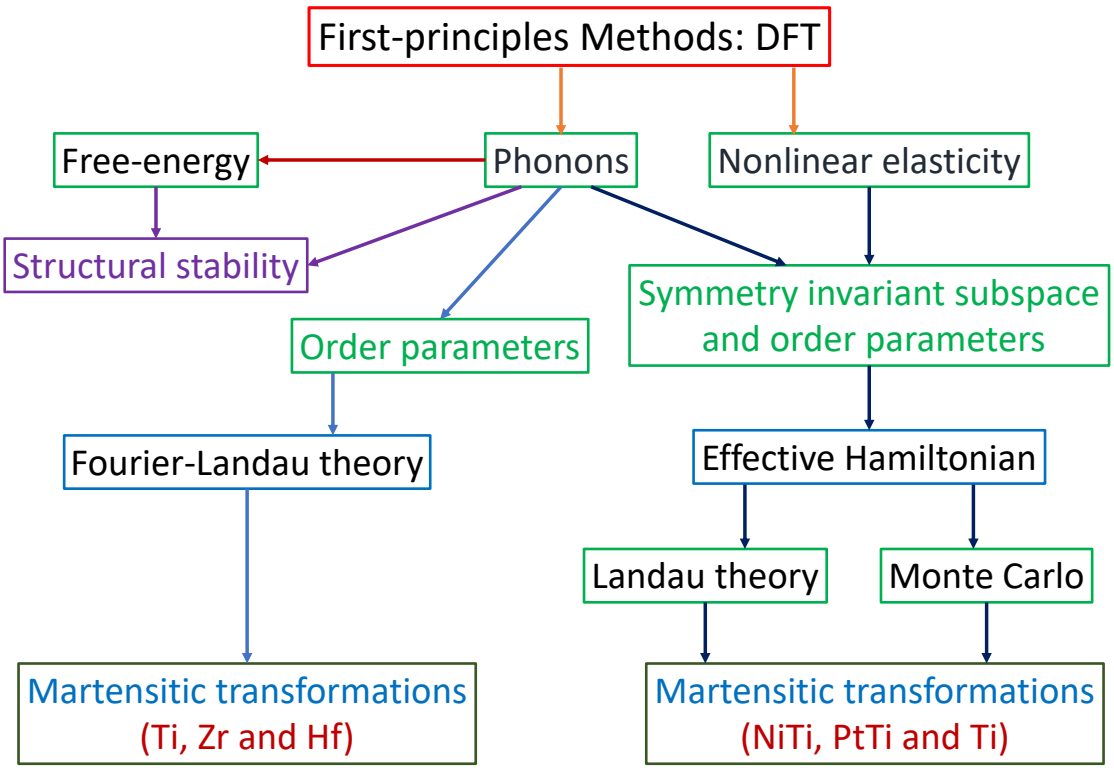

Figure 7.1: A schematic summarizing our work presented in this thesis.

The methods developed in this thesis have general applicability, and open up avenues for further research in physics of materials. Our method to estimate the contributions of unstable phonons to free-energy can be useful in determination of thermodynamic properties of many weakly unstable materials. Secondly, the third-order couplings between the order parameters identified here to be relevant

to symmetry of martensite phases will be useful as descriptors in design of improved shape memory alloys as calculations of these couplings are relatively easy within the framework of first-principles simulations. It should be possible to use the Fourier-Landau theory developed here for martensitic transformations in group IV B transition metals in understanding and design of α and β-stabilizers. Thus, most of the work presented in this thesis will be helpful in the design of metallic alloys with improved properties for smart structures and structural applications in aerospace and automotive industries.

Bibliography

[1] J. Christian, *The Theory of Transformations in Metals and Alloys* (Pergamon, Oxford, 2002).

[2] A. G. Evans and A. H. Heuer, Journal of the Americal Ceramic Society **63**, 241 (1980).

[3] Z. Nishiyama, *Martensitic Transformation* (Academic Press, New York, USA, 1978).

[4] S. Mendelson, Ferroelectrics **37**, 519 (1981).

[5] H. C. Sorby, *New Method of Illustrating the Structure of Various Kinds of Steel by Nature Printing* (Sheffield Literary and Philosophical Society, Sheffield, England, 1964).

[6] A. Westgren, J. Iron and Steel Inst. **207**, 303 (1921).

[7] A. Westgren and G. Phragmen, J. Iron and Steel Inst. **105**, 241 (1922).

[8] A. Westgren and G. Phragmen, J. Iron and Steel Inst. **109**, 159 (1924).

[9] W. J. Buehler, J. V. Gilfrich, and R. C. Wiley, Journal of Applied Physics **34**, 1475 (1963).

[10] E. C. Bain and N. Y. Dunkirk, Trans. Metall. Soc. AIME. **70**, 25 (1924).

[11] G. Kurdjumow and G. Sachs, Z. Physik **64**, 325 (1930).

[12] Z. Nishiyama, Science Reports of Tohoku University **23**, 638 (1934).

[13] M. S. Wechsler, D. S. Lieberman, , and T. A. Read, Trans. AIME **197**, 1503 (1953).

[14] D. S. Lieberman, M. S. Wechsler, and T. A. Read, Journal of Applied Physics **26**, 473 (1955).

[15] J. Bowles and J. Mackenzie, Acta Metallurgica **2**, 129 (1954).

[16] J. Mackenzie and J. Bowles, Acta Metallurgica **2**, 138 (1954).

[17] J. Bowles and J. Mackenzie, Acta Metallurgica **2**, 224 (1954).

[18] J. W. Christian, J Inst Metals **84**, 386 (1955).

[19] K. M. Rabe and J. D. Joannopoulos, Phys. Rev. Lett. **59**, 570 (1987).

[20] K. M. Rabe and J. D. Joannopoulos, Phys. Rev. B **36**, 6631 (1987).

[21] W. Zhong, D. Vanderbilt, and K. M. Rabe, Phys. Rev. Lett. **73**, 1861 (1994).

[22] K. M. Rabe and U. V. Waghmare, Phys Rev. B **52**, 13236 (1995).

[23] U. V. Waghmare and K. M. Rabe, Phys Rev. B **55**, 6161 (1997).

[24] U. V. Waghmare and K. M. Rabe, Ferroelectrics **194**, 135 (1997).

[25] R. M. Martin, *Electronic structure: basic theory and practical methods* (Cambridge university press, Cambridge, UK, 2004).

[26] M. Born and R. Oppenheimer, Annalen der physik **389**, 457 (1927).

[27] P. Hohenberg and W. Kohn, Physical review **136**, B864 (1964).

[28] W. Kohn and L. J. Sham, Physical review **140**, A1133 (1965).

[29] R. O. Jones and O. Gunnarsson, Reviews of Modern Physics **61**, 689 (1989).

[30] D. M. Ceperley and B. Alder, Physical Review Letters **45**, 566 (1980).

[31] S. H. Vosko, L. Wilk, and M. Nusair, Canadian Journal of physics **58**, 1200 (1980).

[32] J. P. Perdew, K. Burke, and M. Ernzerhof, Phys. Rev. Lett. **77**, 3865 (1996).

[33] W. E. Pickett, Computer Physics Reports **9**, 115 (1989).

[34] D. Hamann, M. Schlüter, and C. Chiang, Physical Review Letters **43**, 1494 (1979).

[35] D. Vanderbilt, Physical review B **41**, 7892 (1990).

[36] X. Gonze *et al.*, Computational Materials Science **25**, 478 (2002).

[37] P.-O. Widmark, P.-Å. Malmqvist, and B. O. Roos, Theoretica chimica acta **77**, 291 (1990).

[38] P.-O. Widmark, B. J. Persson, and B. O. Roos, Theoretica chimica acta **79**, 419 (1991).

[39] S. G. Louie, K.-M. Ho, and M. L. Cohen, Phys. Rev. B **19**, 1774 (1979).

[40] O. K. Andersen, Phys. Rev. B **12**, 3060 (1975).

[41] D. D. Koelling and G. O. Arbman, Journal of Physics F: Metal Physics **5**, 2041 (1975).

[42] R. P. Feynman, Physical Review **56**, 340 (1939).

[43] S. Baroni, P. Giannozzi, and A. Testa, Phys. Rev. Lett. **58**, 1861 (1987).

[44] W. Cochran and R. A. Cowley, *Phonons in Perfect Crystals* (Springer, Berlin, Heidelberg, 1967).

[45] P. Kumar and U. V. Waghmare, Materialia **9**, 100602 (2020).

[46] J. R. Chelikowsky, N. Troullier, K. Wu, and Y. Saad, Phys. Rev. B **50**, 11355 (1994).

[47] E. Pytte, Phys. Rev. B **5**, 3758 (1972).

[48] E. Pytte and J. Feder, Phys. Rev. **187**, 1077 (1969).

[49] H. Thomas and K. A. Müller, Phys. Rev. Lett. **21**, 1256 (1968).

[50] W. Kohn, Phys. Rev. **115**, 809 (1959).

[51] J. D. Cloizeaux, Phys. Rev. **135**, A698 (1964).

[52] K. Otsuka and T. Kaseshita, Mater. Res. Bull. **27**, 91 (2002).

[53] G. M. Michal and R. Sinclair, Acta Cryst. B **37**, 1803 (1981).

[54] P. A. Lindgard and O. G. Mouritsen, Phys. Rev. Lett. **57**, 2458 (1986).

[55] E. Goo and R. Sinclair, Acta Metallurgica **33**, 1717 (1985).

[56] Y. Wang and A. G. Khachaturyan, Acta Materialia **45**, 759 (1997).

[57] Y. Kudoh, M. Tokonami, S. Miyazaki, and K. Otsuka, Acta Metallurgica **33**, 2049 (1985).

[58] M. J. Marcinkowski, A. S. Sastri, and D. Koskimaki, Philosophical Magazine **18**, 945 (1968).

[59] F. E. Wang, S. Pickart, and H. A. Alperin, Journal of Applied Physics **42**, 97 (1972).

[60] Y. Y. Ye, C. T. Chan, and K. M. Ho, Phys. Rev. B **56**, 3678 (1997).

[61] X. Huang, C. Bungaro, V. Godlevsky, and K. M. Rabe, Phys. Rev. B **65**, 014108 (2001).

[62] S. Kadkhodaei and A. van de Walle, Acta Materialia **147**, 296 (2018).

[63] J. B. Haskins, A. E. Thompson, and J. W. Lawson, Phys. Rev. B **94**, 214110 (2016).

[64] Z.-Y. Zeng *et al.*, Solid State Communications **149**, 2164 (2009).

[65] K. Parlinski and M. Parlinska-Wojtan, Phys. Rev. B **66**, 064307 (2002).

[66] X. Huang, G. J. Ackland, and K. M. Rabe, Nature Materials **2**, 307 (2003).

[67] K. Otsuka, Progress in Materials Science **50**, 511 (2005).

[68] T. Fukuda, T. Saburi, T. Chihara, and Y. Tsuzuki, Materials Transactions JIM **36**, 1244 (1995).

[69] K. G. Vishnu and A. Strachan, Acta Materialia **58**, 745 (2010).

[70] M. Sanati, R. C. Albers, and F. J. Pinski, Phys. Rev. B **58**, 13590 (1998).

[71] M.-X. Wagner and W. Windl, Acta Materialia **56**, 6232 (2008).

[72] S. Kibey, H. Sehitoglu, and D. D. Johnson, Acta Materialia **57**, 1624 (2009).

[73] J. M. Zhang and G. Y. Guo, Phys. Rev. Lett. **78**, 4789 (1997).

[74] R. Mirzaeifar *et al.*, Journal of Applied Physics **115**, 194307 (2014).

[75] Y. Zhong, K. Gall, and T. Zhu, Journal of Applied Physics **110**, 033532 (2011).

[76] D. Mutter and P. Nielaba, Phys Rev. B **82**, 224201 (2010).

[77] R. R. Pezarini *et al.*, Mater. Res. Express **1**, 026502 (2014).

[78] R. F. Hehemann and G. D. Sandrock, Scripta Metallurgica **5**, 801 (1971).

[79] K. Otsuka and X. Ren, Mater. Sci. Eng. A **273**, 89 (1999).

[80] X. Ren and K. Otsuka, Scripta Materialia **38**, 1669 (1998).

[81] P. Giannozzi *et al.*, J. Phys. Condens. Matter **21**, 395502 (2009).

[82] J. P. Perdew and A. Zunger, Phys. Rev. B **23**, 5048 (1981).

[83] J. Sun, A. Ruzsinszky, and J. P. Perdew, Phys. Rev. Lett. **115**, 036402 (2015).

[84] J. Sun *et al.*, Nature Chemistry **8**, 831 (2015).

[85] G. Kresse and J. Furthmüller, Phys. Rev. B **54**, 11169 (1996).

[86] G. Kresse and J. Furthmüller, Comput. Mater. Sci. **6**, 15 (1996).

[87] G. Kresse and D. Joubert, Phys. Rev. B **59**, 1758 (1999).

[88] W.-S. Ko, B. Grabowski, and J. Neugebauer, Phys. Rev. B **92**, 134107 (2015).

[89] D. Holec, M. Friák, A. Dlouhý, and J. Neugebauer, Phys. Rev. B **84**, 224119 (2011).

[90] J. Lee, Y. Ikeda, and I. Tanaka, Journal of Applied Physics **125**, 055106 (2019).

[91] H. Wang and M. Li, Phys Rev. B **79**, 224102 (209).

[92] X. Li *et al.*, Phys. Rev. B **95**, 024203 (2017).

[93] M. Łopuszyński and J. A. Majewski, Phys. Rev. B **76**, 045202 (2007).

[94] D. Holec, M. Friák, J. Neugebauer, and P. H. Mayrhofer, Phys. Rev. B **85**, 064101 (2012).

[95] M. D. Jong, I. Winter, D. C. Chrzan, and M. Asta, Phys. Rev. B **96**, 014105 (2017).

[96] J. Zhao, J. M. Winey, and Y. M. Gupta, Phys. Rev. B **75**, 094105 (2007).

[97] N. Hatcher, O. Y. Kontsevoi, and A. J. Freeman, Phys. Rev. B **80**, 144203 (2009).

[98] O. Mercier, K. N. Melton, G. Gremaud, and J. Hagi, Journal of Applied Physics **51**, 1833 (1980).

[99] R. Salzbrenner and M. Cohen, Acta Metallurgica **27**, 739 (1979).

[100] G. J. Pataky, E. Ertekin, and H. Sehitoglu, Acta Materialia **96**, 420 (2015).

[101] K. M. Rabe and U. V. Waghmare, Ferroelectrics **194**, 119 (1997).

[102] U. V. Waghmare, Accounts of Chemical Research **47**, 3242 (2014).

[103] F. Mouhat and F. X. Coudert, Phys Rev. B **90**, 224104 (2014).

[104] N. A. Zarkevich and D. D. Johnson, Phys. Rev. B **90**, 060102 (2014).

[105] N. A. Zarkevich and D. D. Johnson, Phys. Rev. Lett. **113**, 265701 (2014).

[106] T. Ezaz, H. Sehitoglu, and H. Maier, Acta Materialia **59**, 5893 (2011).

[107] J. V. Humbeeck, J. Eng. Mater. Technol. **121**, 98 (1999).

[108] H. Donkersloot and J. V. Vucht, Journal of the Less Common Metals **20**, 83 (1970).

[109] A. E. Dwight, R. A. Conner, Jnr, and J. W. Downey, Acta Crystallographica **18**, 835 (1965).

[110] G.-M. Rotaru *et al.*, Acta Materialia **55**, 4447 (2007).

[111] Y. Yamabe-Mitarai, T. Hara, S. Miura, and H. Hosoda, Intermetallics **18**, 2275 (2010).

[112] X. Huang, K. M. Rabe, and G. J. Ackland, Phys. Rev. B **67**, 024101 (2003).

[113] S. Kadkhodaei and A. van de Walle, Acta Materialia **147**, 296 (2018).

[114] N. Nakanishi, A. Nagasawa, and Y. Murakami, Journal de Physique Colloques **43**, C4 (1982).

[115] R. D. King-Smith and D. Vanderbilt, Phys. Rev. B **49**, 5828 (1994).

[116] R. Mahlangu, M. Phasha, H. Chauke, and P. Ngoepe, Intermetallics **33**, 27 (2013).

[117] S. Sikka, Y. Vohra, and R. Chidambaram, Progress in Materials Science **27**, 245 (1982).

[118] D. A. Young, *Phase Diagrams of the Elements* (Uniersity of California Press, Berkeley, 1991).

[119] J. Gyanchandani and S. Sikka, Solid State Communications **156**, 80 (2013).

[120] J. S. Gyanchandani, S. C. Gupta, S. K. Sikka, and R. Chidambaram, Journal of Physics: Condensed Matter **2**, 301 (1990).

[121] R. Ahuja, J. M. Wills, B. Johansson, and O. Eriksson, Phys. Rev. B **48**, 16269 (1993).

[122] C. W. Greeff, D. R. Trinkle, and R. C. Albers, Journal of Applied Physics **90**, 2221 (2001).

[123] Mehl, M. J. and Papaconstantopoulos, D. A., Europhys. Lett. **60**, 248 (2002).

[124] S. P. Rudin, M. D. Jones, and R. C. Albers, Phys. Rev. B **69**, 094117 (2004).

[125] R. G. Hennig *et al.*, Phys. Rev. B **78**, 054121 (2008).

[126] Z.-G. Mei, S.-L. Shang, Y. Wang, and Z.-K. Liu, Phys. Rev. B **80**, 104116 (2009).

[127] W. Petry *et al.*, Phys. Rev. B **43**, 10933 (1991).

[128] W. Burgers, Physica **1**, 561 (1934).

[129] B. A. Hatt and J. A. Roberts, Acta Metallurgica **8**, 575 (1960).

[130] D. D. Fontaine, Acta Metallurgica **18**, 275 (1970).

[131] K. Persson, M. Ekman, and V. Ozoliņš, Phys. Rev. B **61**, 11221 (2000).

[132] D. R. Trinkle *et al.*, Phys. Rev. Lett. **91**, 025701 (2003).

[133] J. P. Perdew and W. Yue, Phys. Rev. B **33**, 8800 (1986).

[134] R. M. Wood, Proc. Phys. Soc. **80**, 783 (1962).

[135] J. C. Jamieson, Science **140**, 72 (1963).

[136] I. Schnell and R. C. Albers, Journal of Physics: Condensed Matter **18**, 1483 (2006).

[137] S. Ostanin and V. Trubitsin, Computational Materials Science **17**, 174 (2000).

[138] G. Aurelio and A. Guillermet, Journal of Alloys and Compounds **298**, 30 (2000).

[139] H. Xia, A. L. Ruoff, and Y. K. Vohra, Phys. Rev. B **44**, 10374 (1991).

[140] P. S. Ghosh, A. Arya, R. Tewari, and G. Dey, Journal of Alloys and Compounds **586**, 693 (2014).

[141] K. M. Ho, C. L. Fu, and B. N. Harmon, Phys. Rev. B **28**, 6687 (1983).

[142] A. Heiming *et al.*, Phys. Rev. B **43**, 10948 (1991).

[143] P. Souvatzis, O. Eriksson, M. I. Katsnelson, and S. P. Rudin, Phys. Rev. Lett. **100**, 095901 (2008).